CMOS-Compatible High-Speed Silicon Photodetectors for Gbps Fiber-Fed Wireline/Wireless Communication Systems

Hyo-Soon Kang

THE GRADUATE SCHOOL

YONSEI UNIVERSITY

Department of Electrical and Electronic Engineering

CMOS-Compatible High-Speed
Silicon Photodetectors for Gbps Fiber-Fed
Wireline/Wireless Communication Systems

A Dissertation
Submitted to the Department of Electrical and Electronic Engineering
and the Graduate School of Yonsei University
in partial fulfillment of the requirements for the degree of
Doctor of Philosophy

Hyo-Soon Kang

January 2009

This certifies that the dissertation of Hyo-Soon Kang is approved.

_____

Thesis Supervisor: Woo-Young Choi

_____

Sang-Kook Han

_____

Ilgu Yun

_____

Jinwook Burm

_____

Hyuk-Kee Sung

The Graduate School

Yonsei University

January 2009

Table of Contents

iv

List of Figures and Tables

Abstract

Silicon avalanche photodetectors are designed and fabricated with standard CMOS technology. By conducting technology computer-aided-design (TCAD) simulation for optimum device structures in standard CMOS technology, CMOS-compatible avalanche photodetectors (CMOS-APDs) having high gain and large bandwidth are implemented.

From the measurements of DC and photodetection frequency response characteristics, the performance of the fabricated CMOS-APDs is experimentally investigated. When the CMOS-APD operates in an avalanche regime by applying high reverse bias voltage to the device, rf peaking in photodetection response is observed. To clarify the physical origin of the rf peaking effect, impedance characteristics are investigated, and an inductive component in an avalanche region is modeled. Through the equivalent circuit modeling of the CMOS-APD, all the circuit parameters including the avalanche inductance, the junction capacitance, the parasitic components, and the transit-time constants for photogenerated carriers are extracted.

To demonstrate high-speed optical signal transmission, CMOS-APD receivers having a CMOS-APD and a transimpedance amplifier are

fabricated on a board. Using the CMOS-APD receiver, error-free data transmission at the data rate of 6.25 Gbps is successfully performed with bit error rate (BER) less than 10^{-12}.

For realization of cost-effective fiber-fed 60-GHz self-heterodyne wireless systems, CMOS-APDs are utilized as a CMOS-compatible harmonic optoelectronic mixer (CMOS-HOEM) to simultaneously perform photodetection and frequency up-conversion to 60-GHz band. The optoelectronic mixing is performed with the help of the nonlinear characteristics of avalanche multiplication factor. Furthermore, a CMOS-compatible self-oscillating harmonic optoelectronic mixer (CMOS-SOHOM) is implemented by connecting a CMOS-APD and a 30-GHz band electrical feedback loop. Using these CMOS-HOEM and CMOS-SOHOM, 25-Mbps 32-QAM data are transmitted through fiber-fed 60-GHz self-heterodyne wireless downlinks.

Finally, for implementation of cost-effective radio-over-fiber (RoF) systems, CMOS-APD receivers are adopted in base stations for RoF receivers. Single standard signal of 2.1-GHz WCDMA or 5.2-GHz IEEE 802.11a is RoF transmitted using a CMOS-APD receiver. In addition, low-cost RoF systems consisting of an 850-nm vertical-cavity surface-emitting laser (VCSEL), 300-m multimode fiber, and a CMOS-APD receiver are realized to transmit multi-standard RoF signals of

2.1-GHz WCDMA and 2.4-GHz IEEE 802.11g WLAN, simultaneously.

1. Introduction

1-1. Recent trends of optical communication systems

Rapidly growing demand for high-capacity data transmission has accelerated the evolution of optical communication systems from long-haul backbone infrastructures to short-distance optical networks to enhance the penetration of fiber further toward end-users. Moreover, large variety of electrical interconnects including board-to-board and chip-to-chip connections are to be replaced by optical interconnects due to such advantages of optical technology as huge bandwidth, light weight of transmission medium, and immunity to electrical interferences [1-3]. Fig. 1-1 shows emerging applications of optical communication systems such as short-distance optical access networks and optical interconnects.

With these trends of optical communications, several standards including Gigabit Ethernet (GbE), fiber channel [4], and fiber channel over Ethernet (FCoE) [5] are established or recently pursued. However, for successful realization of these optical communication systems, large amount of optical transceivers and wide deployment of optical transmission medium are indispensable. Consequently, cost-effective realization of optical components as well as optical transmission

medium is the most critical issue.

For optical transmitters, AlGaAs/GaAs vertical-cavity surface-emitting lasers (VCSELs) operating at 850 nm are promising candidates due to their low fabrication cost [6], [7]. Together with low-cost VCSELs, multimode fibers have been regarded as cost-effective solutions for transmission medium owing to its easy installation. However, as of yet, optical receivers are challenging parts for the implementation in a cost-effective manner.
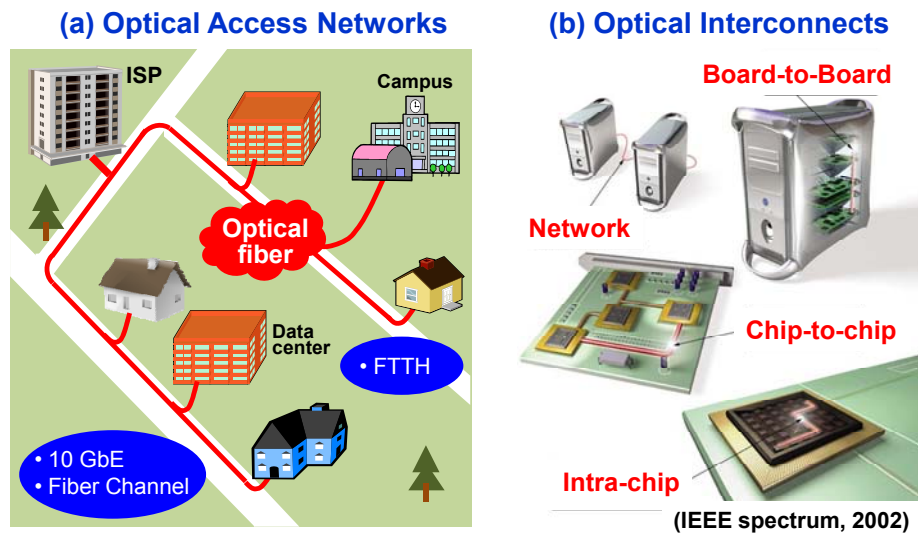
Fig. 1-1. Applications of short-distance optical communication systems: (a) optical access networks and (b) optical interconnects [1].

1-2. CMOS-compatible optical receivers

Complementary metal-oxide-semiconductor (CMOS) technology can provide a powerful solution for low-cost realization of optical receivers [8]. For the past decades, CMOS technology has been used for all types of electronic circuits including analog, digital, and RF applications with the help of its high-volume manufacturability, low fabrication cost, and technological advances. Furthermore, silicon photodetectors fabricated with standard CMOS technology can detect 850-nm optical signals which are widely used for short-distance optical communication systems. Recently, it has been also reported that CMOS-based photodetector can be utilized for 1300/1550-nm optical communication system by adopting germanium layer on silicon substrate with some process modifications [9]. Consequently, well developed CMOS technology can enable cost-effective integrated optical receivers having a photodetector and required electronic circuits such as a transimpedance amplifier (TIA), a limiting amplifier (LA), an equalizer (EQ), and clock-and-data recovery (CDR) circuits on a single chip as shown Fig. 1-2.

In spite of these advantages, there are inherent drawbacks of CMOS technology for photodetector applications. Fig. 1-3 shows simplified cross sectional device structures of CMOS technology. NMOSFET and

PMOSFET are formed by N+ and P+ source/drain regions on P-Well and N-Well, respectively, with gate oxides and poly-silicon gates. In this structure, two PN-junctions for photodetectors can be realized with P+ to N-Well and N-Well to P-Substrate junctions [10]. However, large optical penetration depth of 14 μm in silicon at the wavelength of 850 nm makes it difficult to achieve high responsivity because depletion regions of PN-junctions are usually formed in less than 1 μm under the silicon surface [11]. The responsivity is defined as the ratio of the photocurrent to incident optical power. Moreover, the shallow depletion region due to relatively high doping concentrations in N-Well and P-Substrate causes diffusive transport of the photogenerated carriers in the charge neutral region, limiting high-speed operation.

To improve responsivity and bandwidth of CMOS photodetectors, several approaches have been carried out. A low-doped epitaxial layer in the twin-well process was used to enhance the depletion width and quantum efficiency, resulting in an 1-Gbps optical receiver with 44 % quantum efficiency [12]. In addition, a lateral p-i-n photodetector based on silicon-on-insulator (SOI) substrate, in which slow diffusion currents in the substrate region are blocked, achieved 10-Gbps operation [13]. Although the performance of above CMOS photodetectors is impressive, their realization requires additional

fabrication costs and an approach based on the standard CMOS technology is desired in order to fully utilize the cost advantage of CMOS photodetectors.

With the standard CMOS process, spatially modulated light (SML) detectors in which differential signaling was used to subtracting the slow diffusion tail, resulting in 2-Gbps optical receiver [8]. However, it has weakness of relatively low responsivity and speed limitation due to current subtraction and large active area, respectively. By using equalizer circuits to compensate low-speed photodetectors, a 3-Gbps optical receiver was developed [14]. This scheme, though, requires knowledge in accurate photodetector responses and complicates the receiver circuit design. Recently, p+-p-n avalanche structure has been reported that provides high speed and high responsivity [15]. Based on this photodetector, bandwidth enhancement technique by eliminating slow diffusion photogenerated carriers was also devised [16]. Although this structure provides high responsivity owing to a large depletion region formed by N-Well/P-Substrate junction, relatively high dark current can be generated. Furthermore, the advantage of high responsivity can be sacrificed by body voltages applied for elimination of slow diffusion components. More severely, positive body voltages make it difficult to implement integrated optical receivers because the

substrate potential of all the electronic circuits should be set to ground.

In this dissertation, CMOS-compatible avalanche photodetectors (CMOS-APDs) having high responsivity and large bandwidth are presented for low-cost optical communication systems.
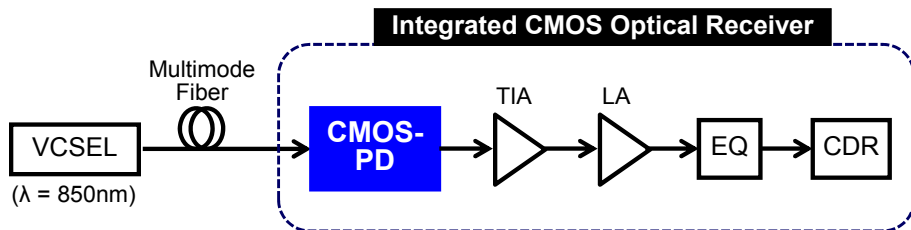
Fig. 1-2. Block diagram of an integrated CMOS optical receiver, which consists of a CMOS-compatible photodetector (CMOS-PD) and electronic circuits including a transimpedance amplifier (TIA), a limiting amplifier (LA), an equalizer (EQ), and clock-and-data recovery (CDR) circuits.
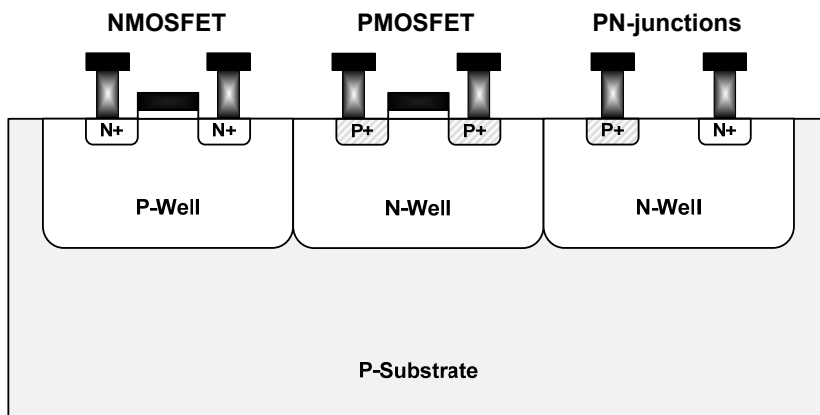
Fig. 1-3. Simplified cross sectional device structures of CMOS technology.

1-3. Outline of dissertation

This dissertation will focus on CMOS-compatible avalanche photodetectors (CMOS-APDs) and their applications for Gbps baseband data transmission, fiber-fed 60-GHz self-heterodyne wireless system, and low-cost radio-over-fiber systems. Design consideration and characteristics of fabricated CMOS-APDs also will be presented. Details of dissertation outline are as follows.

In chapter 2, design considerations for CMOS-APDs to achieve high responsivity and high speed are introduced at first. Section 2-2 shows simulation results of technology computer-aided-design (TCAD) for the optimization of CMOS-APDs. The structure of fabricated CMOS-APDs is explained in section 2-3.

Chapter 3 shows characteristics of the fabricated CMOS-APD. Experimental setup for device characterization is explained in section 3-1. Characteristics of DC and photodetection frequency response are followed in section 3-2 and 3-3, respectively. Section 3-4 presents an equivalent circuit model and extracted parameters from the measurement of RF impedances and photodetection frequency responses.

In chapter 4, 6.25-Gbps baseband data transmission is demonstrated. Section 4-1 describes a CMOS-APD receiver, which is implemented

with a CMOS-APD and a transimpedance amplifier (TIA) on a board. Experimental setup is described in section 4-2 and 6.25-Gbps data transmission results are shown in section 4-3.

For applications of fiber-fed 60-GHz self-heterodyne wireless systems, CMOS-APDs are utilized for a harmonic optoelectronic mixer (CMOS-HOEM) and a self-oscillating harmonic optoelectronic mixer (CMOS-SOHOM). The architecture and characteristics of self-heterodyne wireless systems are introduced in section 5-1. Operation principle of harmonic frequency up-conversion by utilizing a CMOS-APD as a harmonic optoelectronic mixer is explained in section 5-2. Experiments of frequency up-conversion to 60-GHz band and 25-Mbps 32-QAM data transmission are also demonstrated. Section 5-3 shows the results of the self-oscillating harmonic optoelectronic mixer using a CMOS-APD. Configuration and performance of the self-oscillating mixer are presented. Demonstration of 25-Mbps 32-QAM data transmission is also presented in section 5-3.

In chapter 6, cost-effective Radio-over-Fiber (RoF) systems using the CMOS-APDs are presented. Section 6-2 demonstrates single standard RoF transmission for 2.1-GHz WCDMA or 5.2-GHz 802.11a WLAN using the CMOS-APD receiver. With the CMOS-APD receiver as well as a VCSEL, both 2.1-GHz WCDMA and 2.4-GHz 802.11g

WLAN signals are simultaneously transmitted via 300-m multimode fiber and the experimental results are presented in section 6-3.

Finally, the dissertation will be summarized in chapter 7.

2. Design of CMOS-Compatible Silicon Avalanche Photodetectors

2-1. Design considerations for CMOS-APDs

When optical signals in which photon energy is larger than bandgap energy of semiconductor are illuminated to photodetectors, incident photons generate electron-hole pairs in semiconductor regions. Among these generated carriers, carriers in the depletion regions can only induce currents to external circuits because the electric field in the depletion region causes drift of carriers. With these drift currents, some amounts of photogenerated carriers in the charge neutral region can enter into the depletion regions with diffusive transport thus generate photocurrents. Consequently, the depletion width of PN-junction dominantly affects the performance of photodetectors.

Using standard CMOS technology, PN-junctions can be implemented. Fig. 2-1 shows simplified cross-sectional structure of PN-junctions in standard CMOS technology. There are two PN-junctions which are formed by P+ source/drain to N-well regions and N-well to P-substrate regions. The depletion width (W) built in PN-junctions can be estimated by following equations with the assumption of abrupt PN-junctions [17].

$$V_{bi} = \frac{k_B T}{q} \ln\left(\frac{N_A N_D}{n_i^2}\right) \quad [\text{V}]$$

(2.1)

$$W = \sqrt{\frac{2\varepsilon_s}{q}\left(\frac{N_A + N_D}{N_A N_D}\right)(V_{bi} + V_R)} \quad [\text{m}]$$

(2.2)

where, V_{bi} is built-in voltage of a PN-junction, k_B is Boltzmann constant, T is temperature, q is electron charge, N_A is acceptor doping concentration, N_D is donor doping concentration, n_i is intrinsic carrier concentration of silicon, ε_s is permittivity of silicon, and V_R is the reverse bias voltage.
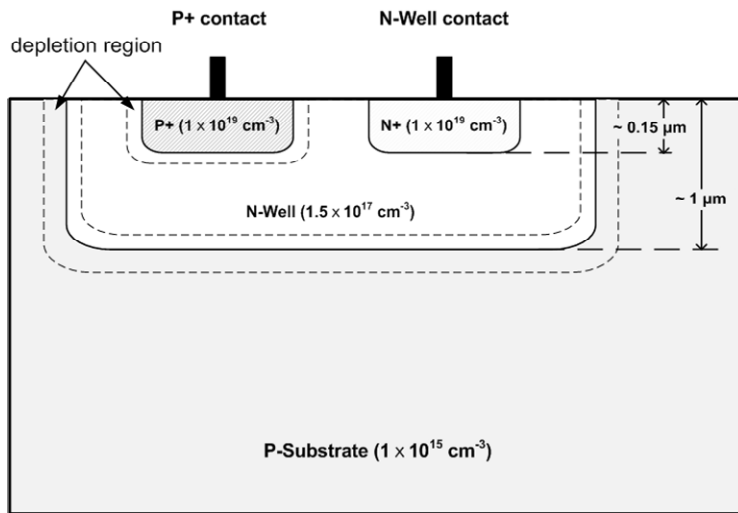
Fig. 2-1. PN-junctions formed by P+/N-Well and N-Well/P-substrate regions in standard CMOS technology. The values in parentheses shows estimated doping concentrations. Dashed lines indicate depletion regions formed in PN-junctions.

From (2.2), the depletion widths of P+/N-Well and N-Well/P-Substrate junctions under zero-bias condition are calculated as 0.09 μm and 0.98 μm, respectively. Due to the low doping concentration of the P-Substrate region compared with the P+ source/drain region, large depletion width by the N-Well/P-Substrate junction can be formed. For efficient collection of the photogenerated carriers, therefore, the N-Well/P-Substrate junction is more suitable than the P+/N-Well junction. Although the N-Well/P-Substrate junction can generate larger photocurrents, carrier transport mechanism, which determines speed of photodetectors, should be considered as well.

The speed of PN-junction photodetectors is mainly limited by three time constants: carrier drift time in the depletion region (τ_{drift}), carrier diffusion time in the charge neutral region ($\tau_{diffusion}$), and RC time constant (τ_{RC}) as explained in following equations [18].

$$
\begin{aligned}
\tau_{drift} &= W / v \\
\tau_{diffusion} &= l_0{}^2 / (2 \cdot D) \\
\tau_{RC} &= (R_S + R_L) \cdot C_J
\end{aligned}
\tag{2.3}
$$

where, W is the depletion width, v is carrier velocity under the applied electric field, l_0 is diffusion length of the charge neutral region, D is

diffusion constant of silicon, R_S is series resistance, R_L is load resistance, and C_J is junction capacitance formed in a PN-junction.

As mentioned before, photocurrents are induced by the photogenerated carriers in the depletion region as well as the diffusive carriers entered into the depletion region from the charge neutral regions. Since depletion widths of PN-junctions are relatively narrow compared with the length of the charge neutral region in standard CMOS technology, large amounts of optical signals are absorbed in the charge neutral region and the speed of PN-junction photodetectors are dominantly constrained by the diffusion time. Especially for N-Well/P-Substrate junction, large diffusion currents can be generated in the P-Substrate region and these severely limit the photodetector speed. Accordingly, the P+/N-Well junction is favorable for the high-speed photodetector in spite of its low photocurrents due to the narrow depletion width. Furthermore, optimized device layout for reducing the series resistance and the junction capacitance, which are dependent on area of the active region, is required for diminishing RC-time limit.

Although the above mentioned considerations are taken into account for design of photodetectors, the performance of CMOS-PDs is still insufficient for high-speed optical communication systems. For instance, the P+/N-Well junction photodetector has diffusion time

constant of approximately 0.23 ns, which corresponds to 3-dB bandwidth of about 0.69 GHz at the reverse bias voltage of 5 V. For this estimation, the depletion width of 0.23 μm is calculated from the P+/N-Well junction and diffusion coefficient of 7.8 cm^2/s is assumed at doping concentration of 1.5×10^{17} cm^{-3} in the N-Well region. The narrow depletion width, which is much smaller than the 850-nm optical penetration depth of 14 μm in silicon, is also problematic for absorption efficiency.

To solve these intrinsic problems of low responsivity and limited speed, this dissertation concentrates on the implementation of avalanche photodetectors using standard CMOS technology. With the help of avalanche multiplication process, the photogenerated carriers can be amplified thus photocurrent increased. Furthermore, bandwidth of photodetectors can be enhanced by the enlarged depletion width under high electric field owing to reduced diffusive carriers and shortened diffusion length. In this dissertation, the rf peaking effect in photodetection frequency response is also presented with equivalent circuit modeling. The avalanche inductance appeared in the avalanche region can induce rf peaking and this results in bandwidth enhancement of avalanche photodetectors.

To realize avalanche photodetectors using standard CMOS

15

technology, an additional factor should be considered for device optimization. When the electric field increases with the increasing reverse bias voltage, avalanche multiplication process starts to occur more likely in the lateral junction periphery due to the stronger electric field in curved junction periphery than planar junction periphery [19]. This premature edge breakdown prevents the photogenerated carriers from having sufficient electric field to obtain avalanche gain. Additionally, multiplication of dark current due to the edge breakdown effect degrades signal-to-noise ratio (SNR) by increasing noise power. To mitigate the edge breakdown effect, this dissertation presents the P+/N-Well junction surrounded by shallow trench isolation (STI) formed with SiO_2. Because dielectric strength of SiO_2 is higher than breakdown field of silicon by 30 times [20], premature breakdown in the lateral edge of P+/N-Well can be avoided with STI. The simulation results for the STI effect on edge breakdown will be demonstrated in the following section.

2-2. TCAD simulation

In order to optimize the structure of CMOS-APDs for high-speed operation, technology computer-aided design (TCAD) simulation was performed using Synopsys TCAD tools including TSUPREM4 and MEDICI. Due to the lack of detailed process parameters for CMOS technology, commonly known doping profiles and junction depths are used for simulation [21].

2-2-1. *Two PN-junctions in CMOS technology: P+/N-Well and N-Well/P-Substrate junctions*

As discussed in the previous section, for achieving high-speed operation, the P+/N-Well junction photodetector is suitable to block slow diffusion currents in P-Substrate. To verify this, TCAD simulation was performed. Fig. 2-2 shows cross-sectional structure for the TCAD simulation. The P+ and N+ regions are formed in the N-Well region to construct P+/N-Well junction and N-Well contact, respectively. In the simulation, optical signals are injected into only the P+ region on N-Well to account for the photocurrents generated in vertical PN-junctions of the P+/N-Well and N-Well/P-Substrate regions.

Fig. 2-3 shows simulated photodetection frequency responses when

17

the bias voltage of 6 V is applied to N-Well contact. The output signals are extracted from P+ and N-Well contacts. The current from P+ contact are attributed to the photogenerated carriers in P+/N-Well junction. Whereas, the currents from N-Well contact are induced by the photogenerated carriers in both P+/N-Well and N-Well/P-Substrate junctions. As shown in Fig. 2-3 (a), N+ contact has larger photocurrents compared with P+ contact because photogenerated carriers are collected by both PN-junctions. However, it can be seen that photocurrent density at N-Well contact has low frequency components, which are caused by slow diffusion currents in the P-Substrate region. Fig. 2-3 (b) shows normalized photodetection frequency response at P+ and N-Well contacts. It is clearly observed that the 3-dB bandwidth of N-Well contact currents is lower than P+ contact due to slow diffusion currents. From this simulation, it is verified that P+ contact current induced only by P+/N-Well junction are suitable for high-speed operation of the CMOS-APD.
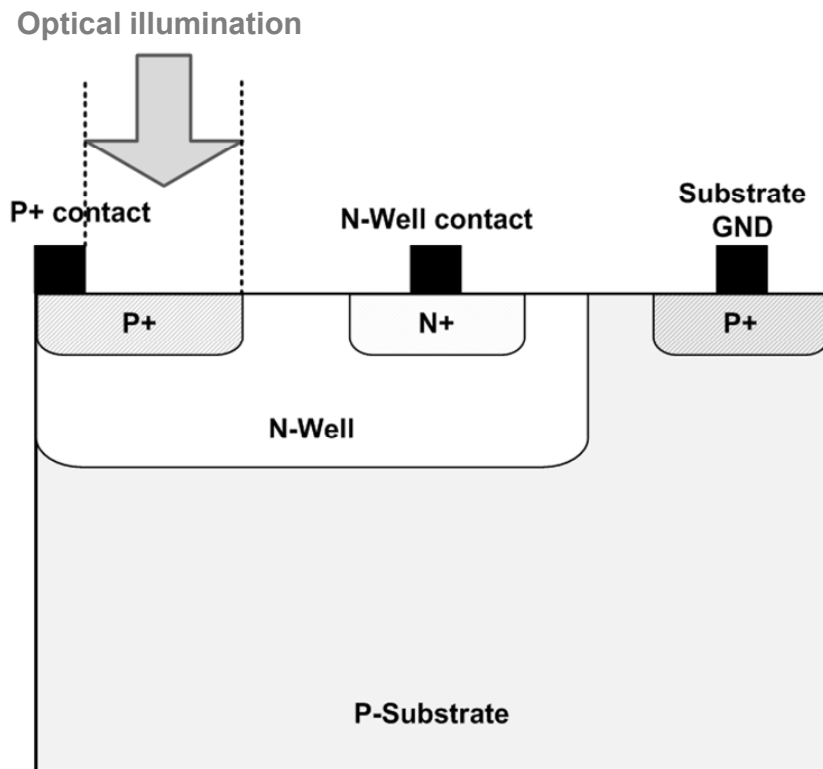
Fig. 2-2. Cross-sectional structure of a CMOS-compatible avalanche photodetector for TCAD simulation.
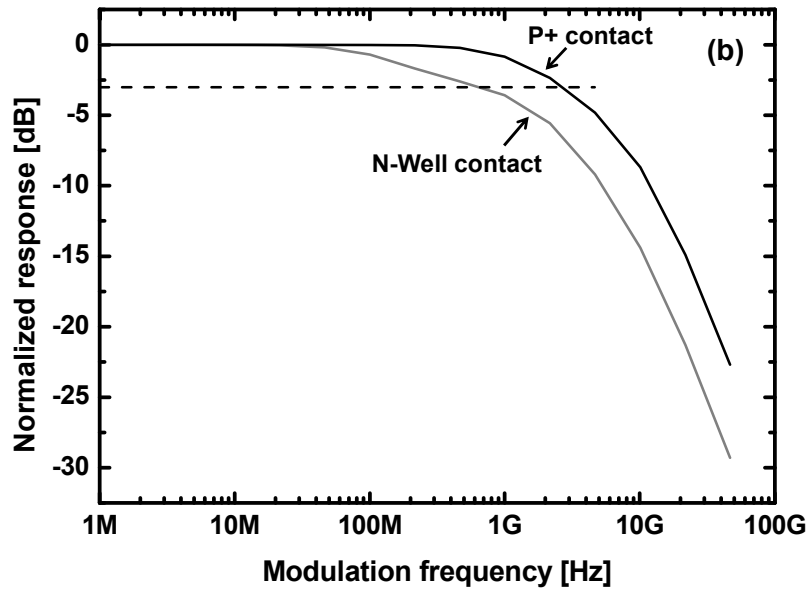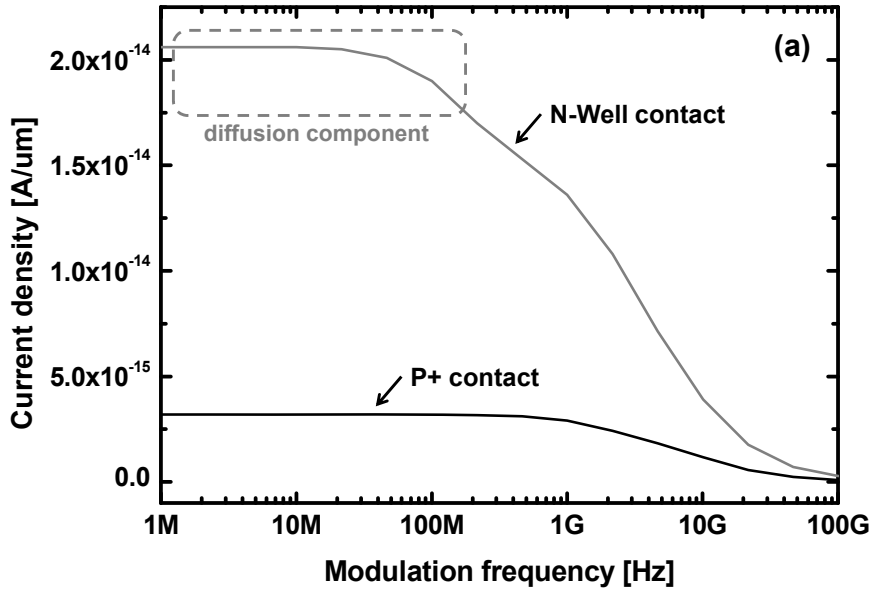
Fig. 2-3. Simulated photodetection frequency responses extracted at P+ contact and N-Well contact: (a) current density and (b) normalized frequency responses.

2-2-2. Influence of the P+ region width on bandwidth

To investigate the influence of lateral diffusion path in the P+ region, the dependence of 3-dB bandwidth on the P+ region width is simulated with TCAD. The device structure is shown in Fig. 2-4 (a). In this simulation, output currents are extracted only from P+ contact and several P+ region widths are chosen for the investigation. Fig. 2-4 (b) shows simulated photodetection frequency responses at different P+ region widths. As the P+ region width increases from 2 μm to 6 μm, the 3-dB bandwidth decreases from 3 GHz to 100 MHz. This is due to increased lateral diffusion path, which can cause slow photogenerated carrier transport in the P+ region.

For the layout of the CMOS-APD, the simulation results for the optimum P+ region width will provide a guideline to determine the finger width of P+ electrodes.

Optical illumination

(a)

P+ contact   N-Well contact   Substrate GND

P+   N+   P+

W

N-Well

P-Substrate

(b)

Normalized response [dB]

0

-5

-10

-15

-20

w = 2 μm

w = 3 μm

w = 6 μm

1M   10M   100M   1G   10G

Modulation frequency [Hz]
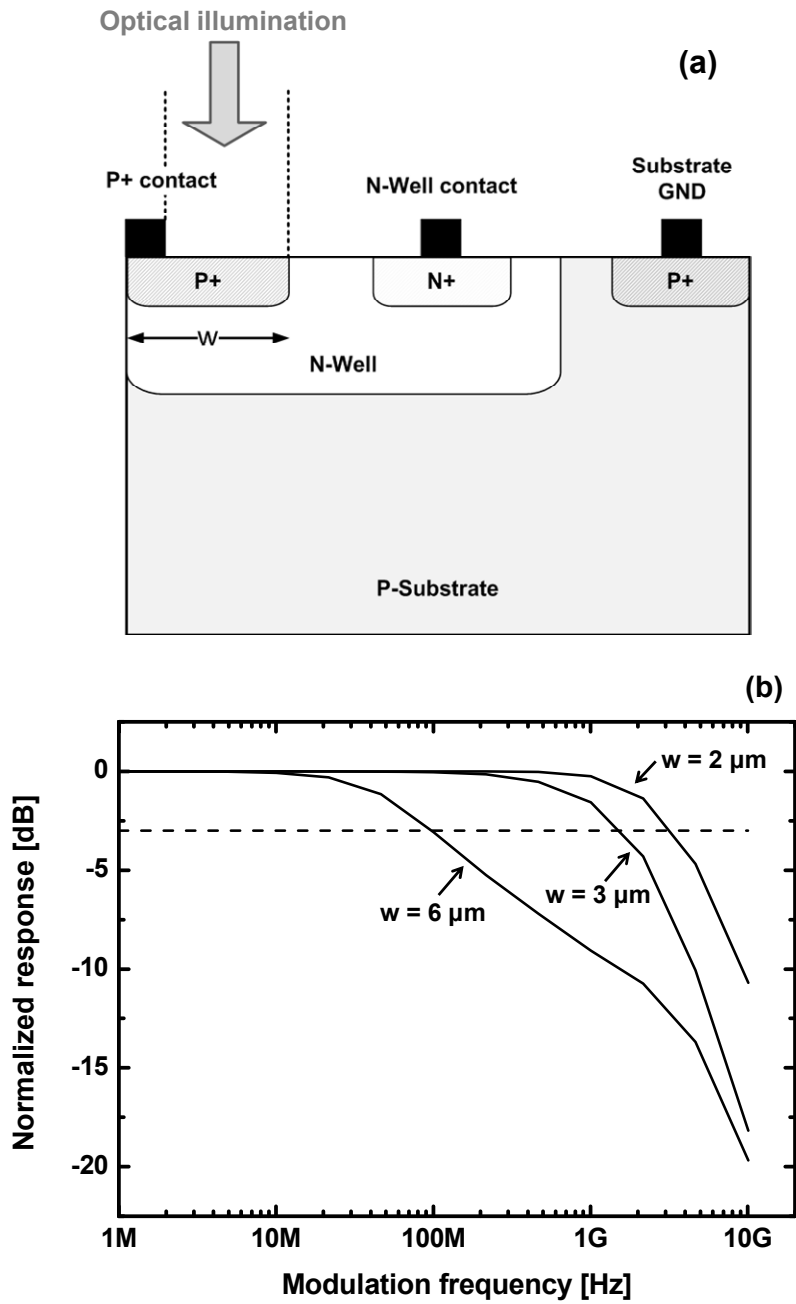
Fig. 2-4. Simulated photodetection frequency response with different P+ region widths of 2 μm, 3 μm, and 6 μm: (a) device structure for simulation and (b) normalized frequency responses.

2-2-3. Electric field profile with and without STI

When high reverse bias voltage is applied to avalanche photodetectors for sufficient avalanche gain, premature edge breakdown can cause several undesired effects as explained in section 2-1. To prevent the edge breakdown in the P+/N-Well junction of the CMOS-APD, shallow trench isolation (STI) can be utilized because dielectric strength of SiO_2 is much higher than breakdown field of silicon [17].

To investigate the influence of STI on lateral periphery of the P+/N-Well junction, electric field profiles in the device are simulated with and without STI structure and the results are shown in Fig. 2-5. Without STI structure, the high electric field in lateral edge of the P+/N-Well junction is clearly observed. This premature avalanche breakdown field in lateral periphery can cause avalanche multiplication of dark current and prevent the photogenerated carriers from having avalanche gain. Whereas, the P+/N-well junction bounded by STI achieves the uniform electric field in entire junction. From the results, it is verified that STI can mitigate the premature edge breakdown in the P+/N-Well junction.
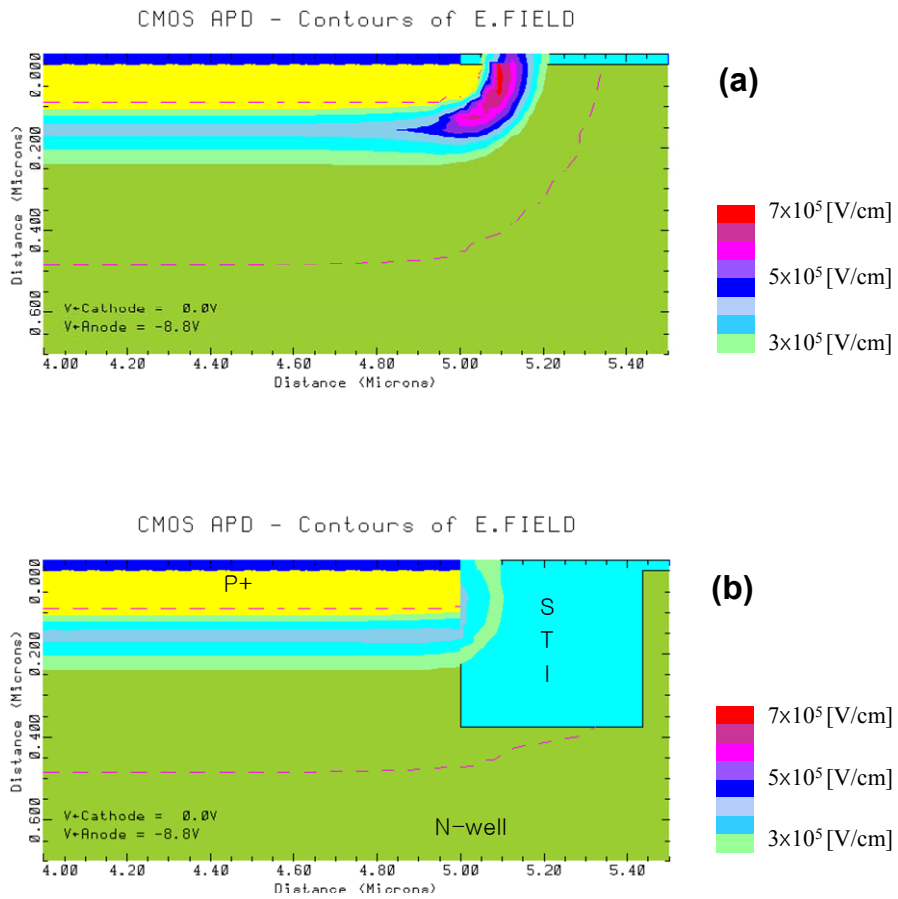
Fig. 2-5. Electric field profiles of P+/N-Well junctions in the CMOS-APD (a) without STI and (b) with STI. (STI: shallow trench isolation)

24

2-3. Structure of the fabricated CMOS-APD

Under design considerations mentioned above, CMOS-APDs were designed and fabricated with 0.18 μm standard CMOS technology. Fig. 2-6 shows cross-sectional device structure and simplified layout of the fabricated CMOS-APD. In the CMOS-APD, output signals are only extracted from P+ contacts to exclude slow diffusion currents generated in P-Substrate. To effectively collect photogenerated carriers, multi-finger electrodes with the finger width of 0.23 μm and spacing of 0.5 μm are formed. Although this narrow finger spacing deteriorates optical coupling efficiency, lateral diffusive transport of the photogenerated carriers was blocked and series resistance was reduced. The shallow trench isolation (STI) surrounded vertical PN-junctions to mitigate edge breakdown in the avalanche regime. The active area is about 30 × 30 μm^2. For injection of optical signals into the CMOS-APD, optical window is formed by blocking the salicide process during the fabrication.
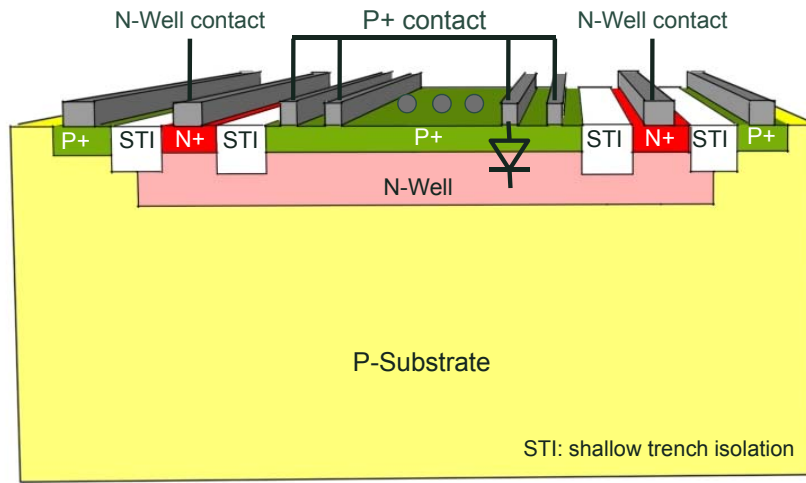
(a)
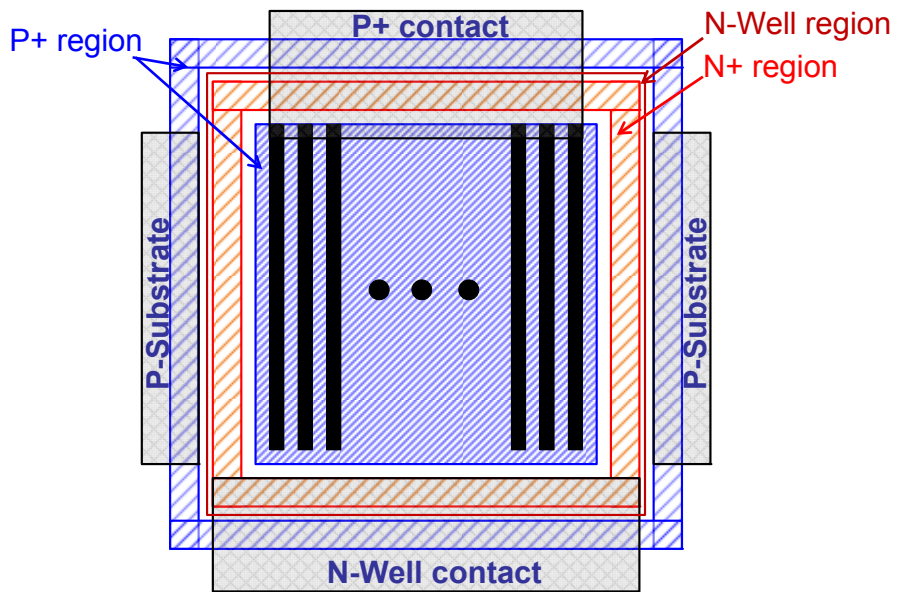
(b)

Fig. 2-6. (a) Cross-sectional structure of the fabricated CMOS-APD.
(b) Simplified layout.

3. Characterization of the fabricated CMOS-APDs

3-1. Experimental setup for characterization of CMOS-APDs

Fig. 3-1 shows experimental setup for characterization of fabricated CMOS-APDs. An 850-nm laser diode followed by a 20-GHz electro-optic modulator was used for generation of modulated optical source. The generated optical signal was injected to the CMOS-APDs through a lensed-fiber having beam spot size of 30 μm at beam waist. Incident optical power was controlled by an 850-nm optical attenuator. The bias voltage of the CMOS-APDs was applied using a semiconductor parameter analyzer (Agilent 4145B). For measurement of photodetection frequency response, a vector network analyzer (Agilent 8719ES) was used to modulate optical signals (Port 1) and detect output signals (Port 2) of the CMOS-APD with prior calibration of cables and RF adaptors as shown in Fig. 3-1 (a). The measured frequency range was from 50 MHz to 13.5 GHz. To investigate impedance characteristics of the CMOS-APDs, two-port S-parameter measurements were performed with the vector network analyzer as shown in Fig. 3-1 (b). All the experiments were done on-wafer.
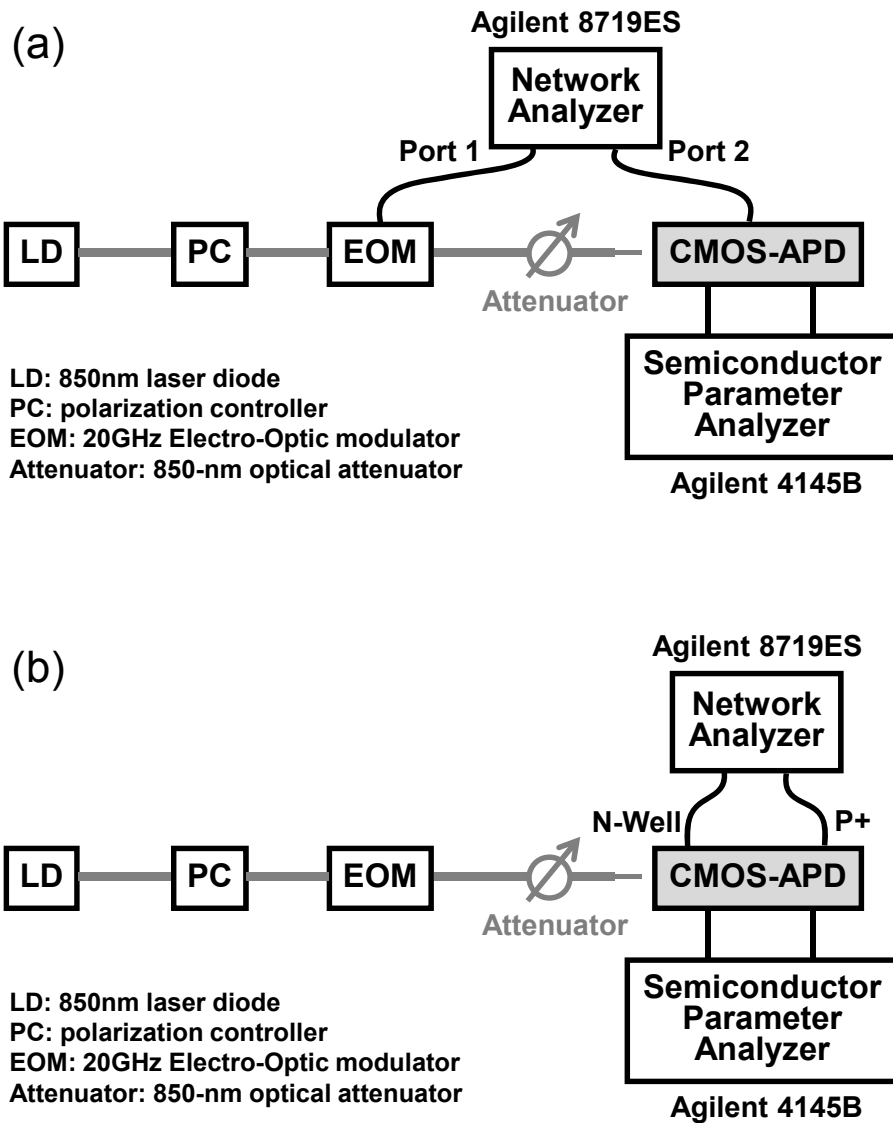
Fig. 3-1. Experimental setup for CMOS-APD characterization: (a) DC, photodetection frequency response, and (b) reflection coefficients measurement.

3-2. DC characteristics

Fig. 3-2 shows measured current-voltage characteristics of the fabricated CMOS-APD with and without optical illumination. When the optical signal is injected to the CMOS-APD, current are increased due to the photogenerated carriers. With the increasing reverse bias voltage, dark current remains nearly constant and start to increase at the breakdown voltage ($V_{BK,dark}$) of 10.2 V due to avalanche multiplication process. Under optical illumination, on the other hand, the current gradually increases at low reverse bias voltage and start to dramatically increase at V_R around 9.5 V owing to the enlarged depletion width and enhanced impact ionization caused by the photogenerated carriers, respectively. The fabricated CMOS-APD exhibits low dark current below a few nA at V_R below 10.1 V.

In avalanche photodetectors (APDs), avalanche multiplication factor (M) – shortly avalanche gain – is a key parameter, which represents internal amplification of photogenerated carriers caused by avalanche multiplication process. The photocurrent (I_{ph}), responsivity (R), and avalanche multiplication factor (M) are defined as following [22]:

$$I_{ph} = I_{illumination} - I_{dark} \quad [A] \tag{3.1}$$

29

$$R = \frac{I_{ph}}{P_{opt}} \quad [\text{A/W}] \tag{3.2}$$

$$M(V) = \frac{I_{ph}(V)}{I_{ph}(V_0)} = \frac{I_{illumination}(V) - I_{dark}(V)}{I_{illumination}(V_0) - I_{dark}(V_0)} \tag{3.3}$$

where, $I_{illumination}$ is the current under illumination, I_{dark} is the current under dark condition, P_{opt} is the incident optical power, and V_0 is the reference voltage in which no avalanche gain is observed.

From the measured current-voltage characteristics, responsivity and avalanche multiplication factor of the CMOS-APD were calculated and the results are shown in Fig. 3-3. For the calculation of avalanche multiplication factor, the reference voltage in which the CMOS-APD provides no avalanche gain was set to V_R of 1 V. As V_R increases, responsivity and avalanche gain increase, and they have maximum value at V_R of 10.2 V. The fabricated CMOS-APD has maximum responsivity of 3.19 A/W and avalanche multiplication factor of 1250 at 10.2 V under 0.1 mW optical illumination. Above the maximum avalanche-gain voltage, responsivity and, avalanche multiplication factor start to decrease. These are due to space charge effect and thermal heating [17]. When the CMOS-APD operates well into the avalanche regime, the current density becomes very high, and

consequently, carrier space charges are generated and junction temperature increases. Accordingly, avalanche multiplication factor decreases due to decreased ionization rates.
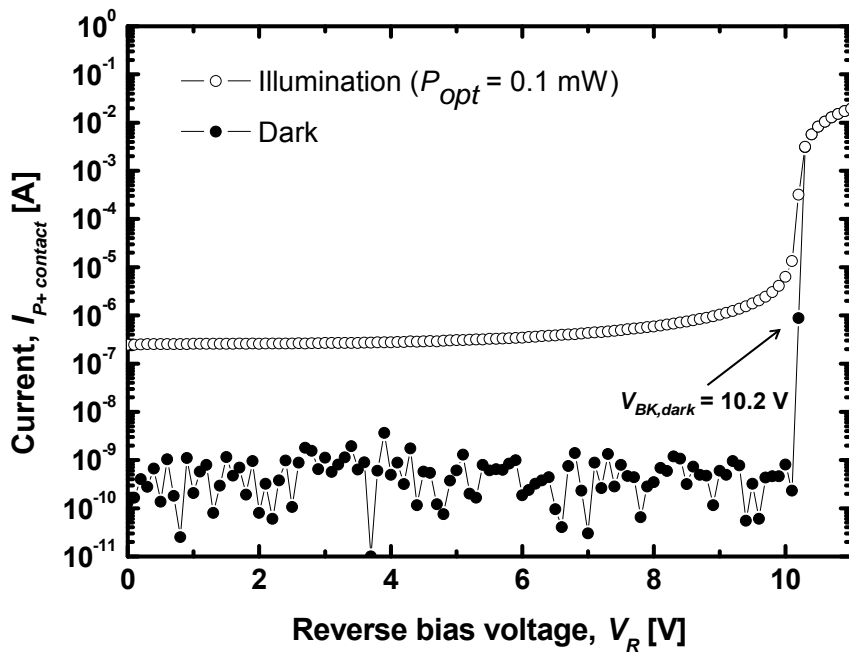
Fig. 3-2. Current-voltage characteristics of the fabricated CMOS-APD under dark and illumination. Incident optical power (P_{opt}) is 0.1 mW.
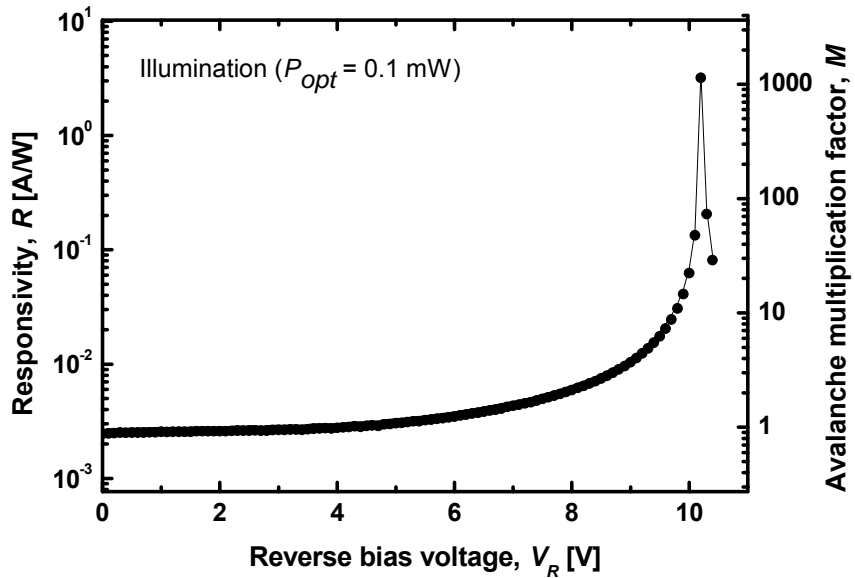
Fig. 3-3. Responsivity and avalanche multiplication factor (*M*) as a function of the reverse bias voltage (*V_R*) under 0.1 mW optical illumination.

With the same reason, the decrease in avalanche multiplication factor also can be observed when the incident optical power is sufficiently high, thus the current density is increased. Fig. 3-4 shows avalanche gains as a function of incident optical power at V_R of 10.0 and 10.2 V. At V_R of 10.0 V, the avalanche multiplication factor is independent on incident optical power because the current density is low enough not to cause the space charge effect or junction temperature change. However, at V_R of 10.2 V which provides maximum avalanche gain, thus high current density, the avalanche multiplication factor decreases with increasing incident optical power. This is due to the increased current density by the photogenerated carriers.
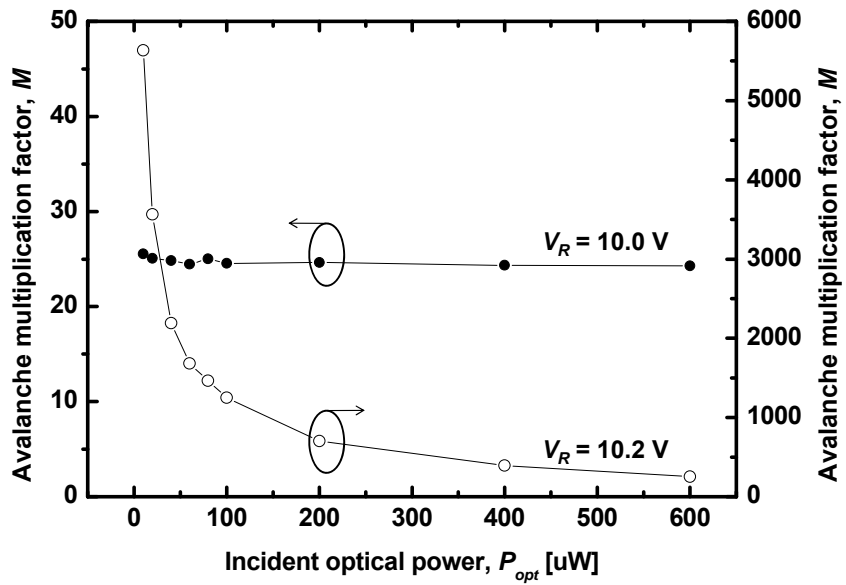
Fig. 3-4. Avalanche multiplication factors as a function of incident optical power at V_R of 10.0 and 10.2 V.

To examine the physical origin of breakdown mechanism of the CMOS-APD, the temperature dependence of current-voltage characteristics were measured and the results are shown in Fig. 3-5. The increase of breakdown voltage ($V_{BK,dark}$) with increasing temperature verifies that the breakdown is attributed to the avalanche process instead of the tunneling effect, which has negative temperature coefficient [17].
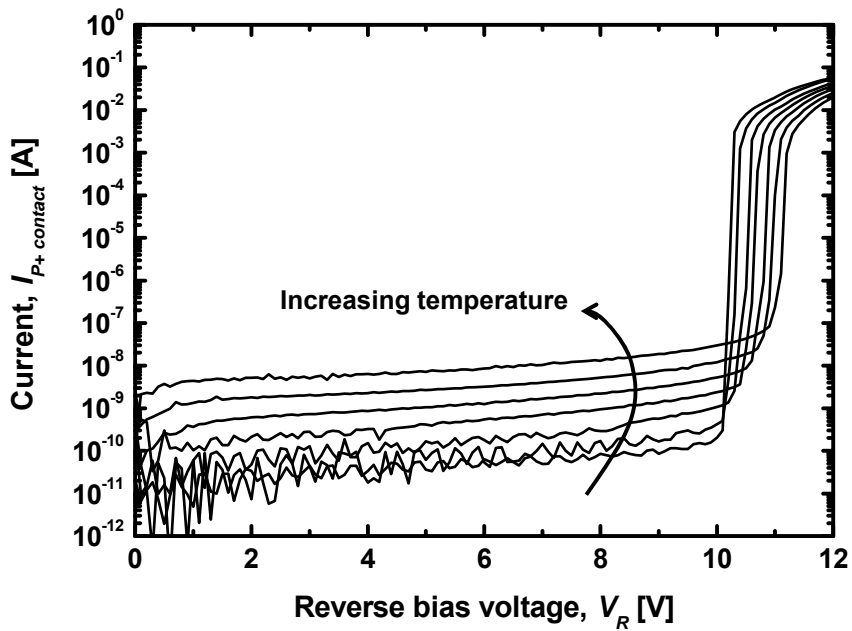
Fig. 3-5. Current-voltage characteristics of the fabricated CMOS-APD at different temperatures under dark condition. The temperature increases from room temperature (about 25 °C) to 175 °C with 25 °C increments.

3-3. Photodetection frequency responses

Fig. 3-6 (a) shows photodetection frequency responses of the CMOS-APD at different reverse bias voltages when the incident optical power is 0.2 mW. The enlarged current-voltage characteristic near $V_{BK,dark}$ was also shown in Fig. 3-6 (b) to designate the measurement voltages for the photodetection frequency response. As described in the previous section, the CMOS-APD has maximum avalanche multiplication factor at V_R of 10.2 V, and accordingly the photodetected signal power of the modulated optical signal is maximized in this condition.

At V_R larger than $V_{BK,dark}$, it is interestingly observed that photodetection frequency response has rf peaking at high frequency of a few GHz. Such rf peaking has been also reported in InGaAs/InAlAs APD due to the generation of space-charge instability [23]. For further investigation of the rf peaking effect in the CMOS-APD, dependences of photodetected frequency responses on incident optical power were measured and the results are shown in Fig. 3-7. The incident optical power increases from 0.2 mW to 1.0 mW with 0.4 mW increments. With increasing optical power, bandwidth of the CMOS-APD is increased from about 1.2 GHz to 2.6 GHz at V_R of 10.2 V as shown in Fig. 3-7 (a). Similarly, at V_R of 10.3 V, the rf-peaking effect is enhanced

as incident optical power increases.
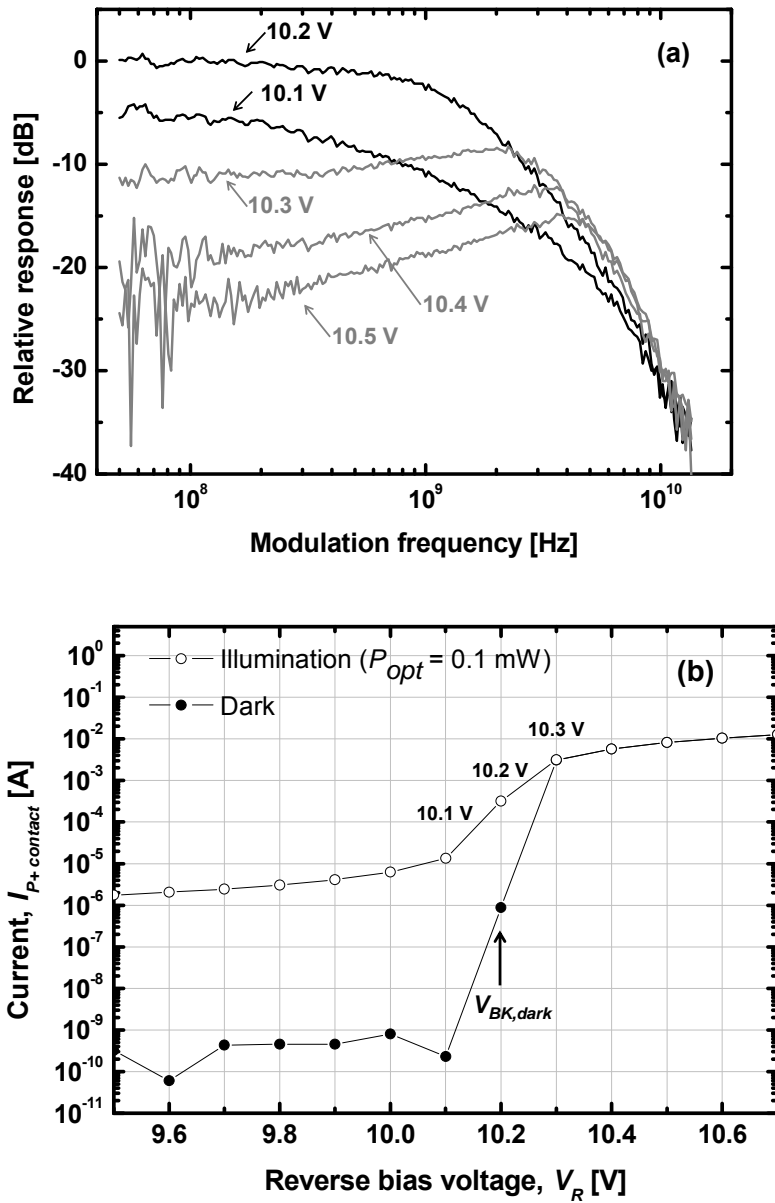
Fig. 3-6. (a) Photodetection frequency responses at different V_R when incident optical power is 0.2 mW. (b) Enlarged current-voltage characteristics near $V_{BK,dark}$ to clearly show measurement condition.

37
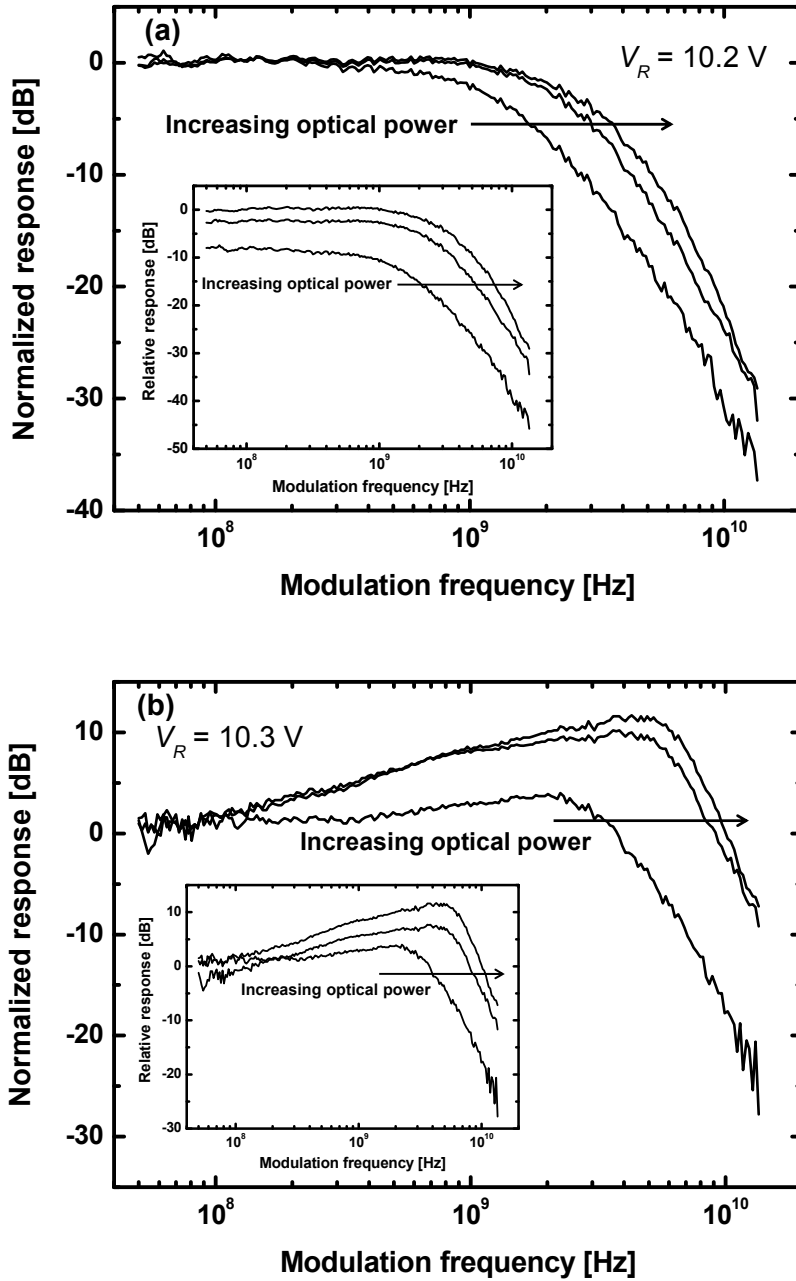
Fig. 3-7. Photodetection frequency responses of the CMOS-APD with different optical powers at (a) V_R of 10.2 V and (b) V_R of 10.3 V. Incident optical power increases from 0.2 mW to 1.0 mW with 0.4 mW increments. Insets show relative responses without normalization.

From the measurement of photodetection frequency responses, it is concluded that rf peaking is more likely appeared in the following conditions:

- Reverse bias voltage is high (e.g. V_R is larger than $V_{BK,dark}$).
- Incident optical power is high.

In other words, the rf-peaking effect is caused by high current density when the CMOS-APD operates in the avalanche regime.

The rf peaking is attributed to the avalanche inductance in the CMOS-APD and the physical origin will be discussed in the next section. With equivalent circuit modeling by measurement of impedance characteristics, the inductive component, which is dependent on the current density, will be investigated.

3-4. Equivalent circuit modeling

3-4-1. Impedance characteristics of the CMOS-APD

As in transit-time diodes such as impact ionization avalanche transit-time (IMPATT) diodes, the CMOS-APD has an inductive component in the avalanche region. Fig. 3-8 shows a simplified IMPATT diode model having avalanche, drift, and inactive regions [17]. In the model, one-sided abrupt junction of p+-n-n+ structure is assumed, thus the characteristics of the avalanche region can be applicable to the CMOS-APD, which has P+/N-Well/N+ structure as shown in Fig. 2-2 (a). With small-signal analysis, total ac current density in the avalanche region can be divided into avalanche conduction current density (J_A) and displacement current density (J_{Ad}). Using Poisson's equation and continuity equations, these currents can be derived as [17],

$$J_A = \frac{2\alpha' x_A J_0 \mathrm{E}_A}{j\omega\tau_a}$$
$$J_{Ad} = j\omega\varepsilon_s \mathrm{E}_A$$
$$\alpha' \equiv \partial\alpha / \partial\mathrm{E}$$
$$\tau_a = x_A / v_s$$

(3.4)

where, α' is derivative of ionization coefficient with respect to the electric field (E), x_A is the width of the avalanche region, J_0 is dc current density, ε_s is dielectric constant of semiconductor, E_A is the ac electric field in the avalanche region, τ_a is the transit time across the multiplication region, and v_s is saturation velocity.

From the relation between the current density and the electric field in (3.4), it can be seen that the avalanche conduction current density (J_A) varies inversely with ω as in an inductor. Whereas, the displacement current density (J_{Ad}) varies proportional to ω as in a capacitor. Accordingly, the avalanche region can be modeled as a parallel LC circuit as shown in Fig. 3-8. The inductance and capacitance are given as

$$
\begin{aligned}
L_A &= \frac{\tau_A}{2I_0\alpha'} \\
C_A &= \frac{\varepsilon_s A}{x_A}
\end{aligned}
\tag{3.5}
$$

where, I_0 is the dc current and A is the junction area.

To examine the validity of the LC model in the avalanche region, impedance characteristics of the CMOS-APD were investigated. Fig. 3-9 shows reflection coefficients on Smith chart. The S-parameters were

41

measured at the P+ port of the CMOS-APD with applying different bias voltages when incident optical power is 0.5 mW. Measurement frequency was from 50 MHz to 13.5 GHz. At the reverse bias voltage below $V_{BK,dark}$, V_R of 9.0 and 10.0 V, the CMOS-APD only have capacitive and resistive components as in conventional p-i-n PD model [18]. However, at V_R larger than $V_{BK,dark}$, the reactance of the CMOS-APD has the inductive component, which is designated by upper side plot of reflection coefficients on Smith chart. Because avalanche inductance is dependent on the current of the device in the avalanche region as explained in (3.5), impedance characteristics of the CMOS-APD varies with bias voltage change. Inset of Fig. 3-9 also shows the measured current at the P+ port of the CMOS-APD. From the impedance measurement, it is concluded that the CMOS-APD has the inductive component as well as the capacitive component when the device operates in the avalanche regime with large dc current.
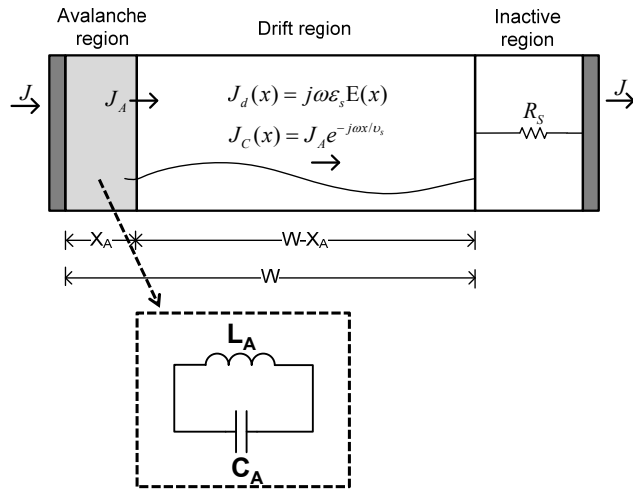
Fig. 3-8. IMPATT diode model for describing the avalanche region, drift region, and inactive region of PN-junction diodes.

V_R	$I_{P+ contact}$
9.0 V	5.2 µA
10.0 V	55.0 µA
10.3 V	3.9 mA
10.4 V	5.7 mA
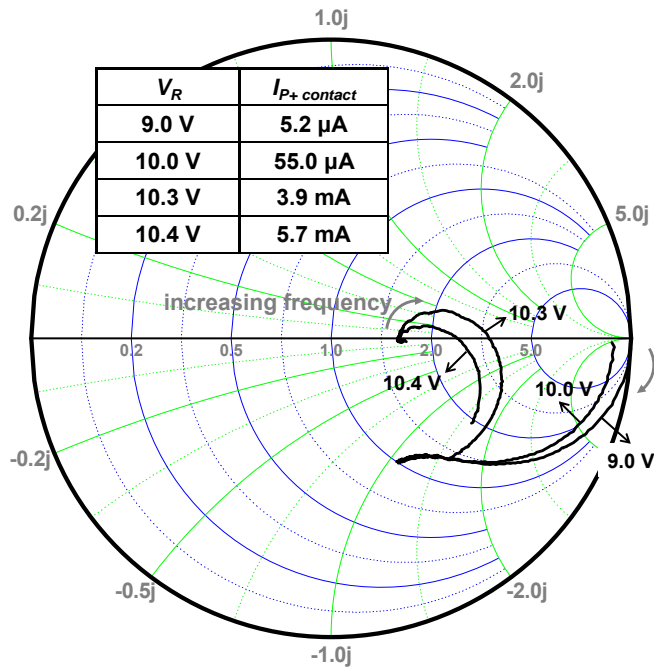
Fig. 3-9. Reflection coefficients of the CMOS-APD at the output port (P+ contact) with different bias voltages when 0.5 mW optical signal is injected. The inset table shows measured current values.

3-4-2. Equivalent circuit model for the CMOS-APD

With the inductive and capacitive components in the avalanche region, equivalent circuit modeling for the CMOS-APD was performed. Fig. 3-10 shows proposed equivalent circuit model when the device operates in the avalanche regime. For accurate modeling of the device operation, several components were added with avalanche components.

To account for the dissipative effect due to the finite reverse saturation current and the field-dependent velocity, series and parallel resistors, R_a and R_l are included in the P+/N-Well junction diode region, respectively [24]. In $Z_{P+/N-Well}$, capacitor, C, represents total depletion capacitance formed in P+/N-Well junction and this can be approximated as $\varepsilon_s A/W_D$, where ε_s is dielectric constant of silicon, A is junction area, and W_D is the depletion width. The drift region resistance, R_d, is given as $W_d/2A\varepsilon_s v_s$, where W_d is the drift region width and v_s is the saturation velocity of carriers in silicon [17]. R_s is the resistance in the inactive region caused by the low doped N-Well in the CMOS-APD.

Outside the P+/N-Well junction diode region, parasitic components and diode model for N-Well/P-Substrate junction were modeled. For the measurement of the devices, ground-signal-ground (GSG) pads were implemented. Due to the interconnect lines and electrodes for connecting the device, parasitic RLC components (Z_{para1}, Z_{para2}, and

Z_{para3}) are generated. To model the N-Well/P-Substrate junction diode, RC components including R_{well}, C_{sub1}, C_{sub2}, and R_{sub} are used. R_{well} is N-Well resistance, C_{sub1} is the capacitance between N-Well, C_{sub2} and R_{sub} are parasitic components in silicon substrate [25].

For consideration of photogenerated carriers, a current source is modeled as shown in Fig. 3-10. When the optical signal is injected to device, carriers are generated not only in the depletion region but also in the charge neutral region due to the long absorption coefficient of 14 μm at 850 nm in silicon. Consequently, slow diffusion currents, which limit the speed of the CMOS-APD, caused by the photogenerated carriers in the charge neutral region should be considered for the current source model. The diffusive transport of the carriers can be modeled with transit-time constant (τ_{tr}) and the current source having single-pole frequency response with $f_{3dB}=1/(2\pi \tau_{tr})$ is used for modeling of the photogenerated current.
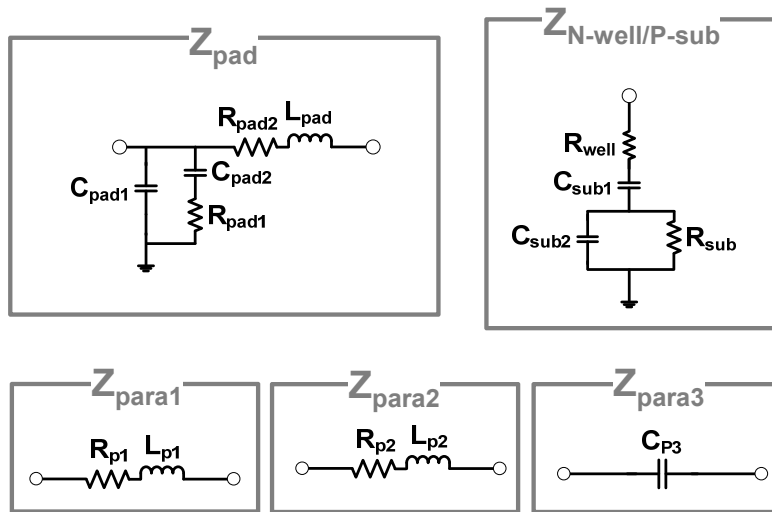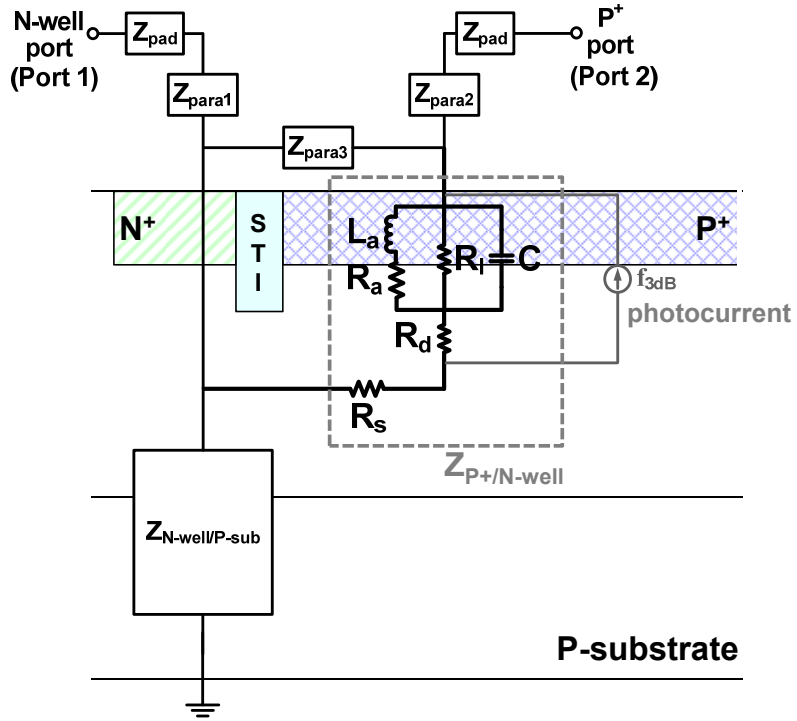
Fig. 3-10. Equivalent circuit model for the CMOS-APD.

3-4-3. Parameter extraction

Using the equivalent circuit model, extraction of all the circuit parameters was performed. From the measurement of two-port S-parameters, Y- and Z-parameters were obtained. To extract circuit parameters of pad structure, open and short test patterns without diode structure were used. After de-embedding Z_{pad}, circuit parameters of Z_{para1} and $Z_{N\text{-well/P-sub}}$ were extracted by de-embedded Z_{11} - Z_{12} and Z_{12}. The parameters for Z_{para2} were initially set to the same value of Z_{para1}, and Z_{para3} was calculated using the layout dimensions of metal layers. The estimated values were refined by parameter tuning and optimization by comparing measured data to simulation results. For the parameters of $Z_{P+/N\text{-well}}$, L_a, C, and R_d were initially calculated from equations, and then refined.

Table 3-1 shows all the extracted parameters at the bias current of 0.3, 0.4, and 0.5 mA. To investigate the dependence of parameter value on the current (I_0) of the CMOS-APD, S-parameter measurements were done with the current bias. It is seen that the avalanche inductance, L_a, is inversely proportional to the bias current as indicated in (3.5). Although C, R_d, and R_s are dependent on the depletion, drift, and inactive region width, the change with respect to the bias current is very little. Accordingly, the parameters can be assumed to be independent on

the bias condition.

To obtain transit-time constant for the current source model, photodetection frequency responses were used. For the estimation of transit-time constant in N-Well, calculation of diffusion time constant ($\tau_{diffusion}$) was performed using (2.3). The diffusion length (l_0) of 0.55 μm and diffusion coefficient (D) of 7.8 cm^2/s were assumed with doping concentration of 1.5 × 10^{17} in N-Well. Extracted f$_{3dB}$, which corresponds to transit-time constants, in Table 3-1 are comparable with estimated values.

All the extracted parasitic components are presented in Table 3-2.

Table 3-1. Extracted circuit parameters of $Z_{P+/N-Well}$.

	0.3 mA	0.4 mA	0.5 mA
L_a [nH]	14	10.5	8.4
R_a [Ω]	105	50	25
R_l [Ω]	780	540	410
C [fF]	190	190	190
R_d [Ω]	4.2	4.2	4.2
R_s [Ω]	40	40	40
f_{3dB} [GHz]	1.18	0.92	0.81

Table 3-2. Extracted parasitic components.

Z_{pad}		$Z_{para1,2,3}$		$Z_{N-well/P-sub}$	
C_{pad1} [fF]	55	R_{p1} [Ω]	10	R_{well} [Ω]	30
C_{pad2} [fF]	5	L_{p1} [nH]	0.1	C_{sub1} [fF]	300
R_{pad1} [kΩ]	2.5	R_{p2} [Ω]	22	C_{sub2} [fF]	200
R_{pad2} [Ω]	1	L_{p2} [nH]	0.1	R_{sub} [Ω]	280
L_{pad} [pH]	35	C_{p3} [fF]	210		

Fig. 3-11 shows measured reflection coefficients and simulated results using the model at the bias current (I_0) of 0.3, 0.4, and 0.5 mA. It is seen that the simulation results are well matched to measured data, correspondingly the equivalent circuit model represents the operation of the CMOS-APD fairly well.

Fig. 3-12 shows measured photodetection frequency responses and simulated results with the model having the current source for the photogenerated carriers. With the current source having one-pole frequency response, the equivalent circuit model also efficiently reflects photodetection performance of the CMOS-APD. To investigate the effect of transit-time constant, simulation of photodetection frequency responses were performed under two conditions at I_0 of 0.3 mA: (1) without the transit-time effect by using a frequency-independent current source and (2) with consideration of only the transit-time effect by using the one-pole current source without any other equivalent circuit components. From the results, it is observed that the rf-peaking effect can be more easily appeared without the transit-time effect and the diffusion component in the N-Well region severely limit the speed of the CMOS-APD.
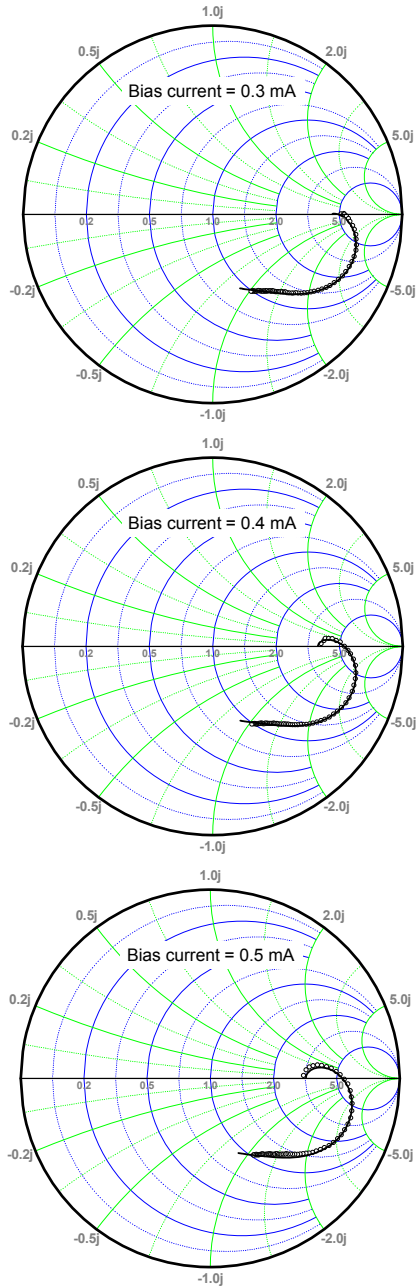
Fig. 3-11. Measured and fitted reflection coefficient at the P+ port under 1 mW optical illumination. Hollow circles show measured data and solid lines represent fitted results using the model.
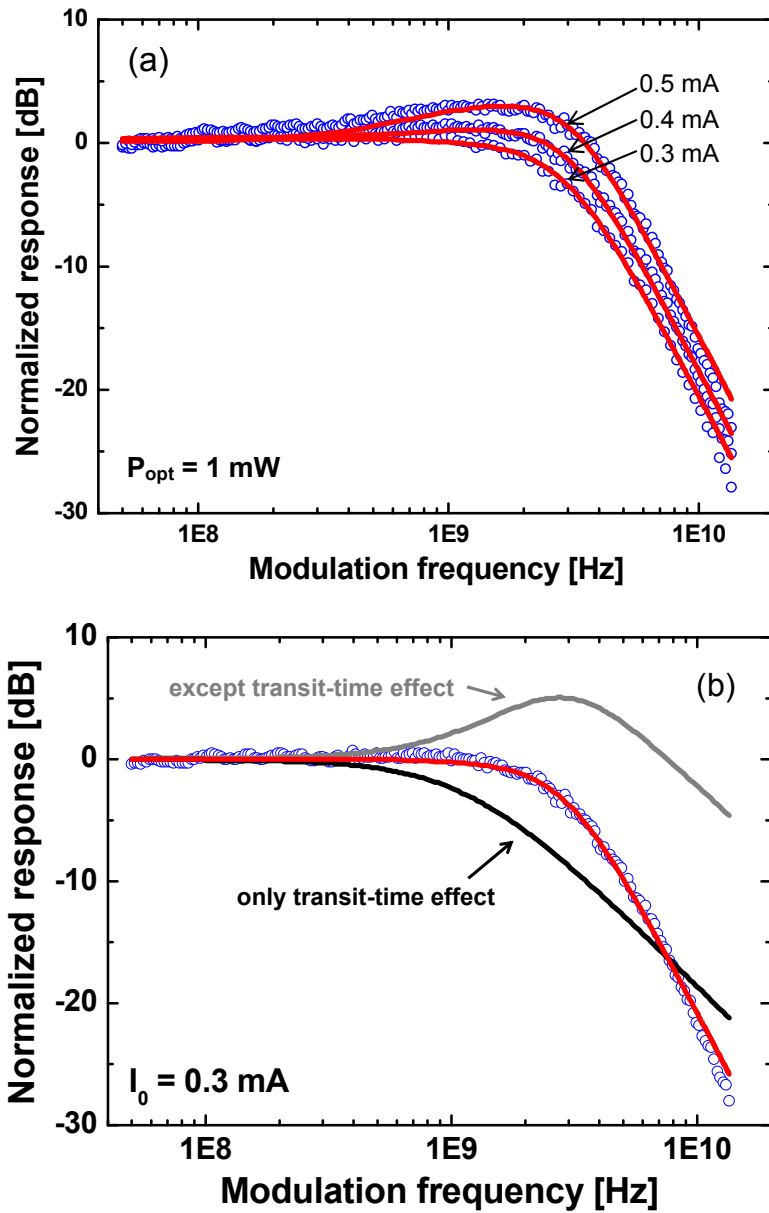
Fig. 3-12. (a) Measured photodetection frequency responses and simulation results with the model at different bias currents. (b) The rf peaking effect and the transit-time effect on the photodetection frequency response.

4. 6.25-Gbps wireline data transmission using the CMOS-APD

4-1. Optical receiver using the CMOS-APD

To perform data transmission using the CMOS-APD, an optical receiver was implemented using chip-on-board (CoB) technique in which semiconductor chips are directly attached onto a board with bond-wires. To convert photocurrents into voltage signals with amplification, a commercially available transimpedance amplifier (ADN2882 from Analog Devices) was connected to the output of the CMOS-APD with wire-bonding. The transimpedance amplifier has gain and bandwidth of about 60 dB·Ω and 3.5 GHz, respectively. Fig. 4-1 shows a schematic and a photograph of the fabricated optical receiver based on the CMOS-APD (CMOS-APD receiver).

In the CMOS-APD receiver, the output port (P+ contact) of the CMOS-APD is internally biased about 0.85 V due to virtually-shorted input stage of the transimpedance amplifier as shown Fig. 4-1 (a). To maintain the same reverse voltage across the P+/N-Well junction, higher voltage by the amount of about 0.85 V should be applied to the N-Well port. For the connection between the CMOS-APD output and the transimpedance amplifier input, bond-wires are used and these

interconnects induce inductive components.
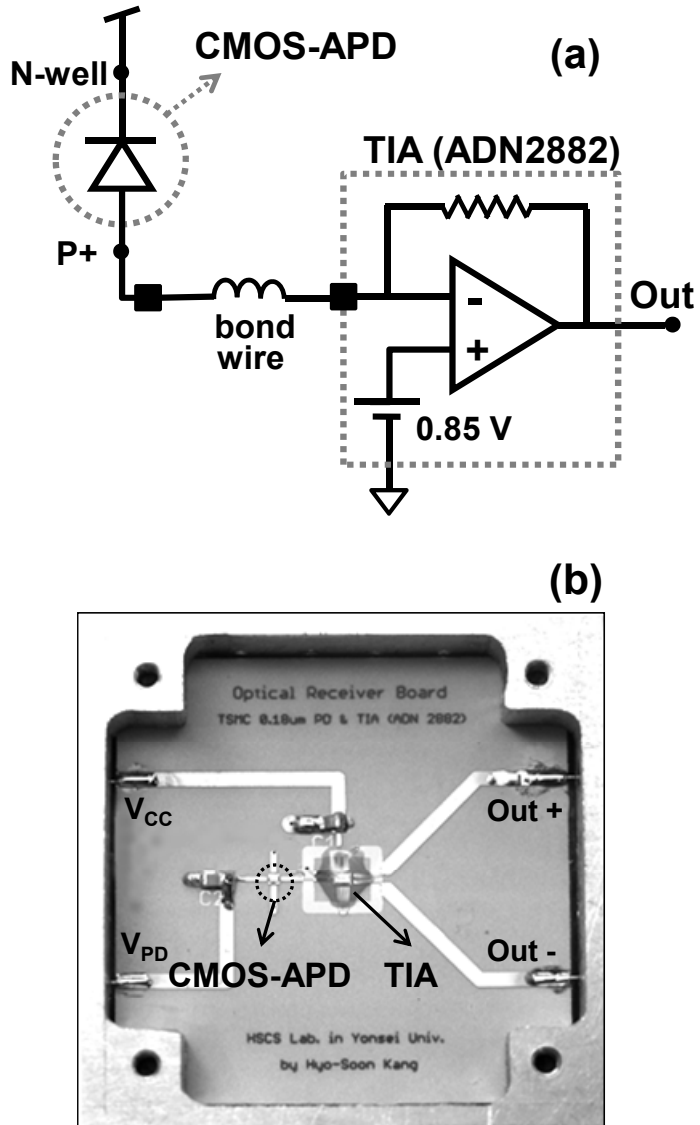
Fig. 4-1. (a) A schematic of optical receiver having the CMOS-APD and the transimpedance amplifier on a board. (b) A photograph of the fabricated CMOS-APD receiver.

The series inductances caused by bond-wires can be beneficial for bandwidth enhancement of optical receivers with the help of the series inductive peaking effect [26]. Fig. 4-2 shows photodetection frequency responses of the CMOS-APD and the CMOS-APD receiver. For the measurement, the bias voltage applied to the N+ port in optical receiver is 11 V, which effectively induces the reverse bias voltage of 10.15 V across the PN-junction of the CMOS-APD. It is observed that the overall bandwidth of the CMOS-APD receiver is enhanced to 4.4 GHz due to series inductive peaking realized by bond-wire inductance.
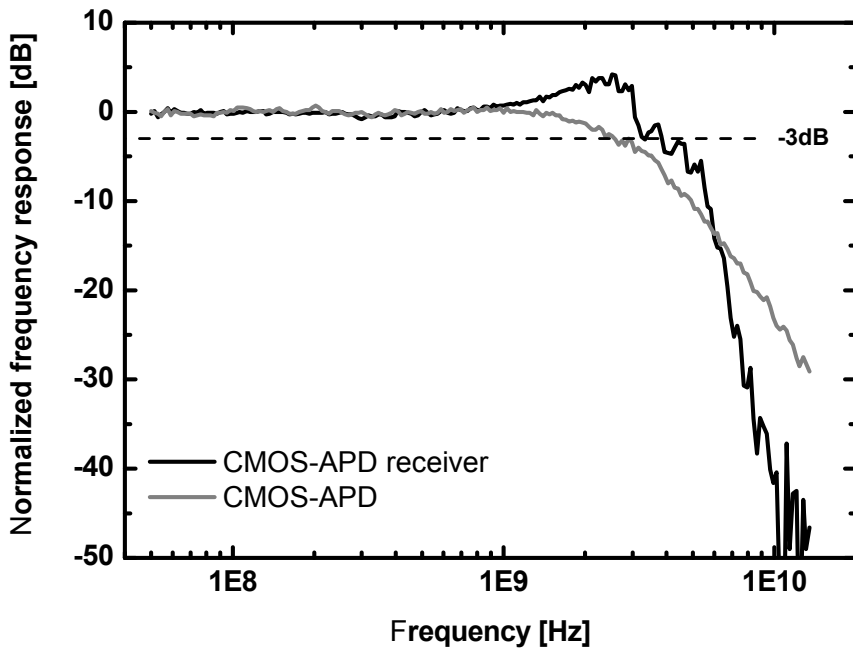
Fig. 4-2. Photodetection frequency responses of the CMOS-APD and optical receiver.

4-2. Experimental setup for 6.25-Gbps data transmission

6.25-Gbps data transmission was demonstrated using the optical receiver based on the CMOS-APD. Fig. 4-3 shows experimental setup. For optical source, an 850-nm laser diode and electro-optic modulators were used and 6.25-Gbps data from pulse-pattern generator were injected to the modulator. At the output of optical receiver, a limiting amplifier was used for boosting up the output signals to satisfy the dynamic range of Bit Error Rate (BER) measurement (BERTScope 12500A). The optical signal is injected to the CMOS-APD using a lensed fiber and optical power was controlled by an optical attenuator to measure optical receiver sensitivity.
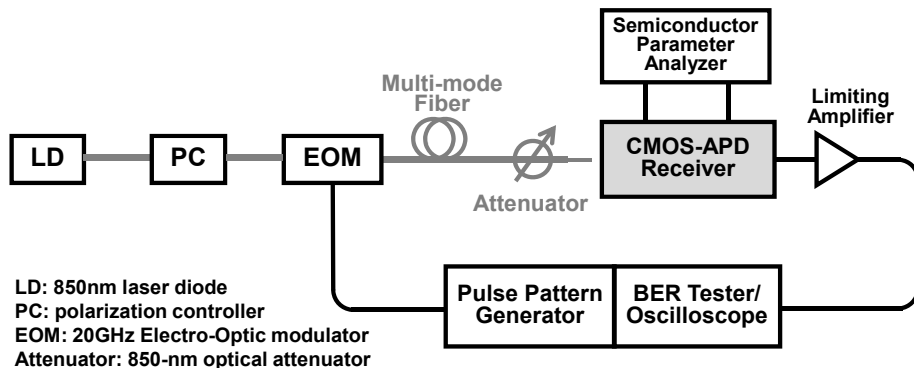
Fig. 4-3. Experimental setup for 6.25-Gbps data transmission using the optical receiver based on the CMOS-APD.

4-3. Data transmission results

Using the CMOS-APD receiver having the CMOS-APD and the transimpedance amplifier, 6.25-Gbps data were transmitted. Bit error rate (BER) was measured with control of incident optical power into the CMOS-APD as shown in Fig. 4-4. When incident optical power is -2 dBm, error free transmission in which BER less than 10^{-12} is observed for the measurement time of about 10 minutes. At P_{opt} of -2 dBm, eye diagram of the output signal is also shown in Fig. 4-4 (b). It is seen that 6.25-Gbps data have clear eye-opening. However, to improve sensitivity of the CMOS-APD receiver, further research for increasing responsivity as well as careful design of an integrated optical receiver to optimize noise performance is required.

Table 4-1 shows the performance comparison of published results with this work. The fabricated CMOS-APD receiver is capable of data transmission for the largest data rate of 6.25 Gbps although further optimization is still required.
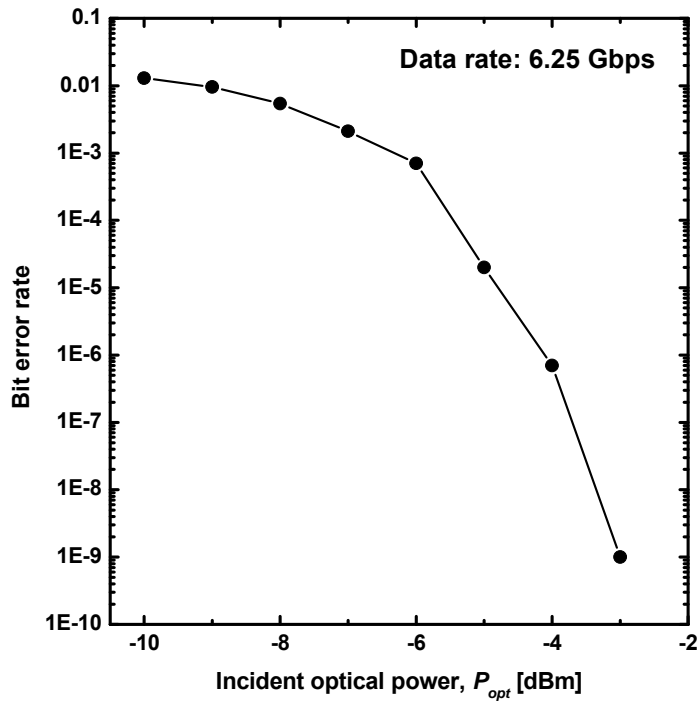
(a)
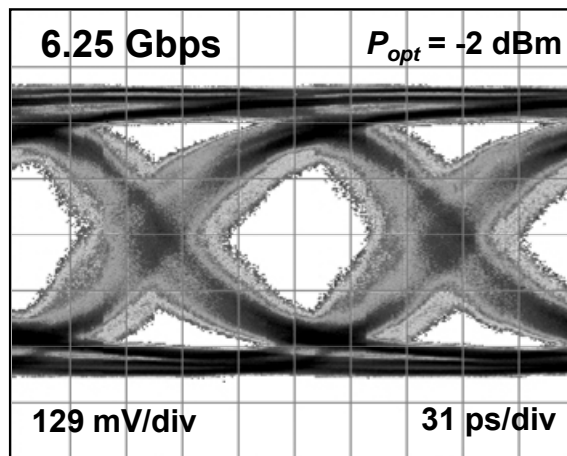
(b)

Fig. 4-4. 6.25-Gbps data transmission results: (a) BER characteristics as a function of incident optical power and (b) eye diagram at P_{opt} = -2 dBm.

Table 4-1. Performance comparison of optical receivers based on CMOS-compatible photodetectors.

Year	**2008**	2007	2005	2005	1999
Reference	**This work**	PTL [15]	JSSC [14]	PTL [8]	J.STQE [11]
Process	**0.18 μm**	0.18 μm	0.18 μm	0.18 μm	0.35 μm
Optical receiver	**Board: PD and TIA**	PD only	Integrated: PD, TIA, and EQ	Integrated: PD, TIA, and LA	Integrated: PD and Preamplifier
PD bandwidth	**2.6 GHz**	1.6 GHz	< 10 MHz	1.1 GHz	N.A.
PD responsivity	**0.34 A/W**	0.74 A/W	N.A.	0.02 A/W	0.04 A/W
Data Rate	**6.25 Gbps**	3.5 Gbps	3 Gbps	2 Gbps	1 Gbps
Sensitivity at BER	**-2 dBm at 10^{-12}**	N.A.	-19 dBm at 10^{-11}	-8 dBm at 10^{-9}	-6.3 dBm at 10^{-9}

5. Utilization of CMOS-APDs for fiber-fed 60-GHz self-heterodyne wireless systems

5-1. Fiber-fed 60-GHz self-heterodyne wireless systems

Due to the advantages of both millimeter-wave band and fiber-optic technology, fiber-fed millimeter-wave wireless systems have been widely investigated [27-31]. In particular, 60-GHz band provides such advantages of large license-free band of about 7 GHz [32], [33], high free-space loss for frequency reusability [34], high directivity mitigating multi-path fading, and short-wavelength enabling small RF components. Together with these advantages of 60-GHz band, fiber-optic technology can provide a low loss, high capacity, and flexible data transmission medium to connect large amounts of base stations with existing fiber networks.

To realize fiber-fed 60-GHz wireless systems, one approach is remote up-conversion scheme as shown in Fig. 5-1 (a). At central stations, broadband data at low IF are distributed to base stations through optical fibers. In base stations, transmitted data at IF are photodetected, and then frequency up-converted to 60-GHz band using a photodetector and 60-GHz components including a phase-locked oscillator, a mixer and amplifier. Finally, these frequency up-converted

data at 60-GHz band are radiated to free space, and transmitted to mobile terminals. The received data at mobile terminals are frequency down-converted to IF band, and demodulated. Although the remote up-conversion scheme does not require high performance optical components operating at millimeter-wave band, RF components at base stations and mobile terminals are complicated to perform frequency up/down-conversion, thus implementation cost is increased. Accordingly, cost reduction for wide deployment of base stations having small cell size and simplification of the mobile terminal are critical issue.

To overcome the problem of RF system complexity, millimeter-wave self-heterodyne wireless systems have been proposed [35], [36]. Fig. 5-1 shows a fiber-fed 60-GHz self-heterodyne system (Fig. 5-1 (b)) compared with a conventional fiber-fed 60-GHz super-heterodyne system (Fig. 5-1 (a)). The most remarkable feature of millimeter-wave self-heterodyne systems is transmission of local oscillator (LO) signal together with RF signal at RF transmitters, which corresponds to base stations in fiber-fed wireless systems. At the mobile terminals, frequency down-conversion of received data at RF band can be performed by self-mixing of RF and LO signals using a square-law device. Owing to this operation principle, the millimeter-wave self-

heterodyne wireless system provides following advantages [35], [36].

- **No need for LO and image rejection filter at base stations (RF transmitters):** Because LO as well as RF signals are transmitted simultaneously at base stations, LO and image rejection technique for a mixer as in the conventional super-heterodyne system is not required.

- **No need for LO in the mobile terminal**: Due to the frequency down-conversion method of self-mixing between LO and RF signals by the square-law device, LO can be eliminated in mobile terminals.

- **Phase noise and frequency offset immunity**: When the RF signal is down-converted by self-mixing process with the received LO signal, phase noise and frequency offset caused at base stations can be eliminated due to noise cancellation. Consequently, complexity of realizing LO signal at base stations can be reduced because phase-locking techniques to generate stable LO signal as in the super-heterodyne system is not required.

For these advantages, the self-heterodyne system is adopted for the implementation of fiber-fed 60-GHz wireless systems.

(a) Fiber-fed super-heterodyne system

Central Station — Electric-to-optic Conversion — Data (IF) — E/O — Optical Fiber — PD — mixer — PA — PLO — Antenna — 60 GHz — Antenna — LNA — mixer — PLO — Data (IF) — Base station — Mobile Terminal

Phase-locking is NOT required!   RF + LO signals transmission   PLO is NOT required!

(b) Fiber-fed Self-heterodyne system

Central Station — Electric-to-optic Conversion — Data (IF) — E/O — Optical Fiber — PD — mixer — PA — LO — Antenna — 60 GHz — Antenna — LNA — square-law detector — Data (IF) — Base station — Mobile Terminal

Fig. 5-1. Downlink configurations of remote up-conversion systems: (a) a conventional fiber-fed 60-GHz super-heterodyne systems and (b) a fiber-fed 60-GHz self-heterodyne systems.

5-2. Optoelectronic mixer

5-2-1. System configuration using a 60-GHz harmonic optoelectronic mixer based on the CMOS-APD

To simplify base station architecture for remote up-conversion systems, a harmonic optoelectronic mixer is implemented using the CMOS-APD. Because optoelectronic mixers can simultaneously perform photodetection and frequency conversion, an additional electrical mixer is not required, thus complexity of base stations can be reduced.

For realizing optoelectronic mixers, several approaches have been reported. InP-based phototransistors including high electron-mobility transistors (HEMTs) and heterojunction phototransistors (HPTs) are investigated because they can simultaneously provide photodetection, amplification, and frequency mixing [27], [28]. Although these approaches can significantly simplify the base station architecture, InP-based components are, as of yet, not very cost-effective. Nonlinearity of semiconductor photodetectors has been also used for photodetection and frequency mixing. Frequency up- or down- conversion using GaAs metal-semiconductor-metal photodetectors (MSM-PDs) [37], InGaAs p-i-n photodiodes [38] or Si avalanche photodetectors (APDs) has been

reported [39], [40]. However, the optoelectronic mixers based on these photodetectors require output signal amplification to compensate conversion loss and it is not an easy task to integrate these photodetectors with necessary electronic circuits in a cost-effective manner.

The CMOS-APD is a very promising solution to overcome these problems. As discussed earlier, CMOS technology is widespread and mature, and possesses great potential for cost reduction. In addition, it provides a powerful platform in which many necessary circuits can be easily integrated.

Fig. 5-2 shows the downlink architecture of fiber-fed 60-GHz self-heterodyne wireless systems using a CMOS-compatible harmonic optoelectronic mixer (CMOS-HOEM) based on the CMOS-APD. Due to multi-functionality of photodetection and frequency conversion, the base station is simplified without an electrical mixer. In addition, required LO frequency is reduced by half due to the operation of harmonic frequency conversion.
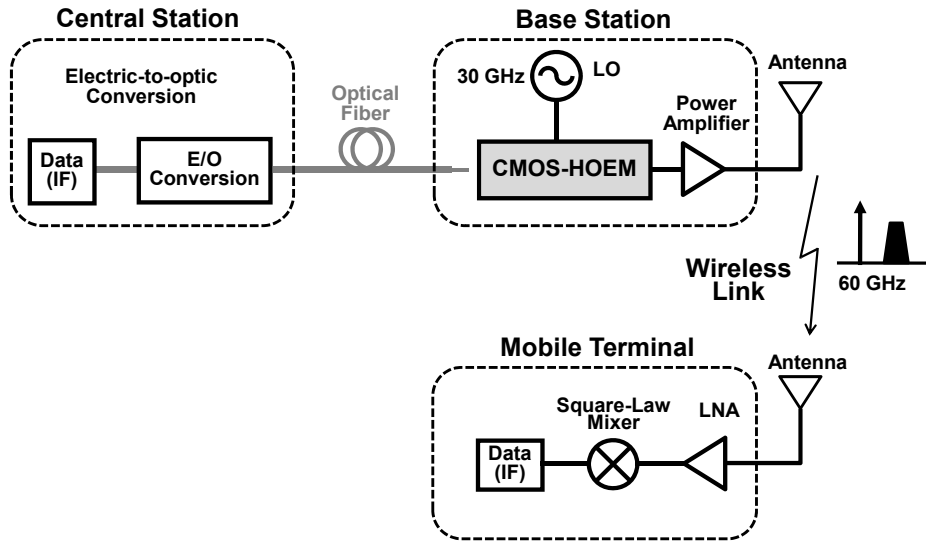
Fig. 5-2. The downlink configuration of fiber-fed 60-GHz self-heterodyne wireless systems using a CMOS-compatible harmonic optoelectronic mixer (CMOS-HOEM) based on the CMOS-APD.

5-2-2. Operation principle and characteristics of the CMOS-compatible harmonic optoelectronic mixer (CMOS-HOEM) using the CMOS-APD

Harmonic frequency up-conversion using the CMOS-HOEM is implemented in the manner shown in Fig. 5-3. An electrical LO signal is injected to the N-Well port of the P+/N-Well junction CMOS-APD and an optically modulated IF signal is illuminated to the device. Output signals of frequency up-converted components are extracted from the P+ port.

In the CMOS-HOEM, frequency mixing can be possible owing to nonlinear characteristics of avalanche multiplication factor which is shown in Fig. 3-3. As a result, the CMOS-HOEM can simultaneously perform photodetection and frequency conversion. Fig. 5-3 also shows spectrum of frequency up-converted signals when electrical LO frequency and optical IF is 30 GHz and 100 MHz, respectively. In the spectrum, second harmonic LO at 60 GHz ($2 \cdot f_{LO}$), upper side band (USB) at 60.1 GHz ($2 \cdot f_{LO} + f_{IF}$) and lower side band (LSB) at 59.9 GHz ($2 \cdot f_{LO} - f_{IF}$) are clearly observed.
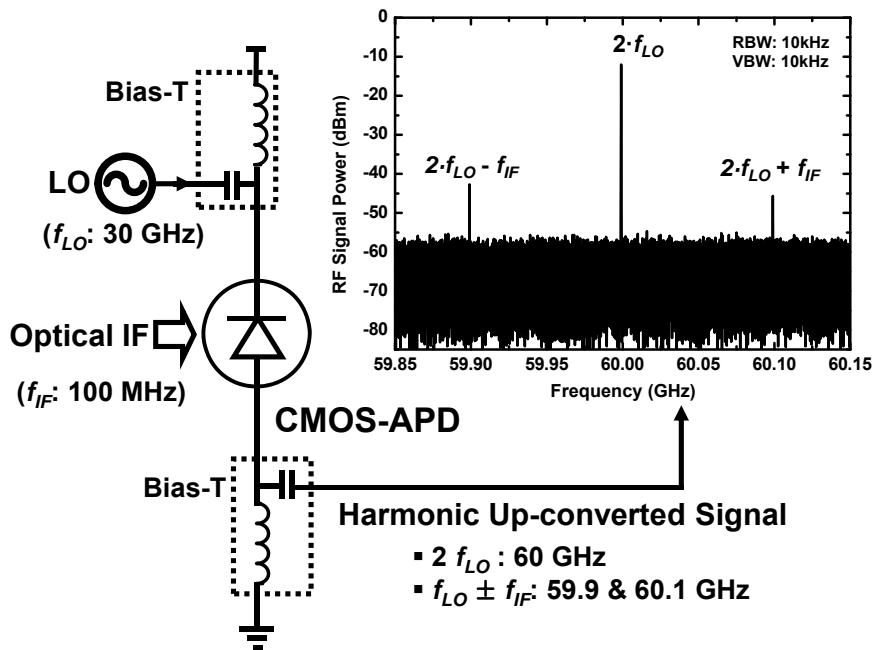
Fig. 5-3. Schematic diagram of harmonic optoelectronic mixing utilizing the CMOS-APD and the spectrum of frequency up-converted signals when 30 GHz electrical LO and 100 MHz optical IF signals are applied to the device.

To optimize the CMOS-HOEM, the dependence of frequency up-converted signal powers for USB and LSB on the reverse bias voltage (V_R) is investigated and the results are shown in Fig. 5-4. For the comparison, the photodetected IF signal powers as a function of the reverse bias voltage is also shown. In the experiment, electrical LO signal power and optical IF signal power into the CMOS-HOEM are 20 dBm and 0 dBm, respectively. With increasing V_R, frequency up-converted signal powers increases and have maximum value at V_R of 10.1 V. This is because at this voltage CMOS-HOEM has maximum avalanche multiplication factor, therefore, maximum photodetected IF signal power. Due to performance variation of devices on the same wafer, the CMOS-HOEM used in our experiment has slightly lower maximum avalanche-gain voltage of 10.1 V than that of the CMOS-APD presented in Chapter 3.

Fig. 5-5 shows the dependence of frequency up-converted signal and second harmonic LO signal powers on injected 30-GHz electrical LO signal power. It is seen that the frequency up-converted signal power and LO signal power increases with slope of 3 and slope of 2, respectively, as LO signal power increases. This dependence is due to second order and third-order mixings for second harmonic LO ($2 \cdot f_{LO}$) and frequency up-converted signals ($2 \cdot f_{LO} + f_{IF}$ and $2 \cdot f_{LO} - f_{IF}$),

respectively. When LO power is about 21 dBm, frequency up-converted signals do not increase with increasing LO power owing to the saturation of the CMOS-HOEM.
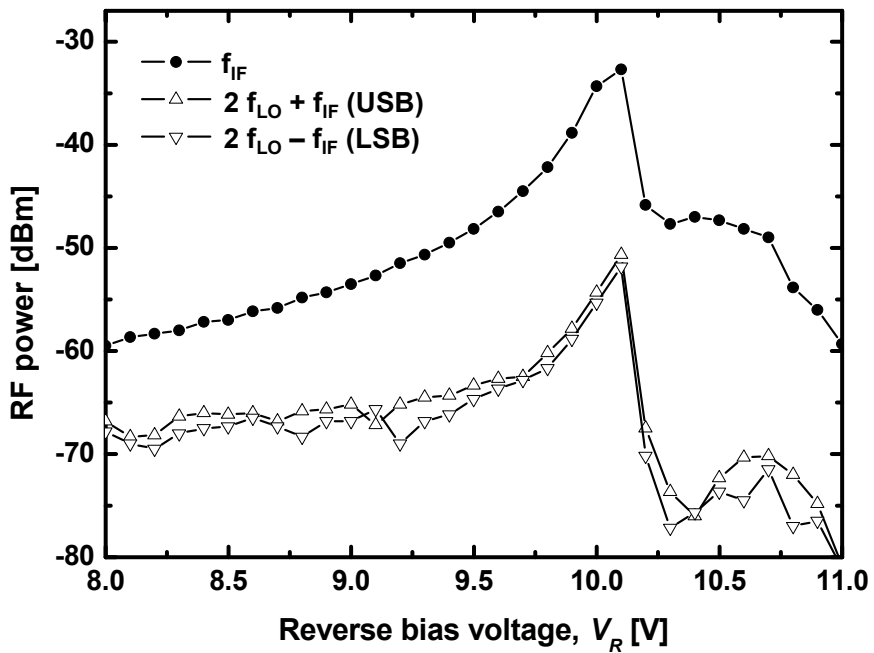
Fig. 5-4. Frequency up-converted signal powers (USB at 60.1 GHz and LSB at 59.9 GHz) as well as photodetected IF signal powers at 100 MHz as functions of the reverse bias voltage applied to the CMOS-HOEM.
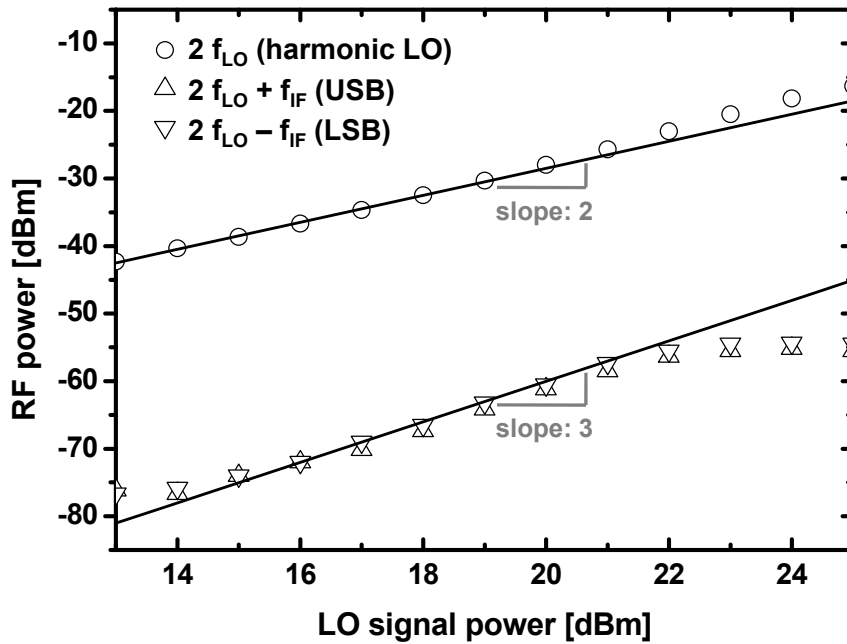
Fig. 5-5. Frequency up-converted signal powers (USB and LSB) and second harmonic LO signal powers as functions of electrical LO signal power injected to the CMOS-HOEM.

5-2-3. Experimental setup for downlink data transmission

Utilizing the CMOS-HOEM, downlink data transmission through the fiber-fed 60-GHz self-heterodyne wireless system is demonstrated. The experimental configuration is shown in Fig. 5-6. At the central station, optical modulation was performed using an 850-nm laser diode and an electro-optic modulator. A 25-Mbps 32-QAM data at IF of 100 MHz were generated using a vector signal generator (Agilent E4432B) and injected to the electro-optic modulator. The optically modulated signal was transmitted via 3-m long multimode fiber and illuminated to the CMOS-HOEM through a lensed fiber. Using the CMOS-HOEM, data embedded in optical signal are photodetected and harmonic frequency up-converted to 60-GHz band at the base station. For harmonic optoelectronic mixing, 30-GHz LO signal from a signal generator (Anritsu 68177C) is amplified by 30-GHz band power amplifier (Quinstar QPN-3004526-JO), and then applied to the CMOS-HOEM. At the mobile terminal, received data together with LO signal at 60-GHz band are boosted by a 36.5-dB gain low-noise amplifier (LNA) and frequency down-converted to IF band by a Schottky diode envelope detector. To evaluate link performance, the data at IF are demodulated by a vector signal analyzer (Agilent 89441A).

In the experiment, 60-GHz wireless link is omitted by connecting

base station and the mobile terminal with a cable. The reverse bias voltage of 10.1 V was applied to the CMOS-HOEM for maximum frequency up-converted power and injected electrical LO power was about 20 dBm. The incident optical power is about 0 dBm.
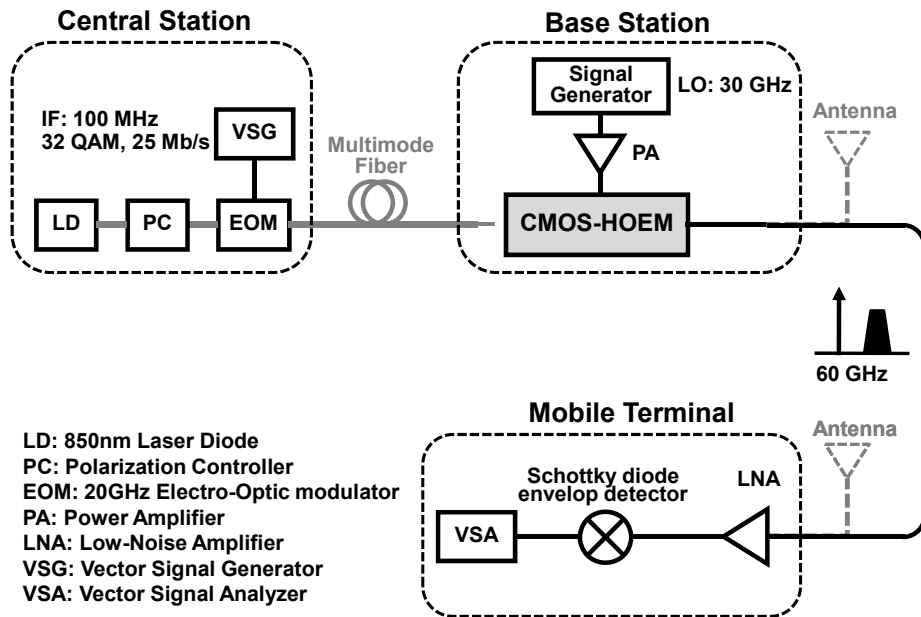
Fig. 5-6. Experimental setup for downlink data transmission through the fiber-fed 60-GHz self-heterodyne system using the CMOS-compatible harmonic optoelectronic mixer (CMOS-HOEM).

5-2-4. Demonstration of data transmission through the fiber-fed 60-GHz self-heterodyne system using the CMOS-HOEM

25-Mbps 32-QAM data were successfully transmitted through the fiber-fed 60-GHz self-heterodyne system. Fig. 5-7 shows experimental results at the mobile terminal. By self-mixing of transmitted RF and LO signals, data at 60-GHz band are frequency down-converted to IF band of 100 MHz and the spectrum is shown in Fig. 5-7 (a). Using the vector signal analyzer for demodulation of data, constellation and eye diagram were measured as shown in Fig. 5-7 (b). From the measurements, rms error vector magnitude (EVM) of 5.1 % corresponding to about 21.7 dB signal-to-noise (SNR) ratio was obtained.
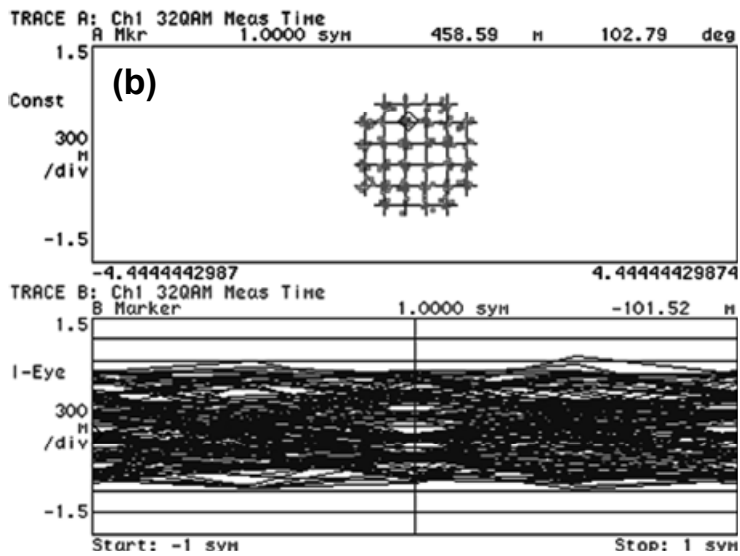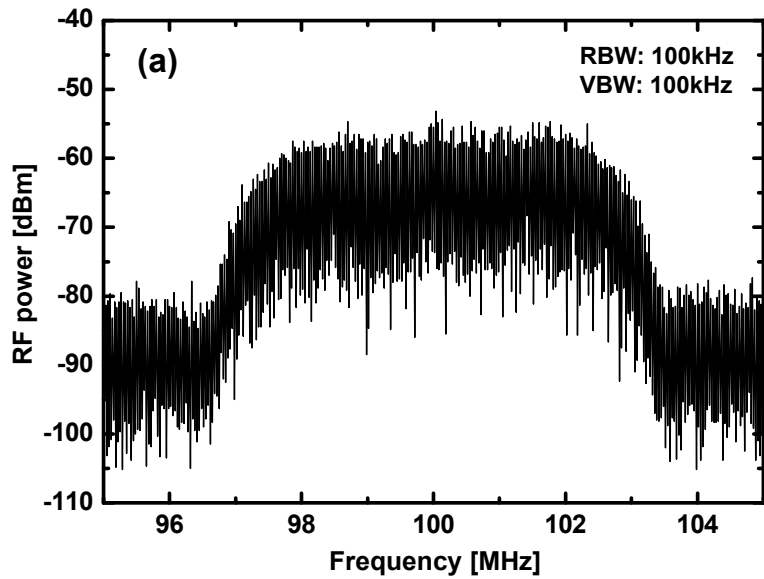
Fig. 5-7. (a) Frequency down-converted signal spectrum at the output of Schottky diode envelop detector. (b) Constellation and eye diagram of demodulated 25-Mbps 32-QAM data at the vector signal analyzer.

5-3. Self-oscillating optoelectronic mixer

5-3-1. System configuration using a 60-GHz self-oscillating harmonic optoelectronic mixer based on the CMOS-APD

For further simplification of base station architecture, a 60-GHz self-oscillating harmonic optoelectronic mixer is implemented utilizing the CMOS-APD. The CMOS-compatible self-oscillating harmonic optoelectronic mixer (CMOS-SOHOM) can simultaneously perform photodetection, signal generation, and frequency up-conversion. Fig. 5-8 shows downlink configuration of the fiber-fed 60-GHz self-heterodyne wireless system using the CMOS-SOHOM. It is seen that a photodetector, a local oscillator, and a mixer are combined into the CMOS-SOHOM, thus base station is simplified.

As for the implementation of the CMOS-HOEM, CMOS technology is also promising solution for the CMOS-SOHOM because all the required components can be realized on a single chip. Although fully integrated solution is eventually pursued, initial results for the self-oscillating harmonic optoelectronic mixer with hybrid approach are demonstrated in this dissertation.
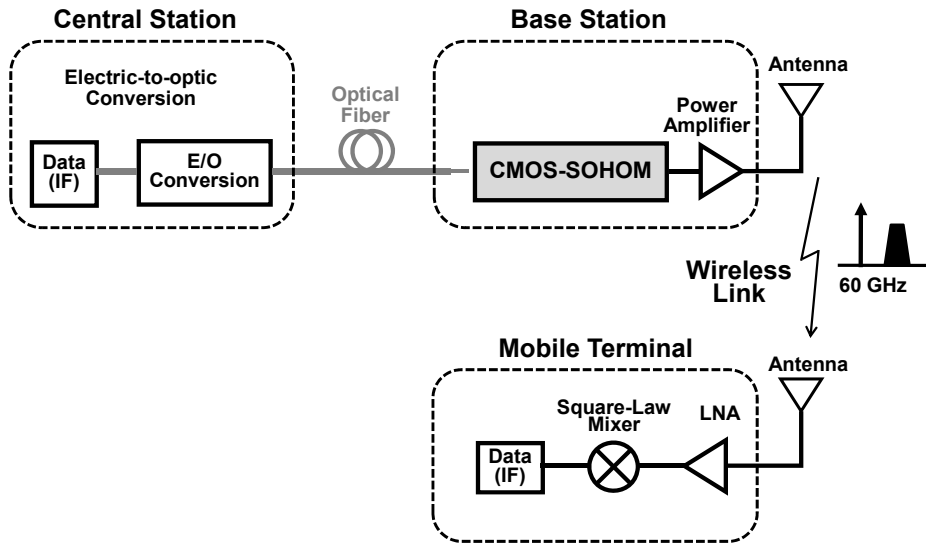
Fig. 5-8. Downlink configuration of the fiber-fed 60-GHz self-heterodyne wireless system using the CMOS-compatible self-oscillating harmonic optoelectronic mixer (CMOS-SOHOM) based on the CMOS-APD

5-3-2. Configuration and characteristics of the CMOS-compatible self-oscillating harmonic optoelectronic mixer (CMOS-SOHOM)

To implement the CMOS-compatible self-oscillating harmonic optoelectronic mixer (CMOS-SOHOM), the CMOS-APD for photodetection and harmonic frequency conversion is utilized and a feedback loop for signal generation is realized with discrete RF components. Schematic configuration for the CMOS-SOHOM is shown in Fig. 5-9 (a). For LO signal generation at 30-GHz band, a feedback loop using a 31-GHz bandpass filter (BPF) and 30-GHz band amplifiers are used. In the loop, the CMOS-APD acts as a capacitor which is attributed to P+/N-Well junction. To satisfy oscillation condition in which loop gain is larger than loss, a power amplifier having 37-dB gain is used to compensate the total loop loss of about 22 dB including on-wafer RF probes, RF adaptors, cables, Bias-Ts, and the CMOS-APD. Output signals of the CMOS-SOHOM are extracted by using a broadband 3-dB coupler.

Fig. 5-9 (b) shows output spectrum of generated second harmonic LO signal at 60-GHz band. Due to free-running oscillation, generated signal is unstable due to environment condition and has large phase noise. However, this poor performance of LO signal is not problematic in the self-heterodyne system as mentioned above.

(a)

Bias-T

3 dB Coupler

Output
- $2\,f_{LO}$
- $f_{LO} \pm f_{IF}$

p+ port

Optical IF

CMOS-APD

n-well port

BPF
CF: 31 GHz
BW: 620 MHz

Bias-T

Amp.
37 dB gain at 30 GHz

(b)

2nd harmonic LO

RBW: 10 kHz
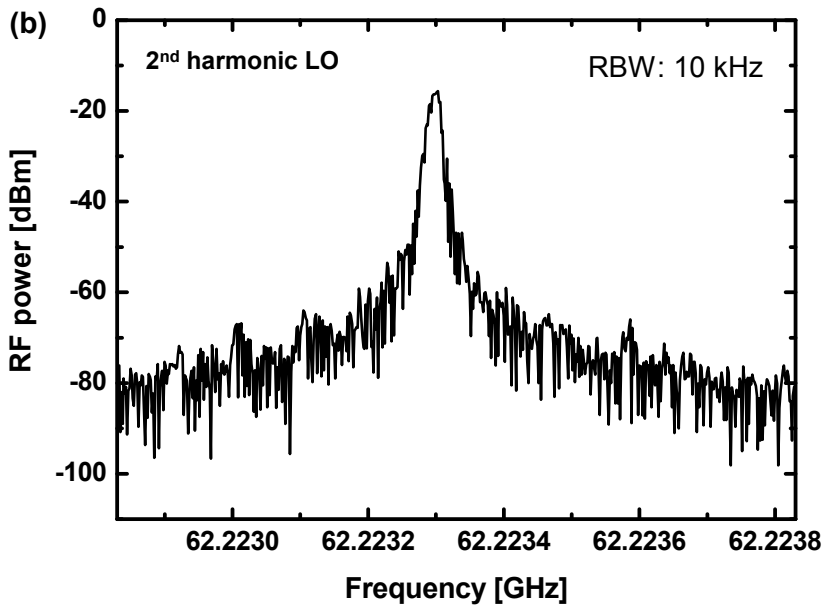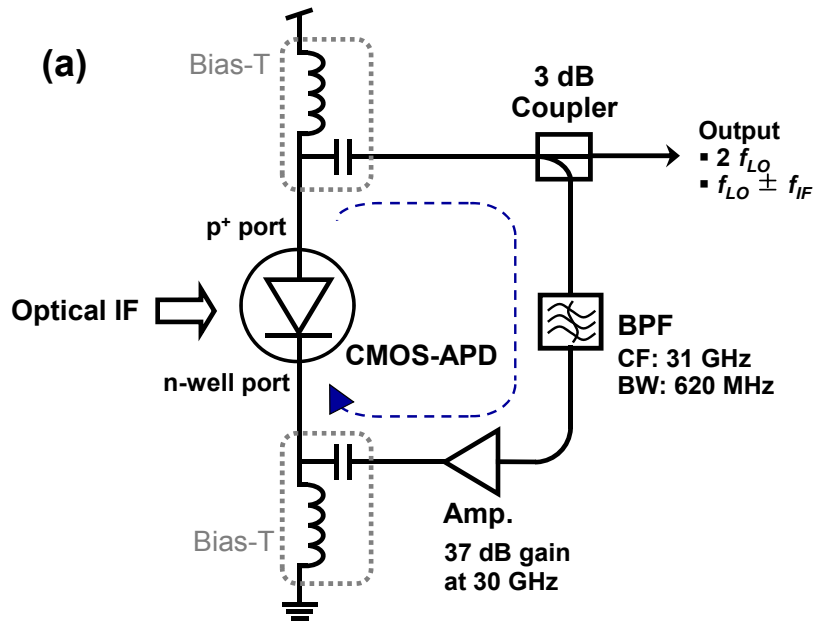
Fig. 5-9. (a) Schematic diagram of the CMOS-SOHOM having the CMOS-APD and the 30-GHz feedback loop. (b) Spectrum of second harmonic self-oscillating signal of the CMOS-SOHOM.

When the optical IF signal is illuminated to the CMOS-SOHOM, photodetection and frequency up-conversion with self-oscillating signals are performed with the help of nonlinearity of the CMOS-APD. Fig. 5-10 shows spectrum of the output signals generated by the CMOS-SOHOM under illumination of 950-MHz, 1-dBm optical IF signal. Second harmonic LO ($2 \cdot f_{LO}$), upper side band (USB at $2 \cdot f_{LO} + f_{IF}$), and lower side band (LSB at $2 \cdot f_{LO} - f_{IF}$) are clearly observed as in the CMOS-HOEM output spectrum.
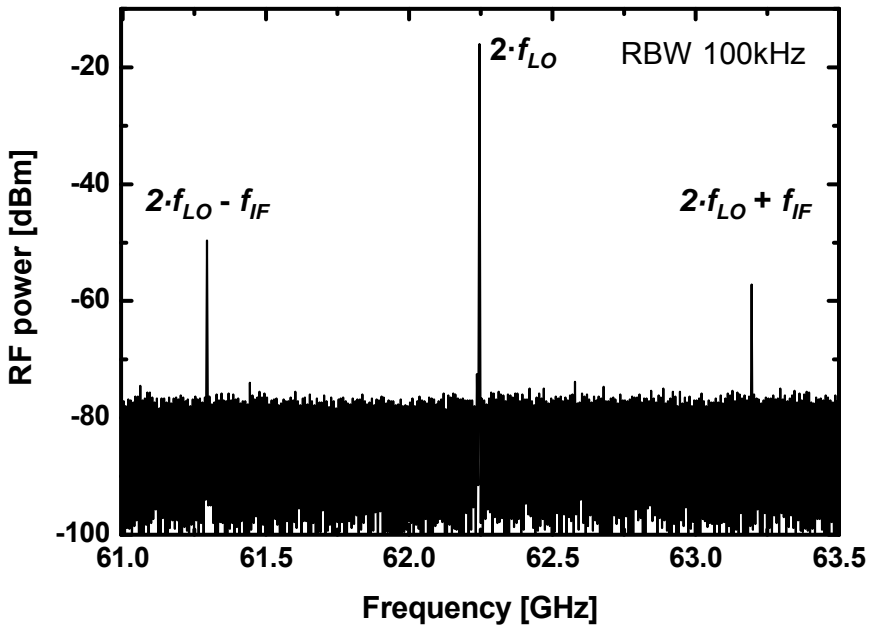
Fig. 5-10. Output spectrum of the CMOS-SOHOM when 950 MHz optical IF signal is injected to the device.

To investigate the photodetection performance of the CMOS-SOHOM, photodetected IF signal powers as functions of the reverse bias voltage were measured with and without self-oscillation, and the result is shown in Fig. 5-11. By turning on or off the 30-GHz RF amplifier in the feedback loop, the self-oscillating signal was enabled or disabled, respectively. The optical IF of 950 MHz signal is illuminated to the device with optical power of 1 dBm. When the self-oscillating signal is injected to the CMOS-APD, the bias voltage for maximum photodetected signal power due to enhanced avalanche multiplication is shifted to the higher reverse voltage of 10.3 V. This is due to additionally generated DC components by mixing process. Owing to second order nonlinearity of the CMOS-APD, DC components as well as harmonic LO signals are generated by injection of self-oscillating LO signal to the device. Consequently, to maintain the condition for maximum photodetected IF signal power, the reverse bias voltage should be changed in the CMOS-SOHOM.

Fig. 5-12 shows the dependence of frequency up-converted signal power at 60-GHz band on the reverse bias voltage. For the comparison, photodetected IF signal powers of the CMOS-SOHOM are also shown in Fig. 5-12. As in the CMOS-HOEM, the maximum frequency up-converted signal power is obtained at the bias condition in which

photodetected IF signal is maximized due to enhance avalanche multiplication factor. However, there is some discrepancy between the dependence of frequency up-converted and photodetected IF signal powers on the reverse bias voltage because mixing process is affected not only by photodetection of IF signal but also by nonlinear coefficient of the CMOS-SOHOM.
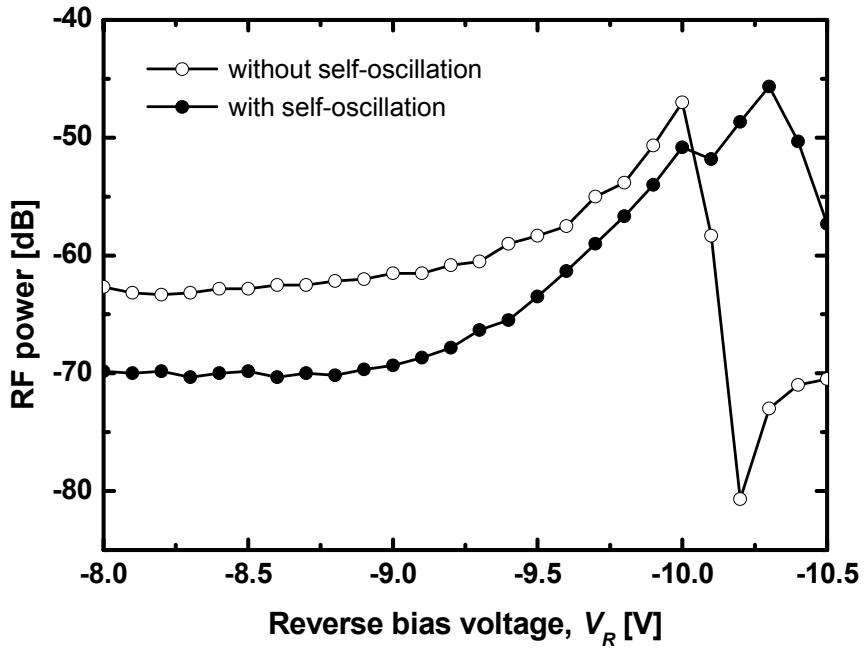
Fig. 5-11. Photodetected IF signal powers at 950 MHz as functions of the reverse bias voltage with and without self-oscillation by turning on/off the amplifier in the feedback loop.
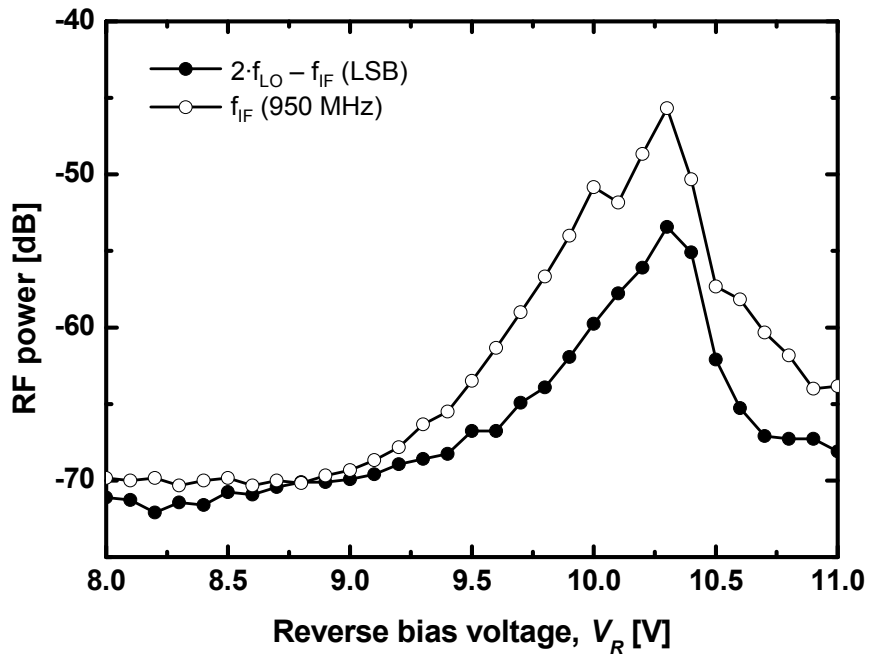
Fig. 5-12. Frequency up-converted signal power (LSB at $2 \cdot f_{LO} - f_{IF}$) and photodetected IF signal power (f_{IF}) as functions of the reverse bias voltage of the CMOS-SOHOM.

5-3-3. Experimental setup for downlink data transmission

Using the CMOS-SOHOM, the fiber-fed 60-GHz self-heterodyne wireless system is implemented and data transmission through the system is demonstrated. Experimental configuration for 25-Mbps 32-QAM data transmission is shown in Fig. 5-13. At the central station, data at 950 MHz IF are optically modulated and transmitted to the base station via 3-m long multimode fiber. The CMOS-SOHOM performs photodetection and frequency up-conversion to 60-GHz band with internally generated 30-GHz LO signal at the base station. To compensate wireless link loss, a 24-dB gain power amplifier was used at the output of the CMOS-SOHOM. Using antennas having 24 dBi gains, the frequency up-converted signals together with the second harmonic LO signal were transmitted wirelessly from the base station to the mobile terminal. The wireless link distance was about 1 m.

In the experiment, incident optical power into the CMOS-SOHOM was controlled by an optical attenuator to characterize the performance. The reverse bias voltage of 10.3 V was applied to the CMOS-SOHOM because this provide maximum photodetected IF signal power, thus maximum frequency up-converted signal power. At the mobile terminal, frequency down-converted data at 950 MHz are demodulated by a vector signal analyzer (Agilent 89441A) to evaluate overall system

performance.
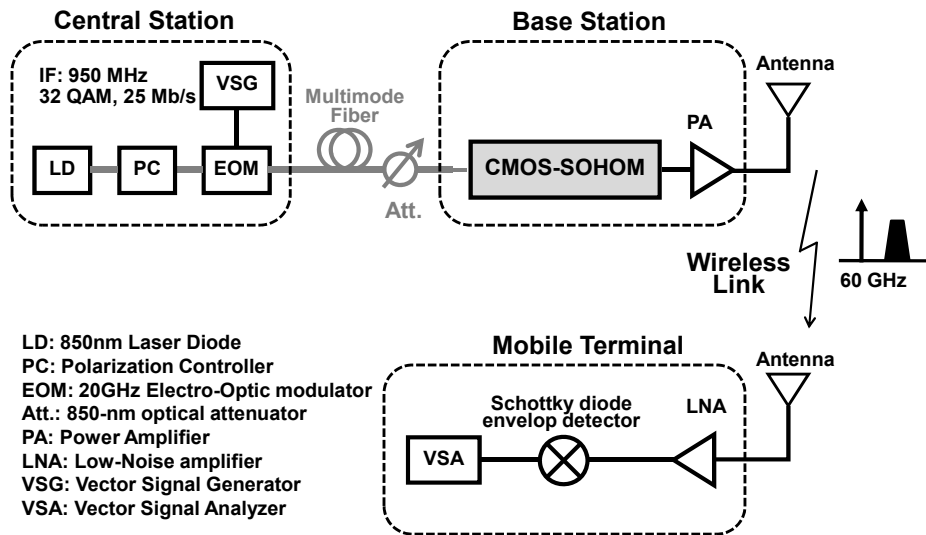
Fig. 5-13. Experimental setup for downlink data transmission through the fiber-fed 60-GHz self-heterodyne wireless system based on the CMOS-compatible self-oscillating harmonic optoelectronic mixer (CMOS-SOHOM).

5-3-4. Demonstration of data transmission through the 60-GHz self-heterodyne wireless system using the CMOS-SOHOM

25-Mbps 32-QAM data were successfully transmitted through downlink of the fiber-fed 60-GHz self-heterodyne wireless system utilizing the CMOS-SOHOM having the CMOS-APD and the feedback loop. Fig. 5-14 shows frequency down-converted data to IF of 950 MHz by self-mixing of received data and LO signals at the mobile terminal. The incident optical power into the CMOS-SOHOM was about 1 dBm and the reverse bias voltage of 10.3 V was applied to the device. These down-converted data at IF are demodulated by the vector signal analyzer and constellation as well as eye diagram results are shown in Fig. 5-15. The measured rms error vector magnitude (EVM) was about 1.83 %, which corresponds to 30.7-dB signal-to-noise ratio (SNR). This EVM of the fiber-fed 60-GHz self-heterodyne system should be sufficient for many wireless applications.

To estimate the supported optical link distance between the central station and the base station, rms EVM as well as SNR performances as a function of optical power is measured and the result is shown in Fig. 5-16. With increasing incident optical power, SNR increases and EVM decreases. This is simply due to increased output signal power when high optical power is injected to the CMOS-SOHOM. With a

87

sufficiently high optical power source, the distance between the central station and the base station can be expected to reach a few hundred meters because typical multimode fiber has attenuation loss less than 3 dB/km.

From the experimental results, feasibility of the use of the CMOS-SOHOM in the fiber-fed 60-GHz self-heterodyne wireless system is demonstrated. In spite of low-quality LO signal generated in the CMOS-SOHOM, data transmission is successfully performed with the virtue of the self-heterodyne system which is immune to phase noise and frequency offset problems. By utilizing the CMOS-SOHOM, it is expected that base station architecture is simplified, thus cost-effective realization can be possible.
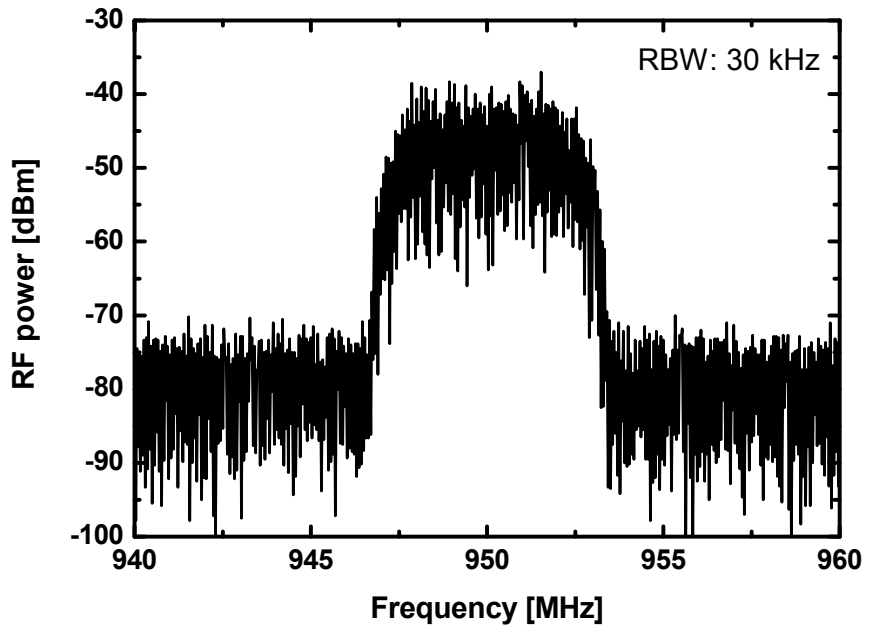
Fig. 5-14. Spectrum of frequency down-converted 25-Mbps 32-QAM data to IF band at the mobile terminal.

TRACE A: Ch1 32QAM Meas Time
A Mkr   1.0000 sym   804.68   m   -32.344 deg

(a)

Const

300 M/div

TRACE C: Ch1 32QAM Meas Time
C Marker   1.0000 sym   690.16   m

(b)

I-Eye

300 M/div

Start: -1 sym   Stop: 1 sym
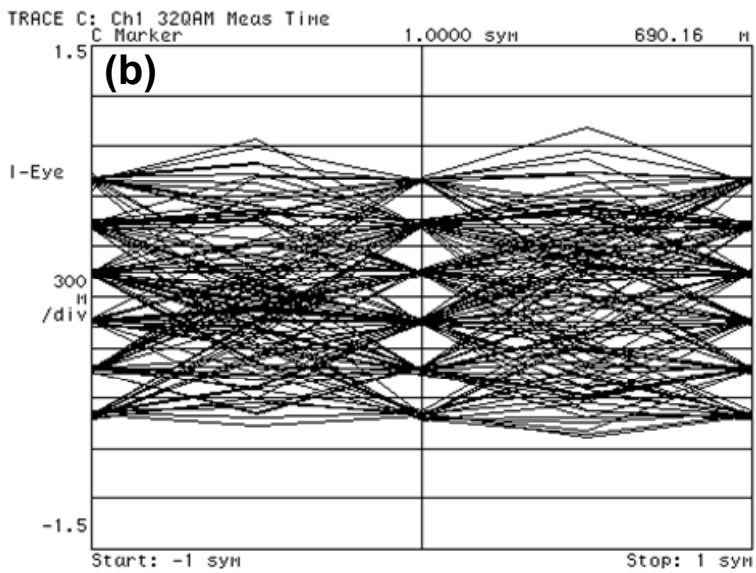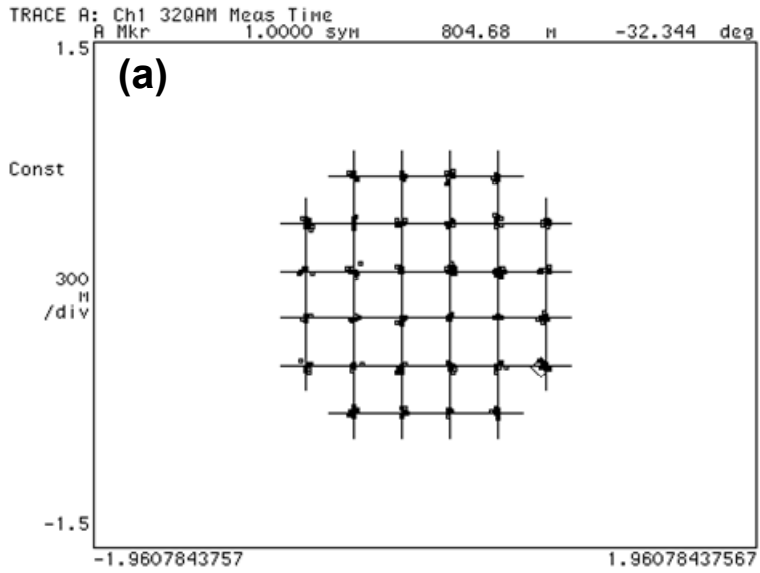
Fig. 5-15. (a) Constellation and (b) eye diagram of demodulated data at the vector signal analyzer.
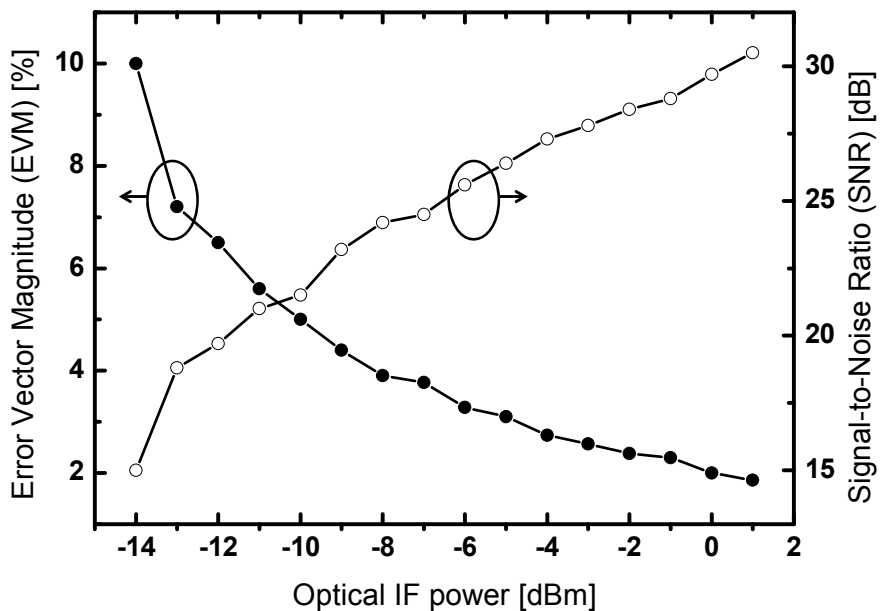
Fig. 5-16. RMS error vector magnitude (EVM) and signal-to-noise ratio (SNR) measured at the output of Schottky diode envelop detector in the mobile terminal as a function of incident optical power into the CMOS-SOHOM at the base station.

6. Implementation of low-cost Radio-over-Fiber systems using CMOS-APDs

6-1. Introduction

With rapidly growing data bandwidth and carrier frequency of wireless communication systems including cellular services and wireless local area network (WLAN), radio-over-fiber (RoF) systems have been regarded as a promising candidate for radio signal distribution to base stations or access points [41-47]. Due to such advantages of optical fiber as huge bandwidth and low transmission loss, high-capacity data embedded on radio frequency (RF) can be easily distributed, thus coverage extended. Fig. 6-1 shows schematic diagram of RoF systems for WLAN and/or cellular services. To realize wide deployment of these systems to densely populated area or shadow regions such as airport lounges, school campuses, shopping malls, and subway stations, low-cost implementation is essential. Particularly, as the cell size decreases to picocell or femtocell, large numbers of base stations are needed and reducing the cost is critical.

To achieve cost reduction of RoF systems for WLAN or cellular systems, several approaches have been reported. Niiho *et al.* developed multichannel 5-GHz RoF WLAN systems using an inexpensive 2.5-

92

Gbps distributed feedback laser diode and a p-i-n diode [43]. In spite of low optic-to-electric conversion efficiency, cost reduction of RoF systems was achieved. Using this system, transmission of IEEE 802.11a WLAN data at 5-GHz band through 1.3 μm zero-dispersion single-mode fiber was demonstrated. Chia *et al*. used a vertical-cavity surface-emitting laser (VCSEL) and multimode fiber to reduce the cost of RoF links [41]. They demonstrated transmission of IEEE 802.11g and IEEE 802.11a WLAN signals at 2.4 GHz and 5 GHz, respectively. Yee *et al*. presented RoF systems using VCSELs and 300-m long multimode fiber for transmission of IEEE 802.11g WLAN signals at 2.412 GHz [47]. They also investigated the effect of interferences caused by coexisting cellular signals. Das *et al*. reported RoF systems based on VCSELs and 300-m multimode fiber with 5-m wireless link and analyzed transmission performance of IEEE 802.11b/g WLAN signals at 2.4 GHz and cellular signals [42]. However, these approaches considered cost issues of only optical sources and transmission media, and no serious attempt has been made for cost reduction of optical receivers.

For the realization of cost-effective RoF receivers, CMOS technology can be attractive solution. With well developed electronic circuits for analog, digital, and RF application, integrated optical

receiver can be implemented using CMOS-compatible photodetectors (CMOS-PDs). Fig. 6-2 shows schematic diagram of low-cost RoF downlink based on the CMOS-PD. With readily available AlGaAs/GaAs vertical cavity surface emitting lasers (VCSEL) and multimode fiber, implementation cost of the RoF system can be reduce by utilizing CMOS-PDs for RoF receivers.

In this dissertation, the feasibility of adopting CMOS-APDs for RoF receiver is demonstrated. For this, RoF transmission of WCDMA and/or WLAN signals is performed. The CMOS-APD receiver having the CMOS-APD and the transimpedance amplifier as explained in section 4-1 is used for all the experiments. With measurement of error vector magnitudes (EVMs), performances of the CMOS-APD for the RoF system are investigated.
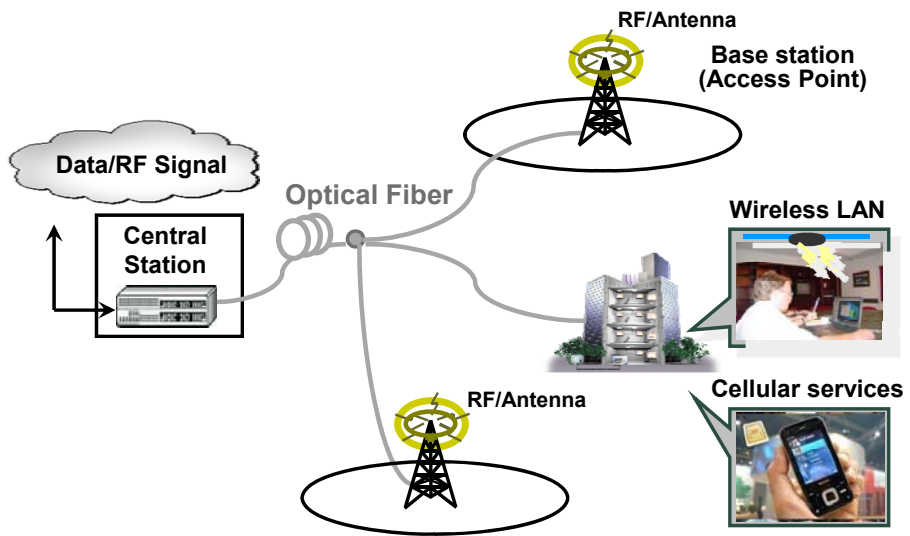
Fig. 6-1. Applications of Radio-over-Fiber (RoF) systems for cellular and/or WLAN signal distribution.
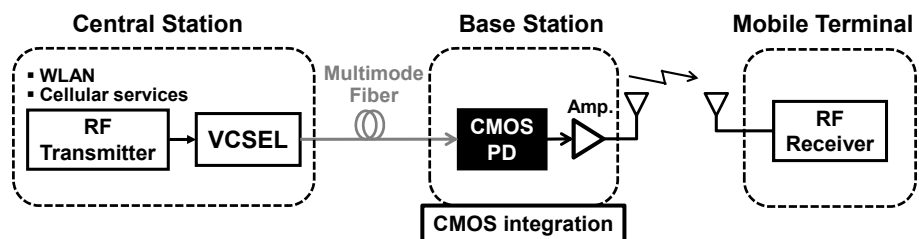
Fig. 6-2. Schematic diagram of low-cost Radio-over-Fiber downlink systems using CMOS-compatible photodetectors.

6-2. RoF transmission of cellular or WLAN signal

6-2-1. Experimental setup for RoF transmission of WCDMA or WLAN signal

Using the CMOS-APD receiver, wideband code division multiple access (WCDMA) or wireless local area network (WLAN) signal was transmitted through RoF downlinks with experimental configuration shown in Fig. 6-3. At the central station, optical modulation of 2.1-GHz WCDMA or 5.2-GHz IEEE 802.11a WLAN signal was performed with an 850-nm laser diode, an electro-optic modulator, and vector signal generators (Agilent E4432 for WCDMA, Anritsu MG3700A for WLAN). The generated optical signal was transmitted to the base station via 3-m long multimode fiber whose core size is 50 μm. An 850-nm optical attenuator was inserted between multimode fibers to control input optical power into the CMOS-APD receiver. The base station was simply configured with the CMOS-APD receiver and an 18-dB gain amplifier (New Focus 1422). At the output of the base station, the photodetected and amplified signal was radiated to free space using a 4-dBi omnidirectional antenna. After 2-m wireless link, WCDMA or WLAN signal was detected by another 4-dBi omnidirectional antenna, amplified by a 24-dB gain low-noise amplifier (Mini-Circuit ZVA-

96

183+). For demodulation of WCDMA signal, the output of the low-noise amplifier is directly connected to a vector signal analyzer (Agilent 89600). On the other hand, for demodulation of WLAN signal, frequency down-conversion was performed using 5-GHz, 7-dBm LO signal and a RF mixer (Mini-Circuits ZMX-10G). To compensate the conversion loss and satisfy the sensitivity of the vector signal analyzer, an additional 20-dB gain amplifier (Mini-Circuits ZFL-1000LN) was used. The frequency down-converted WLAN signal at 200 MHz is demodulated by the vector signal analyzer.

Prior to experiments for RoF data transmission, characteristics of the CMOS-APD receiver were investigated. Fig. 6-4 shows photodetection frequency response of the CMOS-APD receiver. From the measurement, it is observed that the 3-dB bandwidth of the CMOS-APD receiver is less than carrier frequency of IEEE 802.11a WLAN signal. To utilize the CMOS-APD receiver for 5-GHz band IEEE 802.11a WLAN signal detection, about 10-dB loss due to roll-off of frequency response is inevitable.

Central Station

WCDMA or WLAN VSG

LD PC EOM

Multimode Fiber

Att.

Base Station

CMOS-APD Receiver

Amplifier

Antenna

Wireless Link

Mobile Terminal

2.1-GHz WCDMA

VSA

LNA

Antenna

5.2-GHz 802.11a WLAN

VSA

Amplifier

Mixer

LO

LD: 850-nm Laser Diode
PC: Polarization Controller
EOM: 20-GHz electro-optic modulator
Att.: 850-nm optical attenuator
VSG: Vector Signal Generator
VSA: Vector Signal Analyzer
LNA: Low-Noise Amplifier
LO: Local Oscillator

Fig. 6-3. Experimental setup for RoF downlink data transmission of WCDMA or WLAN signal.
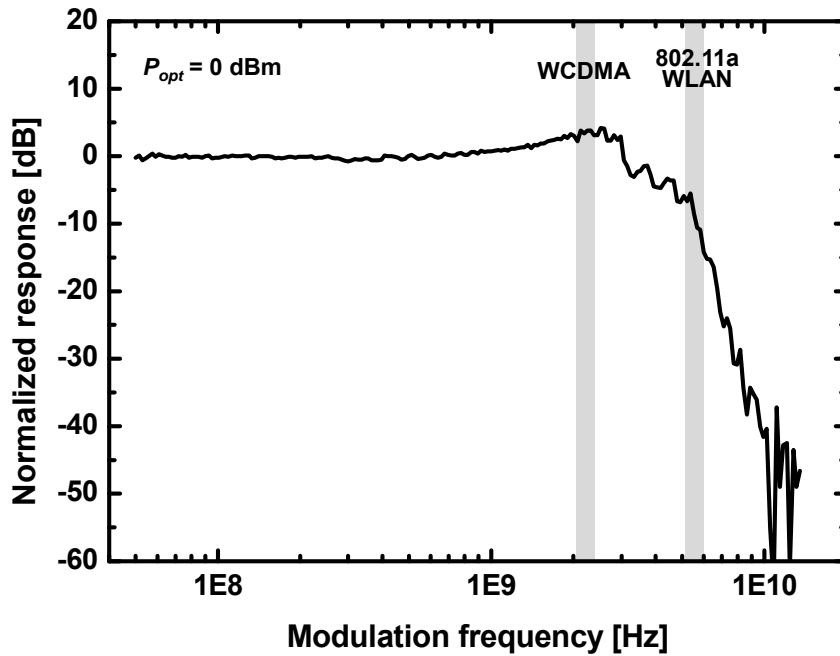
Fig. 6-4. Photodetection frequency response of the CMOS-APD receiver used in the experiments. WCDMA and IEEE 802.11a signal bands are designated.

6-2-2. RoF transmission of WCDMA signal

First of all, WCDMA signal was transmitted through RoF downlink based on the CMOS-APD receiver. Carrier frequency and chip rate of WCDMA signal is 2.1 GHz and 4.096 Mc/s, respectively. To optimize RoF system performance, dependences of rms EVMs on input RF signal power to the electro-optic modulator was measured and the result is shown in Fig. 6-5 (a). With increasing input WCDMA power, rms EVM decreases at first and has the minimum value of about 3.26 % at the input signal power of -10 dBm due to the increased optical modulation index. Beyond this condition, EVM starts to increase. The degradation of EVM is due to inter-modulation distortion caused by the nonlinearity of the electro-optic modulator.

To investigate the system performance dependent on the distance of the fiber-optic link between central station and base station, the dependence of EVM on input optical power into the CMOS-APD receiver was also measured and the result is shown in Fig. 6-5 (b). Because the 3GPP standard requires the EVM not to exceed 17.5 %, the proposed RoF downlink using the CMOS-APD receiver satisfy the EVM requirement in all the measured range of optical powers.

With the optimization of RoF downlink, WCDMA signal transmission was performed. Fig. 6-6 shows output signal spectrum of

the CMOS-APD receiver when -4 dBm WCDMA signal was injected to electro-optic modulator and -2 dBm optical signal was illuminated to the CMOS-APD receiver. It is observed that photodetected WCDMA signal has high SNR of about 30 dB. At the base station, transmitted WCDMA signal through the RoF system and wireless link was demodulated by the vector signal analyzer. Fig. 6-7 shows constellation of demodulated WCDMA signal. In the experiment, rms EVM of 3.26 % is obtained. It is believed that this EVM value is sufficient for downlink data transmission for WCDMA signal.
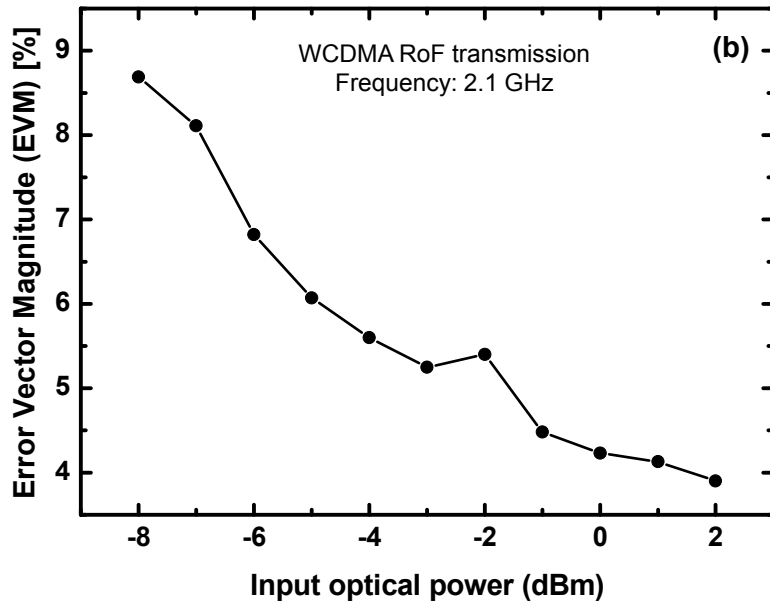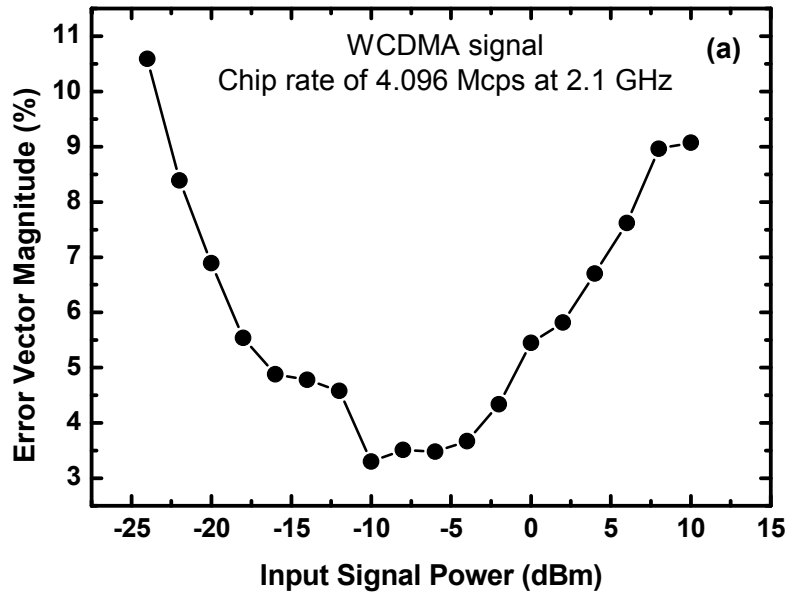
Fig. 6-5. Dependence of error vector magnitude for demodulated WCDMA signal (a) on input RF power to the electro-optic modulator and (b) on input optical power to the CMOS-APD receiver at the base station.

Fig. 6-6. Spectrum of WCDMA signal at the output of the CMOS-APD receiver in the base station.

Fig. 6-7. Constellation of demodulated WCDMA signal at the vector signal analyzer in the mobile terminal. EVM of 3.26 % is obtained.

6-2-3. RoF transmission of IEEE 802.11a WLAN signal

Through RoF downlink using the CMOS-APD receiver, IEEE 802.11a WLAN signal was transmitted. Carrier frequency and data rate was set to 5.2 GHz and 54 Mbps, which is maximum data rate supported by IEEE 802.11a, respectively. Fig. 6-8 (a) shows measured rms EVM of demodulated WLAN signal as a function of input WLAN signal power to the electro-optic modulator. The dependence of EVM on the input signal power is similar to the WCDMA case. The minimum rms EVM of 2.89 % was obtained at input WLAN power of - 4 dBm.

To estimate the supported optical link distance between central station and base station, the dependence of EVM on input optical power into the CMOS-APD receiver was also measured and the result is shown in Fig. 6-8 (b). To meet the EVM requirement of 5.6 % for IEEE 802.11a WLAN signal at 54 Mbps [48], optical power should be higher than about -4 dBm. Accordingly, it is expected that the RoF downlink using the CMOS-APD receiver can support a few hundred meters of multimode fiber link, which has attenuation loss of less than 3 dB/km typically, with sufficient optical power sources.

Fig. 6-9 shows spectrum at the CMOS-APD receiver output when - 4 dBm WLAN signal was injected to the electro-optic modulator and 2

dBm optical signal was illuminated to the device. The photodetected WLAN signal by the CMOS-APD receiver has SNR of about 25 dB. After transmission of wireless link, the WLAN signal is demodulated using the vector signal analyzer. Fig. 6-10 shows constellation of IEEE 802.11a 64-QAM OFDM WLAN signal at data rate of 54 Mbps. From the measurement, rms EVM of 2.89 % was obtained.
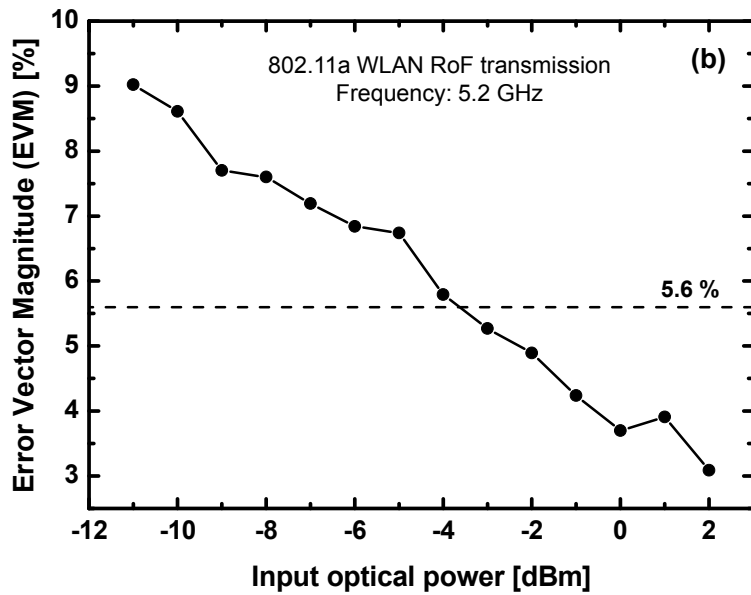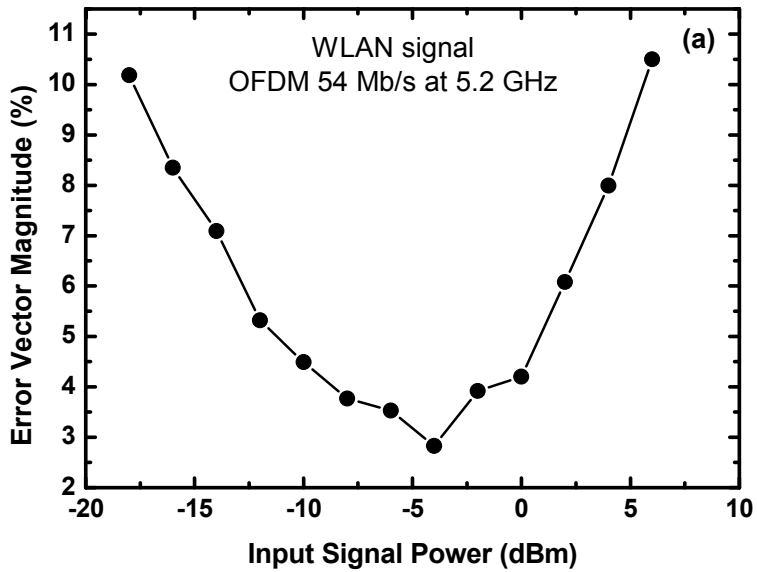
Fig. 6-8. Dependence of error vector magnitude for demodulated WLAN signal (a) on input RF power to the electro-optic modulator and (b) on input optical power to the CMOS-APD receiver at the base station.

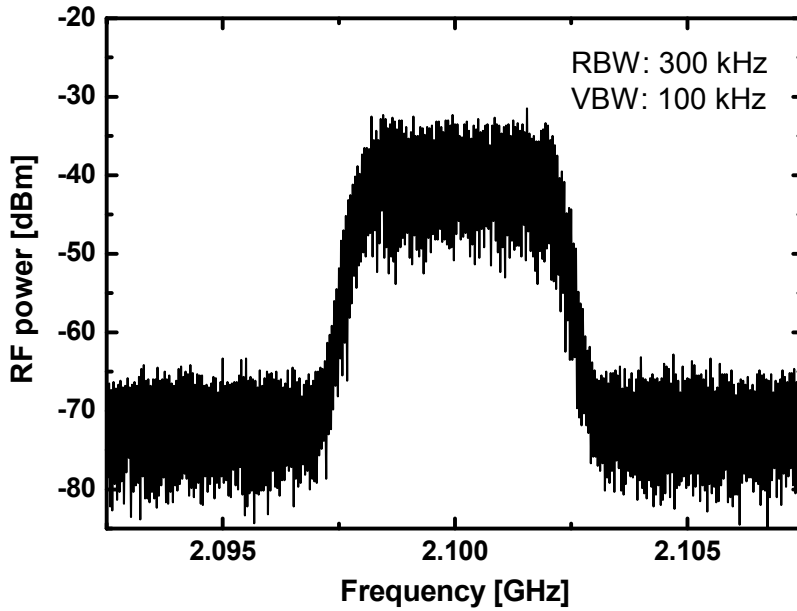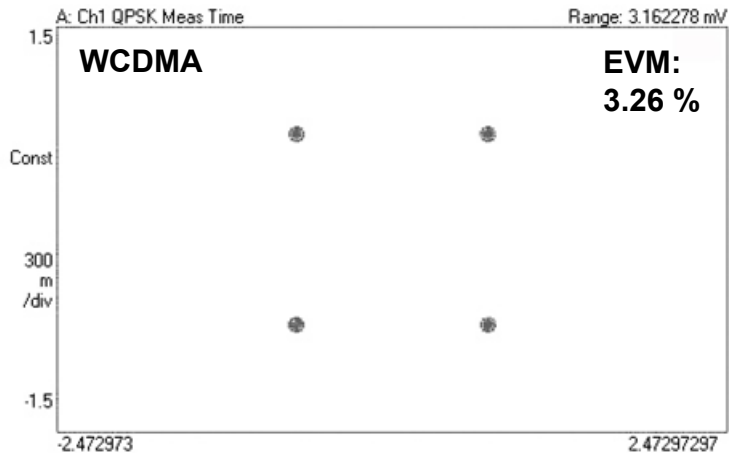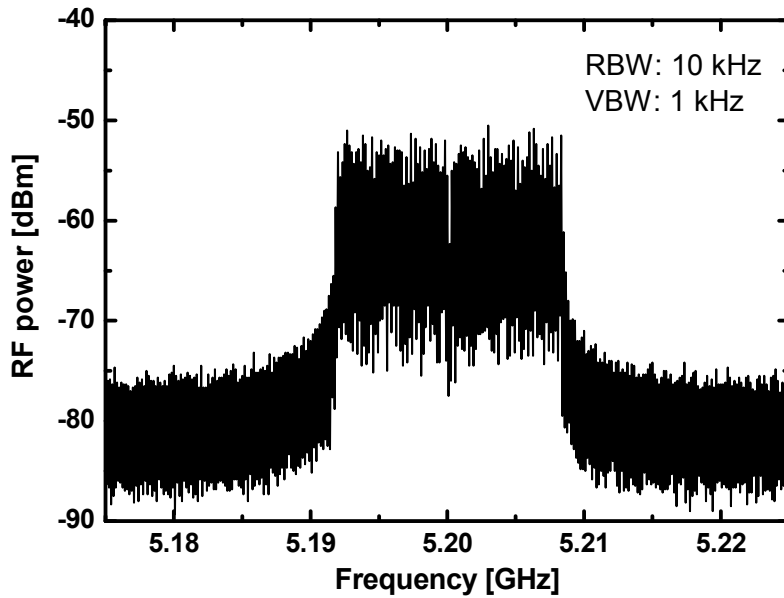Fig. 6-9. Spectrum of IEEE 802.11a WLAN signal at the output of the CMOS-APD receiver in the base station.
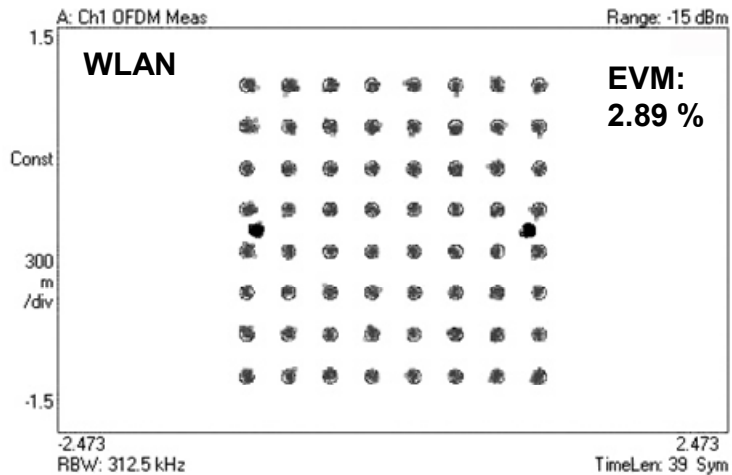
Fig. 6-10. Constellation of demodulated WLAN signal at the vector signal analyzer in the mobile terminal. EVM of 2.89 % is obtained.

6-3. Low-cost RoF downlinks for multi-standard signal transmission

6-3-1. Experimental setup for RoF transmission of both WCDMA and IEEE 802.11g WLAN signals

In order to realize cost-effective RoF systems, the CMOS-APD receiver as well as a VCSEL and multimode fiber is employed for feasibility demonstration. In addition, simultaneous RoF transmission of multi-standard service for WCDMA and IEEE 802.11g is performed.

Fig. 6-11 shows the experimental setup for downlink RoF transmission of multi-standard services. To generate optical signals, a directly modulated 850-nm VCSEL was used at the central station. The multi-standard signals, WCDMA at 2.1 GHz and WLAN at 2.4 GHz, were generated using two separate vector signal generators (Agilent E4432B, Anritsu MG3700A) and combined by a RF power combiner (Mini-Circuits ZN2PD-63+). Modulated optical signals were transmitted to the base station via 300-m long multimode fiber whose core size was 50 μm. The measured optical transmission loss of 300-m long multimode fiber was about 1.3 dB. Fig. 6-12 shows frequency response of 300-m long multimode fiber. Owing to frequency roll-off of 300-m long multimode fiber, high frequency RF signals can suffer from additional loss of RoF link. At the base station, transmitted optical

signals were injected into the CMOS-APD receiver through a lensed fiber, and after 24-dB amplification by an RF amplifier (Mini-Circuits ZVA-183+), radiated by a 4-dBi omnidirectional antenna. After 2-m wireless link, multi-standard RF signals were detected by another 4-dBi omnidirectional antenna, amplified by a 24-dB gain low-noise amplifier, and demodulated by a vector signal analyzer (Agilent 89600). In the experiment, measured signal attenuation of 2-m wireless link including antenna gains at 2-GHz band was about -40 dB. It is expected that the wireless link distance can be extended with a high-gain power amplifier to sufficiently compensate the loss.
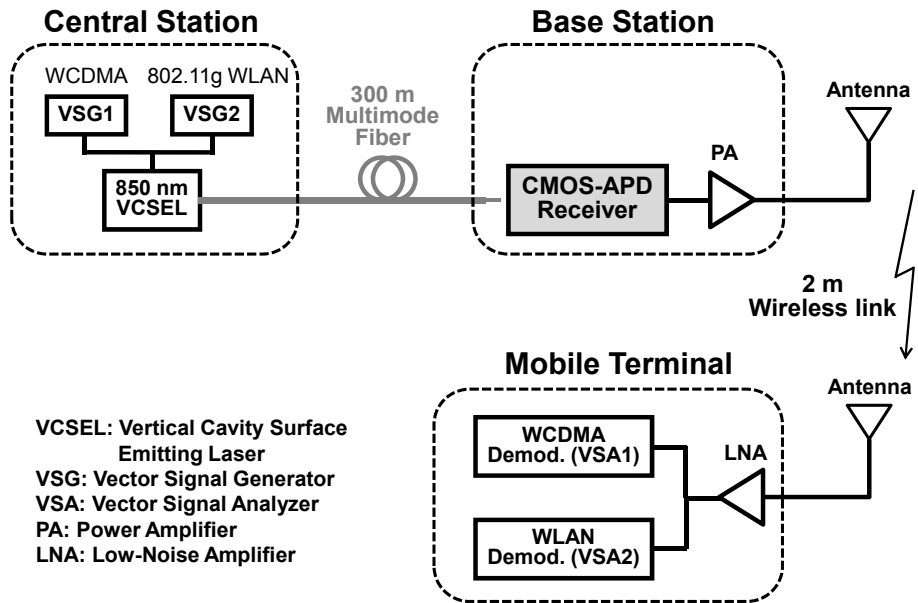
Fig. 6-11. Experimental setup for low-cost RoF downlink to transmit multi-standard signals of WCDMA and IEEE 802.11g WLAN.
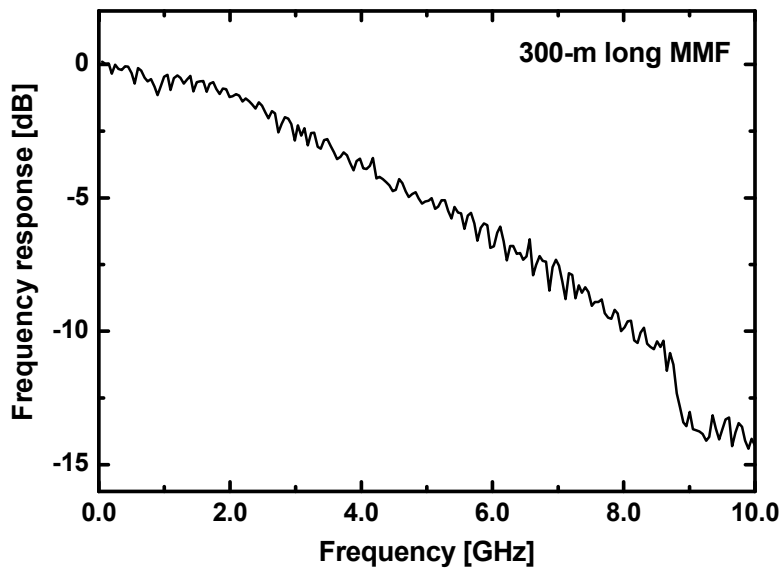
Fig. 6-12. Measured frequency response of 300-m long multimode fiber (MMF).

6-3-2. Demonstration of multi-standard signals transmission

Both 2.1-GHz WCDMA and 2.4-GHz WLAN signals were applied to the VCSEL and RoF transmitted. Fig. 6-13 shows the spectrum at the output of the amplifier in the base station. Each of WCDMA and WLAN RF signal powers was -5 dBm and the incident optical power at the lensed fiber input was about -3 dBm. The measured signal-to-noise ratio (SNR) was 44 dB for WCDMA, and 33 dB for WLAN signals as shown in Fig 6-13 (b) and (c), respectively.

For investigation of signal interference between two types of signals in the RoF downlink, the dependence of EVMs on interfering signal powers was measured and the results are shown in Fig. 6-14. The RF power of WCDMA or WLAN signals was set to -5 dBm while the interferer power was scanned. The incident optical power at the input of the lensed fiber was set to about -3 dBm.

As can be seen in the Fig. 6-14, WCDMA signal did not suffer any interference from WLAN signals, whereas WLAN suffered when WCDMA signal power became larger. This EVM degradation of WLAN signal is believed due to saturation of the CMOS-APD receiver and RF components in the base station. The IEEE 802.11g WLAN signal with larger bandwidth is more sensitive to these undesired effects. Nevertheless, the rms EVM of WLAN signal remains below the 5.6 %

requirement for data rate of 54 Mbps as specified in IEEE 802.11g standard [49].
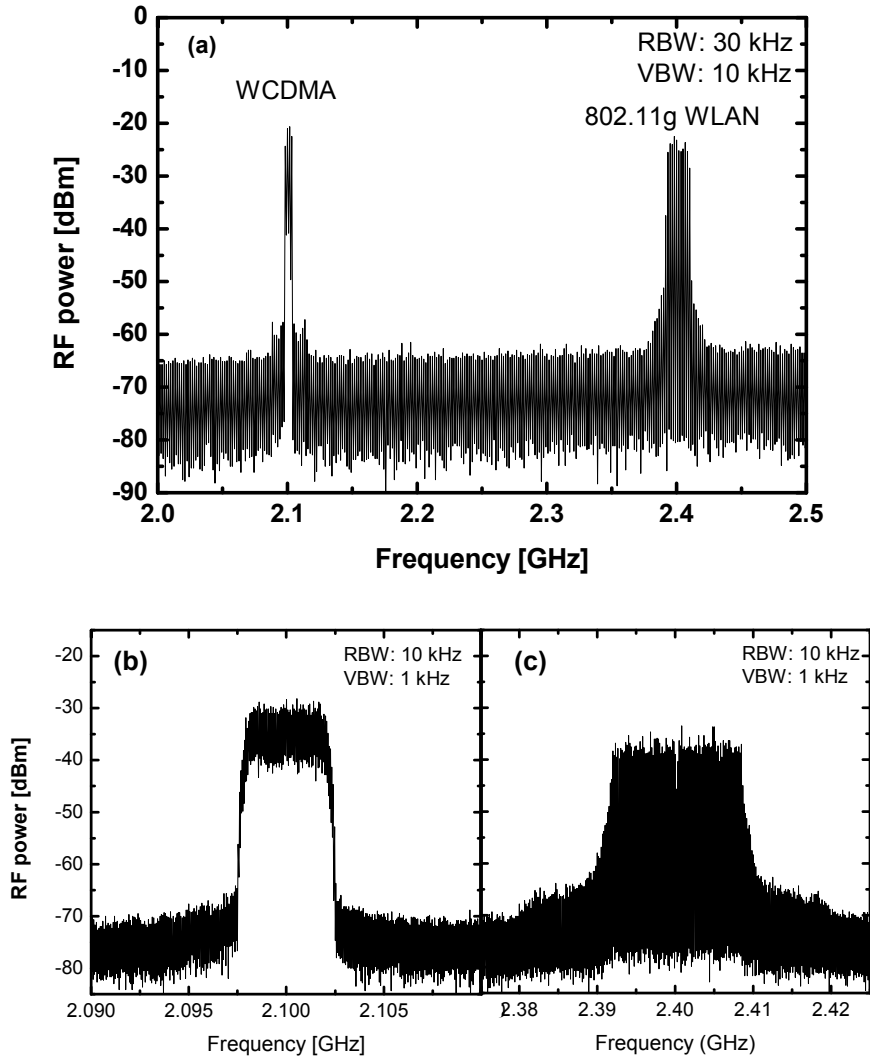
Fig. 6-13. (a) Spectrum of RoF transmitted multi-standard signals at the output of the CMOS-APD receiver. Enlarged spectrums of (b) WCDMA and (c) IEEE 802.11g WLAN signals.
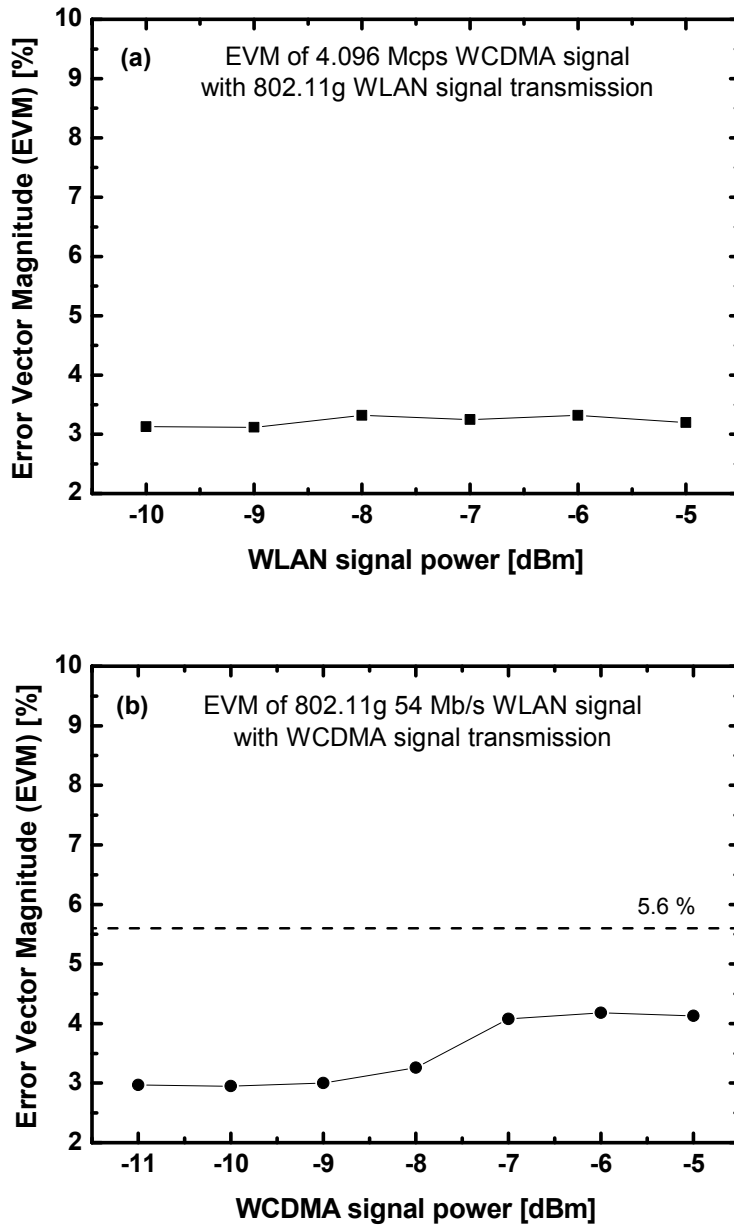
Fig. 6-14. EVM results of RoF transmission of multi-standard signals. (a) EVM of demodulated WCDMA signal as a function of WLAN signal power. (b) EVM of demodulated WLAN signal as a function of WCDMA signal power.

7. Summary

Recently, optical communication systems have evolved for short distance access networks and optical interconnects to meet the demands for high-capacity data transmission. For realization of these systems, large numbers of optical components for wide deployment of the systems is required, thus implementation cost becomes critical issue. 850-nm AlGaAs/GaAs VCSELs and multimode fiber have been developed for low-cost optical transmitters and transmission medium, however, cost-effective realization of optical receiver is still challenging. To come up with this problem, CMOS technology has been regarded as promising solution because photodetectors as well as electronic circuits can be integrated on a single chip.

In this dissertation, CMOS-compatible avalanche photodetectors (CMOS-APDs) to enable cost-effective optical receivers are investigated. Using the CMOS-APDs, Gbps wireline data transmission is performed, and utilization for fiber-fed 60-GHz self-heterodyne wireless systems and low-cost radio-over-fiber systems are demonstrated.

In chapter 2, difficulties and possible solutions for the realization of high-performance CMOS-APDs are introduced. With TCAD

simulation results, the design consideration for the CMOS-APD is explained. The structure of fabricated CMOS-APD is also described.

Chapter 3 shows characteristics of the fabricated CMOS-APD. Measured DC and photodetection frequency response characteristics are shown in this chapter. To clarify the physical origin of the rf-peaking effect in photodetection frequency response, impedance characteristics and equivalent circuit modeling is presented.

In chapter 4, 6.25-Gbps data transmission is demonstrated using the CMOS-APD receiver having the CMOS-APD and a transimpedance amplifier on a board. Experimental results for bit error rate (BER) performance and eye diagram are presented.

For realization of fiber-fed millimeter-wave wireless systems in a simple way, the self-heterodyne system is introduced in chapter 5. Utilizing CMOS-APDs for the harmonic optoelectronic mixer (CMOS-HOEM) and the self-oscillating harmonic optoelectronic mixer (CMOS-SOHOM), simplified base stations are implemented. For the feasibility demonstration, frequency up-conversion to 60-GHz band and 25-Mbps 32-QAM data transmission through the fiber-fed 60-GHz self-heterodyne wireless system are performed.

To reduce the cost of radio-over-fiber (RoF) systems, CMOS-APD receivers are used for detection of optically modulated cellular and

WLAN applications. By adopting the CMOS-APD receiver in the base station, single standard RoF transmission for 2.1-GHz WCDMA or 5.2-GHz 802.11a WLAN is performed. In addition, low-cost RoF systems having the CMOS-APD receiver, a VCSEL, and 300-m long multimode fiber are proposed and simultaneous multi-standard signal transmission for WCDMA and IEEE 802.11g are demonstrated.

From the results, it is expected that CMOS-APDs can play a central role in future optical communication systems to achieve cost reduction of optical receivers by enabling single chip integration with mature CMOS technology.

References

[1]   N. Savage, "Linking with light - high-speed optical interconnects," *Spectrum, IEEE,* vol. 39, pp. 32-36, 2002.

[2]   M. R. Feldman, S. C. Esener, C. C. Guest, and S. H. Lee, "Comparison between optical and electrical interconnects based on power and speed considerations," *Applied Optics,* vol. 27, pp. 1742-1751, 1998.

[3]   D. A. B. Miller, "Rationale and challenges for optical interconnects to electronic chips," *Proceedings of the IEEE,* vol. 88, pp. 728-749, 2000.

[4]   Fiber Channel Industry Association (FCIA).[Online].Viewed 2008. Available:http:www.fiberchannel.org.

[5]   Fiber Channel over Ethernet (FCoE).[Online].Viewed 2008. Available:http://fcoe.com.

[6]   K. J. Ebeling, U. Fiedler, R. Michalzik, G. Reiner, and B. Weigl, "Recent advances in semiconductor vertical cavity lasers for optical communications and optical interconnects," in *22nd European Conference on Optical Communication, ECOC '96*, 1996, pp. 81-88 vol.2.

[7]   F. Koyama, "Recent Advances of VCSEL Photonics," *Journal of Lightwave Technology,* vol. 24, pp. 4502-4513, 2006.

[8]   M. Jutzi, M. Grozing, E. Gaugler, W. Mazioschek, and M. Berroth, "2-Gb/s CMOS optical integrated receiver with a spatially Modulated photodetector," *IEEE Photonics Technology Letters,* vol. 17, pp. 1268-1270, 2005.

[9]   Y. Kang, H.-D. Liu, M. Morse, M. J. Paniccia, M. Zadka, S.

Litski, G. Sarid, A. Pauchard, Y.-H. Kuo, H.-W. Chen, W. S. Zaoui, J. E. Bowers, A. Beling, D. C. McIntosh, X. Zheng, and J. C. Campbell, "Monolithic germanium//silicon avalanche photodiodes with 340 GHz gain-bandwidth product," *Nature Photonics,* vol. 3, pp. 59-63, 2009.

[10] P. Bhadri, P. Mal, S. Konanki, and F. R. Beyette, Jr., "Implementation of CMOS photodetectors in optoelectronic circuits," in *The 15th Annual Meeting of the IEEE Lasers and Electro-Optics Society*, 2002, pp. 683-684 vol.2.

[11] T. K. Woodward and A. V. Krishnamoorthy, "1-Gb/s integrated optical detectors and receivers in commercial CMOS technologies," *IEEE Journal of Selected Topics in Quantum Electronics,* vol. 5, pp. 146-156, 1999.

[12] H. Zimmermann and T. Heide, "A monolithically integrated 1-Gb/s optical receiver in 1-μm CMOS technology," *IEEE Photonics Technology Letters,* vol. 13, pp. 711-713, 2001.

[13] B. Yang, J. D. Schaub, S. M. Csutak, D. L. Rogers, and J. C. Campbell, "10-Gb/s all-silicon optical receiver," *IEEE Photonics Technology Letters,* vol. 15, pp. 745-747, 2003.

[14] S. Radovanovic, A. J. Annema, and B. Nauta, "A 3-Gb/s optical detector in standard CMOS for 850-nm optical communication," *IEEE Journal of Solid-State Circuits,* vol. 40, pp. 1706-1717, 2005.

[15] W. K. Huang, Y. C. Liu, and Y. M. Hsin, "A High-Speed and High-Responsivity Photodiode in Standard CMOS Technology," *IEEE Photonics Technology Letters,* vol. 19, pp. 197-199, 2007.

[16] W. K. Huang, Y. C. Liu, and Y. M. Hsin, "Bandwidth enhancement in Si photodiode by eliminating slow diffusion photocarriers," *Electronics Letters,* vol. 44, pp. 52-53, 2008.

118

[17]   S. M. Sze, *Physics of Semiconductor Devices*, 2nd ed. New York: Wiley, 1981.

[18]   H. Zimmermann, *Integrated Silicon Optoelectronics*. New York: Springer, 2000.

[19]   S. R. Cho, S. K. Ynag, J. S. Ma, J. S. Yu, S. D. Lee, A. G. Choo, and T. I. Kim, "Investigations of Floating Guard Structures in a Planar InGaAs/InGaAsP/InP Avalanche Photodiode," *Journal of Korean Physical Society,* vol. 38, pp. 182-185, 2001.

[20]   H. Finkelstein, M. J. Hsu, and S. C. Esener, "STI-Bounded Single-Photon Avalanche Diode in a Deep-Submicrometer CMOS Technology," *IEEE Electron Device Letters,* vol. 27, pp. 887-889, 2006.

[21]   S. Wolf, *Silicon Processing for the VLSI Era, Volume 1: Process Technology*. Los Angeles: Lattice Press, 2000.

[22]   D. S. Kim, S. R. Forrest, G. H. Olsen, M. J. Lange, R. U. Martinelli, and N. J. Di Giuseppe, "Avalanche gain in InAsyP1-y (0.1 < y < 0.3) photodetectors," *IEEE Photonics Technology Letters,* vol. 7, pp. 911-913, 1995.

[23]   G. Kim, I. G. Kim, J. H. Baek, and O. K. Kwon, "Enhanced frequency response associated with negative photoconductance in an InGaAs/InAlAs avalanche photodetector," *Applied Physics Letters,* vol. 83, pp. 1249-1251, 2003.

[24]   Y. C. Wang, "Small-signal characteristics of a Read diode under conditions of field-dependent velocity and finite reverse saturation current," *Solid State Electronics,* vol. 21, pp. 609-615, 1978.

[25]   Y. Ahn, K. Han, and H. Shin, "A new physical RF model of junction varactors," *Japanese Journal of Applied Physics,* vol. 42, pp. 2110-2113, 2003.

[26] M. Neuhauser, H. M. Rein, and H. Wernz, "Low-noise, high-gain Si-bipolar preamplifiers for 10 Gb/s optical-fiber links-design and realization," *IEEE Journal of Solid-State Circuits,* vol. 31, pp. 24-29, 1996.

[27] C.-S. Choi, H.-S. Kang, W.-Y. Choi, D.-H. Kim, and K.-S. Seo, "Phototransistors based on InP HEMTs and their applications to millimeter-wave radio-on-fiber systems," *IEEE Transactions on Microwave Theory and Techniques,* vol. 53, pp. 256-263, 2005.

[28] C.-S. Choi, J.-H. Seo, W.-Y. Choi, H. Kamitsuna, M. Ida, and K. Kurishima, "60-GHz bidirectional radio-on-fiber links based on InP-InGaAs HPT optoelectronic mixers," *IEEE Photonics Technology Letters,* vol. 17, pp. 2721-2723, 2005.

[29] J.-H. Seo, C.-S. Choi, Y.-S. Kang, Y.-D. Chung, J. Kim, and W.-Y. Choi, "SOA-EAM frequency up/down-converters for 60-GHz bi-directional radio-on-fiber systems," *IEEE Transactions on Microwave Theory and Techniques,* vol. 54, pp. 959-966, 2006.

[30] J.-H. Seo, Y.-K. Seo, and W.-Y. Choi, "1.244-Gb/s data distribution in 60-GHz remote optical frequency up-conversion systems," *IEEE Photonics Technology Letters,* vol. 18, pp. 1389-1391, 2006.

[31] H. Ogawa, D. Polifko, and S. Banba, "Millimeter-wave fiber optics systems for personal radio communication," *IEEE Transactions on Microwave Theory and Techniques,* vol. 40, pp. 2285-2293, 1992.

[32] P. Smulders, "Exploiting the 60 GHz band for local wireless multimedia access: prospects and future directions," *IEEE Communications Magazine,* vol. 40, pp. 140-147, 2002.

[33] R. L. Van Tuyl, "Unlicensed millimeter wave communications.

A new opportunity for MMIC technology at 60 GHz," in *18th Gallium Arsenide Integrated Circuit (GaAs IC) Symposium*, 1996, pp. 3-5.

[34]   M. Marcus and B. Pattan, "Millimeter wave propagation; spectrum management implications," *IEEE Microwave Magazine,* vol. 6, pp. 54-62, 2005.

[35]   Y. Shoji, K. Hamaguchi, and H. Ogawa, "Millimeter-wave remote self-heterodyne system for extremely stable and low-cost broad-band signal transmission," *IEEE Transactions on Microwave Theory and Techniques,* vol. 50, pp. 1458-1468, 2002.

[36]   Y. Shoji, K. Hamaguchi, and H. Ogawa, "A Low-Cost and Stable Millimeter-Wave Transmission System Using a Transmission-Filter-Less Double-Side-Band Millimeter-Wave Self-Heterodyne Transmission Technique," *IEICE Transaction on Communications,* vol. E86-B, pp. 1884-1892, 2003.

[37]   Q. Z. Liu, R. Davies, and R. I. MacDonald, "Experimental investigation of fiber optic microwave link with monolithic integrated optoelectronic mixing receiver," *IEEE Transactions on Microwave Theory and Techniques,* vol. 43, pp. 2357-2360, 1995.

[38]   G. Maury, A. Hilt, T. Berceli, B. Cabon, and A. Vilcot, "Microwave-frequency conversion methods by optical interferometer and photodiode," *IEEE Transactions on Microwave Theory and Techniques,* vol. 45, pp. 1481-1485, 1997.

[39]   W. K. Kulczyk and Q. V. Davis, "The avalanche photodiode as an electronic mixer in an optical receiver," *IEEE Trans. Electron Devices,* vol. 19, pp. 1181-1190, 1972.

[40] A. J. Seeds and B. Lenoir, "Avalanche diode harmonic optoelectronic mixer," *IEE Proceedings,* vol. Pt. J, pp. 353-357, Dec. 1986.

[41] M. Y. W. Chia, B. Luo, M. L. Yee, and E. J. Z. Hao, "Radio over multimode fibre transmission for wireless LAN using VCSELs," *Electronics Letters,* vol. 39, pp. 1143-1144, 2003.

[42] A. Das, A. Nkansah, N. J. Gomes, I. J. Garcia, J. C. Batchelor, and D. Wake, "Design of low-cost multimode fiber-fed indoor wireless networks," *IEEE Transactions on Microwave Theory and Techniques,* vol. 54, pp. 3426-3432, 2006.

[43] T. Niiho, M. Nakaso, K. Masuda, H. Sasai, K. Utsumi, and M. Fuse, "Transmission performance of multichannel wireless LAN system based on radio-over-fiber techniques," *IEEE Transactions on Microwave Theory and Techniques,* vol. 54, pp. 980-989, 2006.

[44] T. Pak Kay, O. Ling Chuen, A. Alphones, B. Luo, and M. Fujise, "PER and EVM measurements of a radio-over-fiber network for cellular and WLAN system applications," *Journal of Lightwave Technology,* vol. 22, pp. 2370-2376, 2004.

[45] K. A. Persson, C. Carlsson, A. Alping, A. Haglund, J. S. Gustavsson, P. Modh, and A. Larsson, "WCDMA radio-over-fibre transmission experiment using singlemode VCSEL and multimode fibre," *Electronics Letters,* vol. 42, pp. 372-374, 2006.

[46] F. Tabatabai and H. Al-Raweshidy, "Performance Evaluation for WLAN and UWB Using Radio over Fibre," in *The 9th European Conference on Wireless Technology*, 2006, pp. 147-149.

[47] M. L. Yee, H. L. Chung, P. K. Tang, L. C. Ong, B. Luo, M. T.

Zhou, Z. Shao, and M. Fujise, "850nm Radio-Over-Fiber EVM Measurements for IEEE 802.11g WLAN and Cellular Signal Distribution," in *36th European Microwave Conference*, 2006, pp. 882-885.

[48]   *Wireless LAN Medium Access Control (MAC) and Physical Layer (PHY) specifications: High-Speed Physical Layer in the 5 GHz Band*, IEEE Standard 802.11a-1999, Part11, 1999.

[49]   *Wireless LAN Medium Access Control (MAC) and Physical Layer (PHY) specifications*, IEEE Standard 802.11-2007, Part 11, 2007.

List of Publications

Journal Papers

[1] **Hyo-Soon Kang**, Myung-Jae Lee, and Woo-Young Choi, "Low-Cost Multi-Standard Radio-over-Fiber Downlinks Based on CMOS-Compatible Si Avalanche Photodetectors," *to be published in IEEE Photonics Technology Letters*, 2009.

[2] **Hyo-Soon Kang**, Myung-Jae Lee, and Woo-Young Choi, "6.25-Gb/s Optical Receiver Using a CMOS-Compatible Si Avalanche Photodetector," *Journal of the Optical Society of Korea*, vol. 12, no. 4, pp. 217–220, December 2008.

[3] Myung-Jae Lee, **Hyo-Soon Kang**, Kwang-Hyun Lee, and Woo-Young Choi, "Self-Oscillating Harmonic Optoelectronic Mixer Based on a CMOS-Compatible Avalanche Photodetector for Fiber-Fed 60-GHz Self-Heterodyne Systems," *IEEE Transaction on Microwave Theory and Techniques*, vol. 56, no. 12, pp. 3180–3187, December 2008.

[4] Myung-Jae Lee, **Hyo-Soon Kang**, and Woo-Young Choi, "Equivalent Circuit Model for Si Avalanche Photodetectors Fabricated in Standard CMOS Process," *IEEE Electron Devices Letters*, vol. 29, no. 10, pp. 1115–1117, October 2008.

[5] **Hyo-Soon Kang**, and Woo-Young Choi, "Fiber-supported 60 GHz self-heterodyne systems based on CMOS-compatible harmonic optoelectronic mixers," *IEE Electronics letters*, vol. 43, no. 20, pp. 1101–1103, September 27, 2007.

[6] **Hyo-Soon Kang**, Myung-Jae Lee, and Woo-Young Choi, "Si avalanche photodetectors fabricated in standard complementary

metal-oxide-semiconductor process," *Applied Physics Letters*, vol. 90, 151118, April 12, 2007.

[7]   Chang-Soon Choi, **<u>Hyo-Soon Kang</u>**, Woo-Young Choi, Dae-Hyun Kim, and Kwang-Seok Seo, "Phototransistors based on InP HEMTs and their applications to millimeter-wave radio-on-fiber systems," *IEEE Transactions on Microwave Theory and Techniques*, vol. 53, no. 1, pp. 256–263, January 2005.

[8]   **<u>Hyo-Soon Kang</u>**, Chang-Soon Choi, Woo-Young Choi, Dae-Hyun Kim, and Kwang-Seok Seo, "Characterization of phototransistor internal gain in metamorphic high-electron-mobility transistors," *Applied Physics Letters*, vol. 84, no. 19, pp. 3780–3782, May 2004.

[9]   C.-S. Choi, **<u>H.-S. Kang</u>**, W.-Y. Choi, H.-J. Kim, W.-j. Choi, D.-H. Kim, K.-C. Jang, and K.-S. Seo, "High Optical Responsivity of InAlAs/InGaAs Metamorphic High-Electron Mobility Transistor on GaAs substrate with Composite Channels," *IEEE Photonics Technology Letters*, vol. 15, no. 6, pp. 846–848, June 2003.

[10] Chang-Soon Choi, **<u>Hyo-Soon Kang</u>**, Dae-Hyun Kim, Kwang-Seok Seo, and Woo-Young Choi, "60GHz Harmonic Optoelectronic Up-Conversion Using an InAlAs/InGaAs Metamorphic High-Electron-Mobility Transistor on a GaAs Substrate," *Japanese Journal of Applied Physics*, vol. 42, pp. L658–L659, June 2003.

International Conference Presentations

[1]   **<u>Hyo-Soon Kang</u>**, Myung-Jae Lee, and Woo-Young Choi, "Multi-Standard Radio-over-Fiber Systems Using CMOS-Compatible Si

Avalanche Photodetectors," *IEEE Topical Meeting on Microwave Photonics*, pp. 302–305 Gold Coast, Australia, September 30 – October 3, 2008.

[2] Woo-Young Choi, and **Hyo-Soon Kang**, "CMOS-Compatible Si Avalanche Photodetectors for Microwave Photonics Applications," *Optoelectronics and Communications Conference (OECC)*, WeP-01, Sydney, Australia, July 7 – 10, 2008 (Invited Paper).

[3] **Hyo-Soon Kang**, Myung-Jae Lee, and Woo-Young Choi, "Radio-Over-Fiber Systems for WLAN Based on CMOS-Compatible Si Avalanche Photodetectors," *IEEE MTT-S International Microwave Symposium (IMS)*, pp. 503–506, Atlanta, GA, USA, June 15 – 20, 2008.

[4] Myung-Jae Lee, **Hyo-Soon Kang**, Kwang-Hyun Lee, and Woo-Young Choi, "Fiber-Fed 60-GHz Self-Heterodyne Systems Using Self-Oscillating Harmonic Optoelectronic Mixers Based on CMOS-Compatible APDs," *IEEE MTT-S International Microwave Symposium (IMS)*, pp. 587–590, Atlanta, GA, USA, June 15 – 20, 2008.

[5] Minsu Ko, **Hyo-Soon Kang**, and Woo-Young Choi, "A CMOS-Compatible Schottky-Barrier Diode Detector for 60-GHz Amplitude-Shift Keying (ASK) Systems," *IEEE MTT-S International Microwave Symposium (IMS)*, pp. 1557–1560, Atlanta, GA, USA, June 15 – 20, 2008.

[6] **Hyo-Soon Kang**, Myung-Jae Lee, and Woo-Young Choi, "Characterization of Silicon Avalanche Photodetectors Fabricated in Standard CMOS process," *The 7th Pacific Rim Conference on Lasers and Electro-Optics*, pp. 614–615, COEX, Seoul, Korea, August 26 – 31, 2007.

[7] **Hyo-Soon Kang**, and Woo-Young Choi, "CMOS-compatible 60

GHz Harmonic Optoelectronic Mixer," *IEEE MTT-S International Microwave Symposium (IMS)*, pp. 233–236, Honolulu, HI, USA, June 3 – 8, 2007.

[8] **Hyo-Soon Kang**, and Woo-Young Choi, "Millimeter-wave Optoelectronic Mixers Based on CMOS-Compatible Si Photodetectors," *International Topical Meeting on Microwave Photonics*, T1-5, Grenoble, France, October 4 – 6, 2006.

[9] **Hyo-Soon Kang**, and Woo-Young Choi, "Bias Voltage Optimization of Vertical PN-Junction Photodetectors Fabricated in Standard CMOS Technology," *The 8th International Conference on Electronics, Information, and Communication*, pp. 340–343, Ulaanbaatar, Mongolia, June 27 – 28, 2006.

[10] Woo-Young Choi, Chang-Soon Choi, **Hyo-Soon Kang**, Dae-Hyun Kim, and Kwang-Seok Seo, "Fiber-supported millimeter-wave data transmission systems based on InP HEMTs," *The 6th Korea-Japan Joint Workshop on Microwave and Millimeter-wave Photonics*, pp. 8–11, Gyeongju, Korea, January 27 – 28, 2005.

[11] Chang-Soon Choi, **Hyo-Soon Kang**, Dae-Hyun Kim, and Kwang-Seok Seo, and Woo-Young Choi "Characteristics of InP HEMT Harmonic Optoelectronic Mixers and Their Application to 60GHz Radio-on-Fiber Systems," *IEEE MTT-S International Microwave Symposium*, pp. 401–404, Fort Worth, TX, USA, June 5 – 11, 2004.

[12] Chang-Soon Choi, **Hyo-Soon Kang**, Dae-Hyun Kim, and Kwang-Seok Seo, and Woo-Young Choi "Millimeter-wave InP HEMT Optoelectronic Mixer," *The 5th Japan-Korea Joint Workshop on Microwave and Millimeter-wave Photonics*, pp. 19–22, Piazza ohmi Otsu, Shiga, Japan, January 29 – 30, 2004.

[13] **Hyo-Soon Kang**, Chang-Soon Choi, Woo-Young Choi, Dae-Hyun Kim, and Kwang-Seok Seo, "High Conversion Gain Millimeter-

wave Optoelectronic Mixer based on InAlAs/InGaAs Metamorphic HEMT," *International Topical Meeting on Microwave Photonics*, pp.105–108, Budapest, Hungary, September 10 – 12, 2003.

Domestic Conference Presentations

[1] **Hyo-Soon Kang**, Woo-Young Choi, "Radio-over-Fiber Systems for WLAN Using CMOS APD," *The 15th Conference on Optoelectronics and Optical Communications (COOC)*, pp. 300-301, Busan Haeundae Hanwha Resort, May 14–16, 2008 (Invited Paper).

[2] Myung-Jae Lee, **Hyo-Soon Kang**, Kwang-Hyun Lee, Woo-Young Choi, "Fiber-supported 60 GHz-band Self-heterodyne Wireless Systems Using a Self-oscillating Harmonic Optoelectronic Mixer," *The 15th Conference on Optoelectronics and Optical Communications (COOC)*, pp. 304-305, Busan Haeundae Hanwha Resort, May 14–16, 2008.

[3] **Hyo-Soon Kang**, Woo-Young Choi, "WLAN Radio-on-Fiber Systems Based on CMOS Compatible Avalanche Photodetectors," *Photonics Conference*, pp. 353-354, Jeju Poonglim Resort, November 14–16, 2007.

[4] Myung-Jae Lee, **Hyo-Soon Kang**, Woo-Young Choi, "An Equivalent Circuit Model for CMOS Compatible Avalanche Photodetectors," *Photonics Conference*, pp. 65-66, Jeju Poonglim Resort, November 14–16, 2007.

[5] Minsu Ko, **Hyo-Soon Kang**, Woo-Young Choi, "0.18-um CMOS Schottky Barrier Diodes for 60-GHz Self-Heterodyne Systems,"

Autumn Conference on Microwave and Wave Propagation, pp. 471-474, Cheju National University, September 13–14, 2007.

[6] **Hyo-Soon Kang**, Myung-Jae Lee, Woo-Young Choi, "Photodetection Frequency Response Peaking in Si Avalanche Photodetectors Fabricated in Standard CMOS Process," *The 14th Conference on Optoelectronics and Optical Communications (COOC)*, pp. 110-111, Jeju Hanwah Resort, May 16–18, 2007.

[7] **Hyo-Soon Kang**, Woo-Young Choi, "60 GHz Harmonic Optoelectronic Mixers Based on CMOS-compatible Si APD," *Photonics Conference*, pp. 314-315, Sorak Daemyung Resort, November 8–10, 2006.

[8] **Hyo-Soon Kang**, Woo-Young Choi, "Bias Voltage Optimization of Vertical PN-Junction Photodetectors Fabricated in Standard CMOS Technology," *The 13th Conference on Optoelectronics and Optical Communications (COOC)*, pp. 213-214, Bugok Ilsung Condominium, May 10–12, 2006.

[9] Chang-Soon Choi, **Hyo-Soon Kang**, Dea-Hyun Kim, Kwang-Seok Seo, Woo-Young Choi, "Fiber-optic/60GHz broadband transmission systems using InP HEMT phototransistors," *The 11th Conference on Optoelectronics and Optical Communications (COOC)*, pp.283-284, Information and Communications University, May 12–13, 2004.

[10] **Hyo-Soon Kang**, Chang-Soon Choi, Woo-Young Choi, Kyoungchul Jang, Kwang-Seok Seo, "Photodetection Characteristics of InAlAs/InGaAs/InP HEMT," *Optical Society of Korea Annual Meeting*, pp. TF-V6, Inha University, February 13–14, 2003.

[11] **Hyo-Soon Kang**, Chang-Soon Choi, Woo-Young Choi, Joo-Hiuk Son, Kyungchul Jang, Kwang-Seok Seo, "Photodetection of 1.55 μm modulated lightwave in InP HEMT," *Photonics Conference*,

pp. 719-720, Yongpyong Resort, October 30 – November 1, 2002.

[12] Chang-Soon Choi, **Hyo-Soon Kang**, Woo-Young Choi, Hwe-Jong Kim, Won-Jun Choi, Kyungchul Jang, Dae-Hyun Kim, Kwang-Seok Seo, "Photoresponse of InAlAs/InGaAs Metamorphic HEMT on GaAs substrate with Composite Channel," *Photonics Conference*, pp. 723-724, Yongpyong Resort, October 30 – November 1, 2002.

[13] Chang-Soon Choi, **Hyo-Soon Kang**, Young-Kwang Seo, Jun-Hyuk Seo, Woo-Young Choi, Kyungchul Jang, Dae-Hyun Kim, Kwang-Seok Seo, "60GHz Broadband Up-conversion using Metamorphic HEMT as a Harmonic Optoelectronic Mixer," *Photonics Conference*, pp. 83-84, Yongpyong Resort, October 30 – November 1, 2002.

Patents

[1] **Hyo-Soon Kang**, and Woo-Young Choi, "Optoelectronic Mixer Based on CMOS and Base Station Using the Same,"
Korean Patent, Patent No. 10-0789364, December 20, 2007.

[2] **Hyo-Soon Kang**, Kwang-Hyun Lee, and Woo-Young Choi, "Wireless Communication System Having CMOS Structure and Method of Manufacturing the Same,"
Korean Patent, Patent No. 10-0829117, May 6, 2008
PCT Patent, Application No. PCT/KR2007/000928, February 22, 2007.